

How does remotely sensed degree of curing and fuel load vary in grasslands and effect modelled fire spread?

Wasin Chaivaranont

A thesis in fulfilment of the requirements for the degree of
Doctor of Philosophy



Climate Change Research Centre
School of Biological, Earth and Environmental Sciences
Faculty of Science

September 2018

ORIGINALITY STATEMENT

'I hereby declare that this submission is my own work and to the best of my knowledge it contains no materials previously published or written by another person, or substantial proportions of material which have been accepted for the award of any other degree or diploma at UNSW or any other educational institution, except where due acknowledgement is made in the thesis. Any contribution made to the research by others, with whom I have worked at UNSW or elsewhere, is explicitly acknowledged in the thesis. I also declare that the intellectual content of this thesis is the product of my own work, except to the extent that assistance from others in the project's design and conception or in style, presentation and linguistic expression is acknowledged.'

Signed

Date 28/9/2018

COPYRIGHT STATEMENT

'I hereby grant the University of New South Wales or its agents the right to archive and to make available my thesis or dissertation in whole or part in the University libraries in all forms of media, now or here after known, subject to the provisions of the Copyright Act 1968. I retain all proprietary rights, such as patent rights. I also retain the right to use in future works (such as articles or books) all or part of this thesis or dissertation.

I also authorise University Microfilms to use the 350 word abstract of my thesis in Dissertation Abstract International (this is applicable to doctoral theses only).

I have either used no substantial portions of copyright material in my thesis or I have obtained permission to use copyright material; where permission has not been granted I have applied/will apply for a partial restriction of the digital copy of my thesis or dissertation.'

Signed

Date 28/9/2018

AUTHENTICITY STATEMENT

'I certify that the Library deposit digital copy is a direct equivalent of the final officially approved version of my thesis. No emendation of content has occurred and if there are any minor variations in formatting, they are the result of the conversion to digital format.'

Signed

Date 28/9/2018

Table of Contents

Table of Contents	i
Acknowledgement	iv
Abbreviations and Symbols	v
List of Figures	viii
List of Tables	xi
1 Introduction.....	1
1.1 Motivation and Objectives.....	1
1.2 Literature Review.....	2
1.2.1 Remote Sensing and Fire Risks	2
1.2.2 Field Observations.....	3
1.2.3 Satellite Products – VOD and NDVI.....	3
1.2.4 Grassland Fire Danger Index.....	5
1.2.5 DOC and Fuel Load Estimation with Remote Sensing.....	6
1.2.6 Grassland Fire Spread Modelling	8
2 Methods.....	11
2.1 Dataset Description	11
2.1.1 VOD and NDVI	11
2.1.2 Climate Datasets	13
2.1.3 Land Cover, Vegetation Structure, Burned Area, and Digital Elevation Maps	15
2.1.4 Site Observed DOC and Fuel Load	17
2.2 Models Description	20
2.2.1 Phoenix RapidFire Model	20
2.2.2 Spark Model	21
3 Estimated Degree of Curing with Satellite Data	25
3.1 Existing Approaches to Estimate DOC with Optical Based Satellite Products	25
3.2 Calibrating VOD-NDVI-based DOC estimate model.....	26

3.2.1	Multiple Linear Regression Model.....	26
3.2.2	Observed DOC Site Selection	28
3.2.3	Calibration Results	29
3.3	Evaluating VOD-NDVI-based DOC Estimate Model.....	34
3.3.1	Evaluation Results.....	34
3.3.2	Spatial and Temporal Variability	35
3.4	Comparing GFDI Derived From VOD-NDVI-based and Existing DOC Estimation	38
3.4.1	Calculating GFDI	38
3.4.2	GFDI Severity Level vs Burned and Unburned Areas	42
3.4.3	Comparison with Current DOC Products	45
3.5	Limitations	46
4	Estimated Fuel Load with Satellite Data.....	48
4.1	Observed Fuel Load Data.....	48
4.1.1	Site-based Fuel Load.....	48
4.1.2	Bioregion Based Fuel Load	49
4.2	Estimating Fuel Load with Satellite Products	49
4.2.1	Estimating Fuel Load Using VOD and Site-based Observations.....	50
4.2.2	Annual AGBC Estimation Using VOD	52
4.3	Fuel Load Model Calibration	54
4.4	Fuel Load Model Evaluation	55
4.4.1	Spatial and Temporal Variability	55
4.4.2	Comparison with Vegetation Structure Data	58
4.5	Limitations	Error! Bookmark not defined.
5	Modelled Grassland Fire Spread Behaviour due to DOC Variations	63
5.1	Experiment Setups	63
5.1.1	DOC and Topography Data	64
5.1.2	Idealised Experiments	65
5.1.3	Realistic Experiments	66

5.2	Grassland Fire Spread with Variable DOC Results	68
5.2.1	Idealised Experiments	68
5.2.2	Realistic Experiments	73
5.3	Discussion	77
5.3.1	Grass Fire Spreads in Idealised Condition.....	77
5.3.2	Modelled Grass Fire Spreads from Past Events	78
5.3.3	Model Uncertainties.....	80
6	Grasslands Fire Spread Behaviour due to Fuel Load Variations.....	82
6.1	Experiment Setups	83
6.1.1	Fuel Load, DOC and Topography Data	83
6.1.2	Idealised Experiments	84
6.1.3	Realistic Experiments	85
6.2	Grassland Fire Spread with Variable Fuel Load Results	86
6.2.1	Idealised Experiments	86
6.2.2	Realistic Experiments	90
6.3	Discussions	95
6.3.1	Grass Fire Spreads in Idealised Condition.....	95
6.3.2	Modelled Grass Fire Spreads from Past Events	96
6.3.3	Limitations	98
7	Conclusions.....	100
	References	104

Acknowledgement

This thesis will not be possible without the continuous supports from the following parties. Firstly, I would like to thank my thesis supervisor and co-supervisors, Jason Evans and Yi Liu from the University of New South Wales (UNSW) and Jason Sharples from UNSW Canberra for their excellent mentoring, motivation, and support. I could not imagine having better supervisors for my PhD. I really appreciate their dedication, effort, and the time they put into my PhD study. It has been quite a stressful, yet enjoyable, insightful, and fulfilling 3.5 years journey with them. I would also like to extend my thanks to my thesis committee, postgraduate coordinator, and other academics and staff at Climate Change Research Centre (CCRC) for their academic and administration support.

Secondly, I would like to thank Marta Yebra, Albert van Dijk, Hamish Clarke, Richard Lucas, and Rachel Bessel for their direction and assistance in supplying observation datasets for my research. I would also like to thank Levi Roberts, Stuart Matthews, and James Hilton for their valuable aid in helping me setting up both Phoenix RapidFire and Spark fire spread models. This thesis would not be as complete as it currently is without support from these generous individuals.

Thirdly, I would like to express my gratitude to my undergraduate honours thesis supervisor at UNSW, Matthew McCabe, and my Master thesis supervisor at Imperial College London, Panos Parpas, for their advice and recommendations when I initially planned to pursue my PhD. Also, thanks to my fellow CCRC students and officemates, UNSW Thai Students Society, my postgraduate friends from Imperial College London, my undergraduate comrades from UNSW and Thammasat University, and my high school buddies from Bangkok Christian College for their continuous morale support and friendships.

Lastly, I would like to thank my mother – Vinita Chaivaranonth, my father – Somnuk Chaivaranont, and my family for their endless, unconditional support of my decisions. I would not have been the person I am today without them.

My PhD study is funded by UNSW tuition fee scholarship and Australian Research Council's Centre of Excellence for Climate System Science top up scholarship.

Abbreviations and Symbols

a, b, c, d	Coefficients
AGBC	Aboveground Biomass Carbon
ALOS-1	Advanced Land Observing Satellite
AMSR-E	Advanced Microwave Scanning Radiometer – Earth Observing System
AMSR2	Advance Microwave Scanning Radiometer 2
AVHRR	Advanced Very High Resolution Radiometer
AWAP	Australian Water Availability Project
BNHCRC	Bushfire and Natural Hazards Cooperative Research Centre
CFA	Country Fire Authority
CMIP5	Coupled Model Intercomparison Project Phase 5
CSIRO	Commonwealth Scientific and Industrial Research Organisation
DEM	Digital Elevation Model
DOC	Degree of Curing (%)
ECMWF	European Centre for Medium-Range Weather Forecasts
ELVIS	Elevation Information System
f, g, h	Elliptical Shape Parameters
f(DOC)	Curing Factor
FFDI	McArthur Forest Fire Danger Index
FRP	Fire Radiative Product (MW)
GFDI	McArthur Grassland Fire Danger Index
GVMl	Global Vegetation Monitoring Index
H _{3pm}	Daily Relative Humidity at 3pm (%)
k	Decomposition Rate
L ₀	Rate of Litterfall
L _{rem}	Remaining Litter After Specific Time Period (t ha ⁻¹)
$\frac{L}{B}$	Length-to-Breath Ratio
LPRM	Land Parameter Retrieval Model
MCD12C1	MODIS Land Cover Type Map (UMD Scheme, 2010)

MCD14ML	MODIS Active Fire Product
MCD45A1	MODIS 1 month Burned Area Product (Combined)
MCD64A1	MODIS 1 month Burned Area Product (Combined, Direct Broadcast)
MOD09A1	MODIS 8 day Surface Reflectance Product (Terra Satellite)
MODIS	Moderate Resolution Imaging Spectroradiometer
NASA	National Aeronautics and Space Administration
NCI	National Computational Infrastructure
NDVI	Normalised Difference Vegetation Index
NOAA	National Oceanic and Atmospheric Administration
NVIS	Native Vegetation Information System framework
Q	Fuel Load (t ha^{-1})
R	Rate of Fire Spread on Flat Terrain (km h^{-1})
R_0	Zero-wind Rate of Fire Spread (km h^{-1})
R_b	Back Fire Rate of Spread (km h^{-1})
R_f	Flank Fire Rate of Spread (km h^{-1})
R_h	Head Fire Rate of Spread (km h^{-1})
R_η	Rate of Fire Spread on a Specified Slope (km h^{-1})
RFI	Radio Frequency Interference
RG	Relative Greenness
RMSE	Root Mean Square Error
ROC	Receiver Operating Characteristic
t	Time Period
$T_{1/2}$	Half-Life of Litter (yrs)
T_{max}	Daily Maximum Temperature ($^{\circ}\text{C}$)
UMD	University of Maryland
USGS	United States Geological Survey
V	Wind Speed (km h^{-1})
V_{max}	Daily Maximum Wind Speed (km h^{-1})
VOD	Vegetation Optical Depth
VOD6	6.9 GHz or C-band Vegetation Optical Depth
VOD10	10.7 GHz or X-band Vegetation Optical Depth
WRF	Weather Research and Forecasting

α, β	Percentages of the Head Fire Rate of Spread
γ	Curing Coefficient
η	Slope of Ground Surface ($^{\circ}$)
θ	Fire Spread Direction ($^{\circ}$)
μ	Moisture Coefficient
ρ_1	620 to 670 μm Spectral Reflectance (Visible)
ρ_2	841 to 876 μm Spectral Reflectance (Near-Infrared)
ρ_6	1628 to 1652 μm Spectral Reflectance
ρ_7	2105 to 2155 μm Spectral Reflectance

List of Figures

Figure 2.1 Example vegetation optical depth (VOD) and normalised difference vegetation index (NDVI) time series (b) and spatial maps, (c) for VOD and (d) for NDVI, at Silent Grove, WA (17.13° S, 125.37° E). The star (*) indicate the location of the time series on Australia map (a).	13
Figure 2.2 MODIS MCD12C1 land cover type map for Australia (Hansen et al., 2000). The locations of observed degree of curing (DOC) sites are marked with crosses. 17	
Figure 3.1 Scatter plot of observed degree of curing (DOC) from five calibration sites against VOD, NDVI, and combined VOD and NDVI terms.	31
Figure 3.2 Scatter plot of residual observed degree of curing (DOC) from five calibration sites that are unexplained by NDVI against VOD and combined VOD and NDVI terms.	32
Figure 3.3 Scatter plots between observed and estimated degree of curing (DOC) from the first (Equation 3.7) and second (Equation 3.8) models during calibration, all sites evaluation, and independent sites evaluation stage, corresponding to the information in Table 3.1; dash line represent idealise 1:1 line (perfect fit) while grey solid represent the best fit.	33
Figure 3.4 Example satellite based and site observed degree of curing (DOC) time series comparison at Silent Grove, WA (17.131° S, 125.374° E) (b), where the star (*) indicate the location of the time series on Australia map (a). Satellite based DOC across Australia during summer (December, January, February) for 2002-2003 (c) and 2010-2011 (d) are shown with forest areas masked out.	36
Figure 3.5 Spatial standard deviation of estimated degree of curing (DOC) time series from 4 July 2002 to 26 June 2011.	37
Figure 3.6 Temporal standard deviation of estimated degree of curing (DOC) map from 4 July 2002 to 26 June 2011.	37
Figure 3.7 Maximum estimated Grassland Fire Danger Index (GFDI) for summer (December, January, February) of 2002-2003 (a) and 2009-2010 (b). Both zoomed areas marked with red bounding boxes for (a) and (b) are shown in (c) and (d), respectively. The fires locations for Canberra fire (c) and Toodyay fire (d) are marked with red crosshair. Forest areas are masked out in white.	40
Figure 3.8 MCD64A1 burned area map (Ruiz et al., 2014) during summer (December, January, February) 2002-2003 (a) and 2009-2010 (b) with forest areas masked out.	41

Figure 3.9 Grassland Fire Danger Index (GFDI) time series plot at Weston Creek, ACT, from July 2002 to June 2011 (a) and at Toodyay, WA, from July 2002 to June 2011 (b) where the red vertical dash line indicates the date of fire event on 18 January 2003 for Canberra fire and on 29 December 2009 for Toodyay fire. Solid black line is estimated GFDI time series computed from estimated degree of curing (DOC), whereas green dash line is GFDI time series computed from constant DOC at 100%. 42

Figure 3.10 Grassland Fire Danger Index (GFDI) severity level histograms at burned and unburned areas over Australia during 4 July 2002 to 26 June 2011 where the dark and light blue shaded bars are recalculated GFDI with satellite estimated variable degree of curing (DOC), while the green and yellow shaded with diagonal hatch bars are reference GFDI with constant DOC at 100%. 44

Figure 4.1 Example annual average VOD (black) and AGBC (blue) time series comparison at Silent Grove, WA (17.13° S, 125.37° E) (b), where the star (*) indicate the location of the time series on Australia map (a). 53

Figure 4.2 Example satellite based fuel load time series comparison at Silent Grove, WA (17.13° S, 125.37° E) (b), where the star (*) indicate the location of the time series on Australia map (a). Annual satellite based fuel load across Australia during 2003 (c) and 2011 (d) are shown. 56

Figure 4.3 Spatial standard deviation of estimated fuel load time series from 2003 to 2011. 57

Figure 4.4 Temporal standard deviation of estimated fuel load map from 2003 to 2011. 58

Figure 4.5 Vegetation structure map (rescaled to 0.1°) across Australia (Lucas et al., 2014). 60

Figure 5.1 DOC spatial maps for a) idealised experiment scenario I1a (only I1 with DOC = 100% is shown here), I4, and I5, b) idealised experiment scenario I2, c) idealised experiment scenario I3, d) realistic experiment scenario R1 (Toodyay, WA), e) realistic experiment scenario R2 (Pulletop, NSW), and f) realistic experiment scenario R3 (Jail Break Inn, NSW). Black borders indicate the 100 x 200 km experiment domain. Red dots or lines indicate the fire ignition location for each experiment. 65

Figure 5.2 Scatter plot showing the changes in the rate of spread due to changes in DOC from idealised experiments I1a to I1g, I2, I4a to I4b, and I5a to I5b for both Phoenix and Spark models. Calculated rate of spread from Cheney et al. (1998) and Cruz et al. (2015) are shown as dash lines. Predicted rate of spread with slope modifier from Noble et al. (1980) are shown as crosses. 71

Figure 5.3 Burned time step (2 left columns for Spark and Phoenix) and flame height (right column for Phoenix) over the burned area in the idealised experiments (only I1a, I4b, and I5b are shown for scenario I1, I4, and I5), where the background shows the corresponding DOC spatial map in greyscale (as shown in Figure 5.1). 72

Figure 5.4 Fire propagation speed at each burned time step comparison time series for all realistic experiments (a, b, and c for scenario R1, R2, and R3), where the blue line shows control scenarios with homogeneous DOC = 100%, the black line shows scenarios using satellite based DOC, and the red line shows scenarios using satellite based DOC and digital elevation model. Solid lines are for Phoenix model, whereas dash lines are for Spark models. 75

Figure 5.5 Burned time step (2 left columns for Spark and Phoenix) and flame height (right column for Phoenix) area burned maps for realistic experiment, where the background shows the corresponding DOC spatial map in greyscale (as shown in Figure 5.1). The scenarios with digital elevation map (R1-C, R2-C, and R3-C) are not shown here due to negligible changes in spreads. For Phoenix’s scenario R2-B, a 10 times magnifying burned area are shown with red bounding box insets. 76

Figure 6.1 Artificial fuel load for idealised experiments (a, b, and c) and satellite based fuel load at Toodyay, WA (d), Pulletop, NSW (e), and Jail Break Inn, NSW (f) for realistic experiments. Red lines and dots indicate the fire ignition locations. Only 20 t ha⁻¹ fuel load is shown for idealised experiment scenarios with homogeneous fuel load. 84

Figure 6.2 Changes in rate of spread due to changes in fuel load from Phoenix (black) and Spark (blue) idealised experiments..... 88

Figure 6.3 Phoenix and Spark idealised experiments burned time spatial maps. Grayscale backgrounds show the corresponding fuel load map from Figure 6.1. Only experiments I1a, I4b, and I5b are shown for scenario I1, I4, and I5..... 89

Figure 6.4 Rate of spread comparison between Phoenix and Spark idealised experiments. Only scenario I1, I4, and I5 are shown. The marker size of I1 represents the fuel load level (larger circle represents higher fuel load). 90

Figure 6.5 Phoenix and Spark realistic experiments burned time spatial maps. Grayscale backgrounds show the corresponding fuel load map from Figure 6.1. Scenarios with suffix D are not shown. For Phoenix’s scenario R2-C, a 10 times magnifying burned area are shown with red bounding box insets..... 94

Figure 6.6 Rate of spread comparison between Phoenix and Spark realistic experiments, where X represents number ranging from 1 to 3 (scenario R1, R2, and R3)..... 95

List of Tables

Table 2.1 List of datasets used in this study in order of appearance.	18
Table 3.1 Calibration and evaluation of satellite based degree of curing (DOC) model derived from Vegetation Optical Depth (VOD) and Normalised Difference Vegetation Index (NDVI). Existing estimated DOC models, Method B (Newnham et al., 2010) and MapVic (Martin et al., 2015), evaluations are also listed below.....	32
Table 3.2 Spatial standard deviation of estimated degree of curing (DOC) by season, month, and land cover type from 4 July 2002 to 26 June 2011.....	38
Table 3.3 Referenced and recalculated Grassland Fire Danger Index (GFDI) severity and burned-unburned area contingency table for satellite based degree of curing (DOC) derived from Vegetation Optical Depth (VOD) and Normalised Difference Vegetation Index (NDVI). Reference GFDI is computed from constant DOC at 100%, while recalculated GFDI is computed from satellite based DOC.....	45
Table 3.4 Recalculated Grassland Fire Danger Index (GFDI) severity and burned-unburned area contingency table for degree of curing (DOC) computed with Method B (Newnham et al., 2010) and MapVic (Martin et al., 2015) model. Reference GFDI is computed from constant DOC at 100%, while recalculated GFDI is computed from satellite based DOC.	46
Table 4.1 List of vegetation structural formations (as shown in Figure 4.5) and their corresponding total vegetation cover fraction and 95 th percentile height.....	61
Table 5.1 List of weather inputs for idealised fire spread experiment.	67
Table 5.2 Observed weather conditions from the nearest weather station for realistic fire spread experiments.....	67
Table 5.3 List of chosen fire events for realistic fire spread experiments with corresponding nearest weather stations.	68
Table 5.4 Average fire spread speed, area burned, and average flame height for idealised experiments.....	70
Table 5.5 Average fire spread speed, area burned, and average flame height for realistic experiments.	74
Table 6.1 Idealised experiments average fire spread speed and area burned for Phoenix and Spark models.	87
Table 6.2 Realistic experiments average fire spread speed and area burned for Phoenix and Spark models.	92

1 Introduction

1.1 Motivation and Objectives

Wildfire can become a rapidly spreading, destructive fire over natural landscapes; it is a major natural hazard worldwide. Wildfire can negatively influence the land use, soil degradation, and emission of greenhouse gas (Arroyo et al., 2008). Some major environmental damage and changes to ecosystems are the results of wildfire (Cobb et al., 2016; Gazzard et al., 2016; Mistry et al., 2016). One of the important components in determining the severity of wildfire is fuel availability. Wildland fuels can vary considerably, both spatially and temporally (Stambaugh et al., 2011). Various interpretations and characterisations of fuel have been made in past studies as a key contribution to assessing wildfire potential (Hudec and Peterson, 2012; Jurdao et al., 2012; Peterson et al., 2008; Sharples et al., 2009a; Stambaugh et al., 2011; Yebra et al., 2013). Fuel can also be quantified by its age or time since last fire (Bradstock et al., 2010).

In Australia, most wildfires are generally referred to as bushfires. To be more specific, a bushfire can be described by its dominant fuel type, such as forest fire, grass fire, or scrub fire. Grasslands are the most widespread fuel type in Australia with nearly 75% coverage (Cheney and Sullivan, 2008). Thus, efforts are being dedicated to the prediction and management of grassland fire.

There are multiple factors that influence a grassland fires severity, including fuel conditions and weather variables. Due to their fuel characteristics, grassland fires are very responsive to weather conditions, especially wind speed, wind direction, and relative humidity (Cheney and Sullivan, 2008). Fuel availability also plays an important role in a grassland fires severity (Cheney et al., 1998; Cruz et al., 2015; Kidnie et al., 2015). Grassland fuel availability can be quantified with the metric known as the degree of curing (DOC). The DOC is the percentage of dead material in a grassland fuel bed; 100% indicates a fully cured (dead) grassland fuel complex. Fuel load, while its influence on grassland fire severity is not as prominent as other factors mentioned, is another interesting variable in grassland fire.

In this study, I focused on grassland DOC and fuel load and their influence on fire spread and severity. DOC and fuel load monitoring over Australia is currently limited in space and time. To quantify the spatial and temporal variability of both grassland DOC and fuel load, I developed estimates of DOC and fuel load using satellite observations over Australia. This observed DOC and fuel load gridded data was then used as inputs to fire spread models to assess the impact on spread of grassland fires due to variation in DOC and fuel load. The questions I am addressing in this thesis are: how does DOC and fuel load vary in space and time, and how do these variations effect fire spread as predicted by current fire spread models?

1.2 Literature Review

1.2.1 Remote Sensing and Fire Risks

There are currently many Earth observing satellites acquiring a large amount of data relevant to surface vegetation. Many remote sensing approaches have been developed to estimate fire relevant properties of the fuel and have been assessed and compared in previous studies (Arroyo et al., 2008; Yebra et al., 2013). Note that the combination of data retrieval method, type of sensor, and spectral information are dependant on the respective research objectives.

There are numerous advantages in remote sensing methods. This includes very cost effective, high spatial and temporal coverage, much faster and more consistent update time, and easier access to data (Arroyo et al., 2008). However, some of the traditional limitations in remote sensing still persist. Including: inability to identify the vertical structure of fuel bed; canopy obstruction in high density forest; high variability and inherent complexity of fuel types across spatial and temporal domain; and the resolution is too coarse for smaller or point scale representation; are some examples of remote sensing limitations for wildfire fuel mapping (Keane et al., 2001; Saatchi et al., 2007). Significant errors and inaccuracies can also be introduced by cloud cover, variability in land cover, atmospheric effects such as aerosols and water vapour, and variations between satellite over-passes (Dilley et al., 2004).

1.2.2 Field Observations

The earliest efforts to gather fuel spatial data were based on field survey. Field observation involved simple but tedious procedures, such as recording the type of fuel conditions on a paper map while traversing an area by foot (Hornby, 1935), collecting samples required for destructive sampling back in the laboratory to determine moisture content (Yebra et al., 2013), and extensive field inventory with statistical analysis and inference (Miller et al., 2003).

The main advantage of field observed fuel data is its accuracy because the researcher is in physical contact with the fuel. Though, there are chances that mapping errors may occur; the error is still likely to be limited to improper fuel type assessments. Note that the amount of money and time required for extensive fuel field mapping implementation may not be practical for many land managers (Falkowski et al., 2005; Miller et al., 2003). Thus, field observation is deemed to be appropriate for use as the reference or basic source of fuel datasets, and here it is used to evaluate remotely sensed fuel estimations.

1.2.3 Satellite Products – VOD and NDVI

The satellite products I used to estimate both DOC and fuel load in this study are a more recent, passive microwave based product and a well-known, optical based product. The recently developed, passive microwave based remote sensing vegetation product used here is called vegetation optical depth (VOD) (Meesters et al., 2005). VOD is primarily sensitive to vegetation water content, including both leafy and woody components (Guglielmetti et al., 2007; Jackson and Schmugge, 1991; Kerr and Njoku, 1990). The other product is a traditional, optical based vegetation index called normalised difference vegetation index (NDVI). As opposed to VOD, NDVI is primarily sensitive to vegetation greenness.

NDVI is a well-established vegetation index and has been used in many vegetation and biomass studies. For instance, NDVI was used to identify the changes in Australian vegetation cover due to climate related trends between 1981 to 2006; the results showed an overall greening of Australia over these decades, where persistent vegetation types have better benefits than recurrent vegetation types (Donohue et al., 2009). NDVI was also often used as a complimentary dataset for investigating vegetation. For example, NDVI was used along with a satellite derived soil moisture to quantify the long term

changes in vegetation due to large spatial variations in soil moisture. It was found that soil moisture affected NDVI in both monthly variations and long term changes, and both NDVI and soil moisture had coherent trends (Chen et al., 2014). Another example of NDVI application was to help discriminating the climate and human induced dryland degradation. NDVI and precipitation data were used to determine the area of high possibility of human induced degradation. The climate induced changes can be identified using the rainfall period that was best related to maximum NDVI; any deviations from this relationship were considered as human induced degradation (Evans and Geerken, 2004). It should be noted that optical based remote sensing products, including NDVI, are affected by cloud cover and aerosols. Some studies explicitly acknowledged challenges presented by cloud effects and when there are both forest and water bodies in the same NDVI pixel, which resulted in an erroneous grassland interpretation (Allan et al., 2003; Chladil and Nunez, 1995).

Unlike the traditional optical based vegetation indices, such as NDVI, VOD is minimally influenced by the atmospheric conditions due to its longer wavelength and stronger penetration capacity (Jones et al., 2009). However, it has a coarser spatial resolution (0.1°) in comparison with optical based products, which is a consequence of the low energy microwave emissions from the Earth's surface. It had been demonstrated that VOD can capture the changes in vegetation water content over different land cover types at the global scale, including grassland, cropland, savannas, tropical forests, and boreal forests (Liu et al., 2015, 2013a, 2013b). Also, NDVI and VOD provided complementary information and can comprehensively characterise vegetation dynamics when combined (Andela et al., 2013; Liu et al., 2011).

There are various past studies using VOD. Jones et al. (2011) used VOD to monitor global vegetation phenology, which characterise seasonal cycle of vegetation that influences the land-atmosphere water exchange and carbon cycle. It was found that VOD corresponded well with vegetation indices and leaf area index from optical based satellite and exhibited a unique end of season signal associated with changes in canopy water content. It was concluded that VOD contributed to a better view of land surface phenology than optical based vegetation indices (Jones et al., 2011). VOD was also used to determine the long term changes in regional and global environments via the changes in vegetation water content across different land cover types. For instance, the biomass reduction in Mongolian Steppes was successfully identified by VOD. It was found that the VOD declines in Mongolian Steppes were approximately 60% due to climate

variations and the rest are from increased goat population and wild fire (Liu et al., 2013a). For global biomass changes, it was found that VOD changes in different land cover types can be attributed to various factors VOD patterns have a strong correlation with temporal precipitation patterns over grasslands and shrublands, while VOD changes in croplands are associated with both precipitation patterns and agricultural improvements (Liu et al., 2013b).

1.2.4 Grassland Fire Danger Index

Since wildfires are primarily driven by weather and climate, many different types of fire danger rating systems are implemented based on different local meteorological variables in a specific region. Though, these fire danger rating systems interpret and quantify their inputs differently, many meteorological parameters required by these fire danger indices are common, such as temperature, relative humidity, and wind speed. For instance, McArthur Forest Fire Danger Index (FFDI) (McArthur, 1967), McArthur Grassland Fire Danger Index (GFDI) (Noble et al., 1980; Purton, 1982), and Sharples Simple Index (Sharples et al., 2009b) are fire danger indices that required all three common meteorological parameters.

Several revisions of GFDI were made by past studies (Noble et al., 1980; Purton, 1982). The GFDI revision used in this study is modified Mark 4 GFDI, since it is the grassland fire danger assessing system that is generally being used by Bureau of Meteorology (Sharples et al., 2009b). Originally, the fire danger rating system was presented in a circular slide rule. A mathematical equation representation of modified Mark 4 GFDI was derived from the circular meter, and can be expressed as follows in Equation 1.1 (Purton, 1982):

$$GFDI = Q^{1.027} f(DOC) \exp(-1.523 + 0.0276T_{max} - 0.2205\sqrt{H_{3pm}} + 0.6422\sqrt{V_{max}}) \quad (1.1)$$

where Q is the fuel load (kg m^{-2}), T_{max} is the dry bulb or daily maximum temperature ($^{\circ}\text{C}$), H_{3pm} is the daily relative humidity at 3 pm (%), V_{max} is the daily maximum wind speed (km h^{-1}), and $f(DOC)$ is the curing factor and DOC is, of course, the degree of curing (%). The curing factor can be calculated by Equation 1.2.

$$f(DOC) = \exp(-0.009432(100 - DOC)^{1.536}) \quad (1.2)$$

Note that though GFDI provides a satisfactory fire danger rating for grassland, it does not provide satisfactory predictions of the rate of spread (Cheney and Sullivan, 2008).

1.2.5 DOC and Fuel Load Estimation with Remote Sensing

There are several past studies that use remote sensing, in particular optical based satellite products, to estimate DOC (Chladil and Nunez, 1995; Dilley et al., 2004; Martin et al., 2015; Newnham et al., 2011, 2010; Turner et al., 2011). Some of these studies used NDVI, while others used multiple optical based vegetation indices. In Chladil and Nunez (1995) and Dilley et al. (2004), both studies used satellite derived NDVI and ground observations estimated fuel moisture content and DOC. While one study area was in Tasmania (Chladil and Nunez, 1995), the other was in Victoria (Dilley et al., 2004). In Chladil and Nunez (1995) study, NDVI had been used to produce DOC derived from a soil dryness index model to predict soil and fuel moisture content. While Dilley et al. (2004) established a relationship between DOC and NDVI by estimating live fuel moisture content from NDVI and relating it to curing via an exponential function using a finite difference Levenberg-Marquardt method (Rouse et al., 1973). Both studies found a good relation between NDVI and DOC in their respective study area. Another method for estimation of DOC using NDVI can be achieved by using a relative greenness (RG) approach that was based on NDVI distribution to provide more accurate estimation of DOC than a direct linear regression between DOC and NDVI (Newnham et al., 2011). NDVI and other optical based vegetation indices computed from remote sensing reflectance products can also be developed into a satellite based model integrated with ground observations to predict DOC (Martin et al., 2015; Turner et al., 2011).

Bureau of Meteorology are currently providing two DOC estimation products that have 500 m spatial resolution and daily temporal resolution based on two past studies (Martin et al., 2015; Newnham et al., 2010). There are five separate satellite based DOC models; four are from Newnham et al. (2010) and one is from Martin et al. (2015). All satellite based DOC models are based on optical and near-infrared wavelength bands, hence they share similar limitations concerning clouds and aerosols etc. Here I propose a new satellite derived DOC product that combines observations in the optical and infrared wavelengths with observations in the microwave band. The addition of microwave observations will reduce the sensitivity to atmospheric interference improve the DOC estimation over Australia.

For fuel load estimation, some studies opted for much higher resolution remote sensing products (higher than 500 m), such as radar and aerial imagery, in a much smaller area rather than over continental areas (Brandis and Jacobson, 2003; Jin and Chen, 2012; Miller et al., 2003; Reich et al., 2004; Saatchi et al., 2007; Scott et al., 2002). In the USA, fuel load snapshots were developed from aerial photographs for two particular areas in New Mexico (Scott et al., 2002), Landsat imagery in South Dakota (Reich et al., 2004), and multifrequency polarimetric synthetic aperture radar in Yellowstone National Park (Saatchi et al., 2007). For the first two studies, they found that while the high spatial resolution fuel load models developed were good, the models exhibited high errors on one of the two study areas (Scott et al., 2002) and some degree of skewed distribution (Reich et al., 2004). For the third study, it was found that the three major fuel load parameters (canopy fuel weight, canopy bulk density, and foliage moisture content) that were estimated provided more than 70% accuracy when compared to plot measurements (Saatchi et al., 2007). Usage of these fuel load models were also limited to certain regions that have similar climate, terrain, and soil conditions. While in China, a more recent study use a newer high resolution satellite image from QuickBird and Landsat imagery to constructed a fuel load model for a region in northeast of China. They found that both QuickBird and Landsat models performed better at estimating fine fuel loads, while not as good for coarse fuel loads (Jin and Chen, 2012). For Australia, there was a study using observed data collected from Popran National Park in New South Wales and Landsat imagery. In this study, two estimation methods were tested, where the first method used classification techniques to derived current fuel load from predicted vegetation type and fire history and the second method used litterfall estimation from biomass. It was found that the classification method overestimated fuel loads and biomass method was subject to less uncertainty (Brandis and Jacobson, 2003). There was also a study that used lower spatial but higher temporal resolution satellite product, such as the wildfire risk modelling in the Mojave Desert in Nevada. In this study, NDVI was used in fuel load prediction model along with other climate and topography parameters (Van Linn et al., 2013).

Other fuel load estimation studies decided to rely solely on field records for fuel load estimation model development, such as a study in several locations across Australian open woodlands and forests (Gilroy and Tran, 2009). Linear regression models were developed for open woodland and open forest fuel types based on field observations in various areas across Australia. It was found that the developed model provided useful guidance on the fine fuel loads development in eucalypt forests of southeast Queensland

(Gilroy and Tran, 2009). Fire severity can also affect the variability in fuel load as demonstrated by the fuel variability study in Cascade Range, USA. It was found that fire severity influenced the immediate post burned canopy fuels but not the dead and down surface fuel loads (Hudec and Peterson, 2012). In contrast, fuel aging and structures can also influence fire behaviour, as demonstrated in an Australian eucalypt forest fire behaviour study. It was found that the fire behaviour was dominantly affected by the near surface fuel layer during the prescribed burn experiments (McCaw et al., 2012).

Here, I propose a different approach to estimate fuel load over Australia by using the VOD derived aboveground biomass carbon (AGBC) estimation as a proxy for estimating fuel load (Liu et al., 2015). AGBC was estimated globally via microwave based VOD and used to assess the interannual variations and recent reversal in global AGBC reduction. It was found that the increase in AGBC was associated with wetter conditions in the savannahs of northern Australia and southern Africa. The AGBC dataset derived here has the same moderate spatial resolution as VOD and annual temporal resolution. While the spatial resolution is much lower than the imagery products used for estimating fuel load in most of the past studies described earlier, it has an advantage of providing a total spatial coverage over Australia.

1.2.6 Grassland Fire Spread Modelling

The factors influencing wildfire behaviour can be loosely categorised into three main components: fuels; weather; and topography. Many fire danger rating systems, fuel classification, and other related research is based on fire behaviour and spread modelling (Rothermel, 1972). In order to improve fire spread predictions in various grassland types in Australia, rural fire authorities requested the Commonwealth Scientific and Industrial Research Organisation (CSIRO) to undertake major research on fire spread in 1986 (Cheney and Sullivan, 2008). The development of grassland fire spread models has been heavily based on field observation data. The traditional southern grassland fire spread model developed by the CSIRO in 1998, associated grass fuel load with the condition of pasture for practical field use; level of grassland fuels was associated with three pasture categories: undisturbed (high fuel load), grazed (moderate fuel load), and eaten-out pasture (low fuel load) (Cheney et al., 1998). In addition, Cheney et al. (1998) model suggested that grassland fires are unable to spread where DOC is less than 50%. However, more recent studies also by CSIRO on grassland fire spread model developments that put more emphasis on DOC revised this limit (Cruz et

al., 2015; Kidnie et al., 2015). In Cruz et al. (2015) model, grassland fires can spread on an area with DOC as low as 20%.

To simplify the process of fire spread predictions, several integrated software packages for the prediction of fire spread have been developed. In Australia, Phoenix RapidFire (hereafter referred to as Phoenix) is one of the more popular fire spread models with a lot of complex features (Tolhurst et al., 2008). Phoenix fire propagation prediction is based on Huygenon principle (simulates the propagation of fire with an elliptic stencil) (Knight and Coleman, 1993). Its grassland fire behaviour module is based on modified version of CSIRO southern grassland fire spread model discussed earlier (Cheney et al., 1998).

Phoenix is widely used in fire simulation studies in Australia, including examining the effects of fire weather, suppression, and fuel treatment on fire behaviour in the Sydney Basin (Penman et al., 2013), changes in future fire behaviour due to revegetation altering the fuel characteristics in New South Wales (Collins et al., 2015), and a fire risk mitigation policy and scientific interactions study in Victoria (Neale et al., 2016). Penman et al. (2013), using Phoenix simulations, concluded that fuel treatment can benefit the fire management agencies in a case where the suppression resources can respond rapidly. Collins et al. (2015) found that revegetation rarely increased median fire intensity over the suppressible levels, while the fuel load and fire weather were the main factors in suppressibility. Neale et al. (2016) used Phoenix as a part of their workshop in investigating how wildfire scientific research and policy and practices interacted. Phoenix has also been adapted for fire modelling outside of Australia, such as in a case study in Cavillon, France, where Phoenix was used to predicted fire spread in the interface area between the vegetated and urban area (Pugnet et al., 2013). The study in France concluded that Phoenix was effective in predicting spread in the vegetated and urban interface area, but testing with other fire events was required before a widespread deployment. Phoenix is routinely used in bushfire agency operations, such as those conducted by the New South Wales Rural Fire Service (Louis and Matthews, 2015).

There is also a more recently developed software package that models fire spread called Spark (Miller et al., 2015). Spark uses a level set method as its baseline for predicting fire propagation (Osher and Sethian, 1988). While all fire behaviour models in Phoenix are embedded in the core of the program and are inaccessible to the user, Spark allows much more flexibility where the user can specify their own fire behaviour algorithm for

any fuel classification to govern the baseline level set method. Currently Spark can only output the predicted rate of spread and fire perimeter, in contrast to Phoenix which offers various fire behaviour components. However, Spark is relatively young model and continuous improvement and development in refining the fire perimeter shape and its internal level set method are still ongoing (Hilton et al., 2017, 2016, 2015).

Both Phoenix and Spark models were recently evaluated in a fire spread models evaluation report by Bureau of Meteorology (Deslandes and Jacobs, 2017). In this evaluation, four simulators (Phoenix, Spark, Prometheus, and Australis) were evaluated based on ten case studies. It was found that no single fire spread simulator performs distinctively better than others, since none performed well for all case studies. One of the case studies, the Cobbler Road fire (8 January 2013), is a 6 hours, 140 km² grassland fire. In this case study, both Phoenix and Spark (with grassland model varied by grass fuel condition and additional flank and back fire spread modification) generally performed in a median range. The report recommended executing the simulators in ensemble based approach over single, deterministic runs to account for uncertainty in fuel, weather conditions, and ignition inputs.

2 Methods

This chapter describes all satellite and ground observation datasets used during this study. In addition, fire behaviour models used during the second part of this thesis (Chapter 5 and 6) is also described here. General methods that are used in multiple chapters are explained here, while unique methods that are exclusive to each individual chapter are described in their respective chapter.

2.1 Dataset Description

2.1.1 VOD and NDVI

VOD was used in the estimation of DOC and to derive AGBC, which was used for estimating fuel load over Australia. NDVI was used for estimating DOC only. Both estimated DOC and fuel load gridded data were then used as the fire spread models' inputs for analysing the sensitivity of grassland fire spread over landscapes with variable DOC and fuel load.

The NDVI dataset used here is derived from the Moderate Resolution Imaging Spectroradiometer (MODIS) 8 day surface reflectance product (MOD09A1) on-board the Terra satellite (Vermeulen and Vermeulen, 1999). The 8 day product has less noise than the daily product, and its spatial resolution is 0.005° (~500 m). This product is obtained from Remote Sensing at National Computational Infrastructure (NCI) MODIS Land Product for Australia website (Paget and King, 2008). It is produced from original tiles provided by the United States Geological Survey (USGS) for Australia with a starting date from 18 February 2000. Note that MOD09A1 is pre-processed with the provided quality flag grid, where the pixels with less than ideal quality were excluded prior to NDVI computation.

The 8 day NDVI data is derived from the MODIS reflectance dataset using Equation 2.1:

$$NDVI = \frac{\rho_2 - \rho_1}{\rho_2 + \rho_1} \quad (2.1)$$

where ρ_1 and ρ_2 are spectral reflectance measurements obtained from the visible (red) and near-infrared regions, respectively. During the conversion, to ensure the quality of data, only pixels with ideal quality in all bands and a view angle zenith of less than 60° were kept for the analysis, as suggested by Newnham et al. (2011). The spatial resolution was kept at 0.005° .

The VOD dataset used here is retrieved from the Advanced Microwave Scanning Radiometer – Earth Observing System (AMSR-E) using the Land Parameter Retrieval Model (LPRM) (Meesters et al., 2005; Owe et al., 2001). It has a spatial resolution of 0.1° (~10 km) and nearly daily temporal resolution (Parinussa et al., 2014). The time period covered by AMSR-E is from 2 June 2002 to 3 October 2011, but I use complete years covering a 9 year range from 4 July 2002 to 26 June 2011 in our analysis. The same time period is also used for the MOD09A1 NDVI dataset.

VOD data, which has a near daily temporal resolution, is converted to an 8 day average product to reduce noise and ensure complete coverage over Australia (10° S to 45° S and 110° E to 160° E) per temporal interval. The grid cells with radio frequency interference (RFI) are excluded from our analysis. RFI is caused by man-made transmitters, such as radars and wireless communications. These transmitters can be operated in the same frequency range as passive microwave observation, including VOD. Thus, natural signals captured by passive microwave observations are sometimes contaminated with RFI (Nijs et al., 2015).

There are two frequency variants of AMSR-E VOD available, a shortwave frequency (6.9 GHz or C-band) called VOD6 and a longwave frequency (10.7 GHz or X-band) called VOD10 (Reichle et al., 2007). The VOD data used for estimating DOC (Chapter 3) is VOD10. For estimation of fuel load (Chapter 4), VOD6 is used as a basis, while VOD10 is used as a replacement in the locations (pixels) that are affected by RFI.

An example comparison time series of VOD and NDVI from July 2002 to June 2011 at one of the observed DOC sites, Silent Grove, WA (17.13° S, 125.37° E) can be seen in Figure 2.1. It is shown that both VOD and NDVI have a similar seasonal cycle. Vegetation types that are present within the VOD (0.1°) and NDVI (0.005°) pixel influence the differences in VOD and NDVI behaviour. It is worth noting that the VOD time series is complete while the NDVI time series has periods of missing data generally caused by extended periods of atmospheric interference (clouds, aerosols, etc.). The difference

between VOD and NDVI spatial resolution can be clearly seen in the example $2^\circ \times 2^\circ$ spatial maps around the Silent Grove area (Figure 2.1). I used both VOD and NDVI together in DOC estimation to combine their strengths.

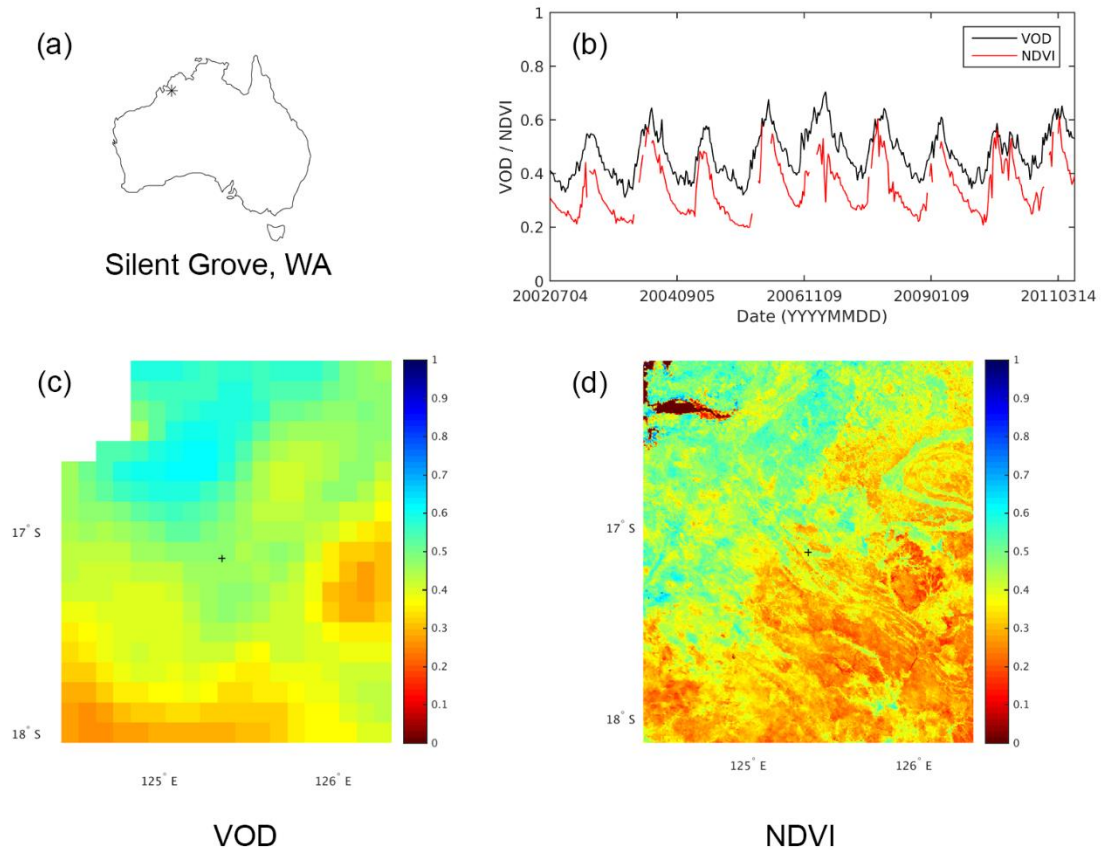


Figure 2.1 Example vegetation optical depth (VOD) and normalised difference vegetation index (NDVI) time series (b) and spatial maps, (c) for VOD and (d) for NDVI, at Silent Grove, WA (17.13° S, 125.37° E). The star () indicate the location of the time series on Australia map (a).*

2.1.2 Climate Datasets

Gridded and point observed climate datasets are used in study. Gridded climate datasets, in particular – dry bulb or maximum temperature, 3 pm relative humidity, maximum wind speed, from multiple sources are used for GFDI calculation for assessing the usability of the satellite based DOC (estimated from VOD and NDVI). Point observed climate datasets recorded from weather stations network across Australia (temperature, relative humidity, wind speed and direction) are used as inputs for fire spread models in the realistic fire spread experiments.

The gridded, meteorological datasets are usually derived from the network of ground observation stations across Australia. The range for the temperature, relative humidity, and wind speed datasets is from 4 July 2002 to 26 June 2011 to exactly match with the VOD 9 year range. Both temperature and relative humidity datasets are acquired from the Australian Water Availability Project (AWAP) (Jones et al., 2009). Note that relative humidity is derived from vapour pressure and temperature data. These AWAP datasets have a 0.05° spatial and daily temporal resolution with a coverage region of 10° S to 44.5° S and 112° E to 156° E. AWAP dataset has been widely used in climate modelling and land surface studies. For instance, there was a study on Australian rainfall patterns and associated vegetation growth. It was concluded that a lasting reduction in precipitation pattern was a major constraint on Australian vegetation growth (Liu et al., 2017). Another example is the study of changes in Australian temperature and precipitation extremes and future projection with Coupled Model Intercomparison Project Phase 5 (CMIP5) multi-model ensemble, where the results were: increases in high temperature extremes, changes in temperature extremes were mostly found in the tropics, more periods of dryness, and increases in the most intense precipitation extremes (Alexander and Arblaster, 2017). AWAP was also used in validating dynamical downscaling of coupled global circulation models, where it was found that air to sea interactions were important and global forecast bias corrections were needed before downscaling for applications over Australia (Ratnam et al., 2017). An example of remote sensing related study that used AWAP is the improvement of satellite observations on detecting dryland degradation, where an extension of an existing technique is developed and resulted in more accurate estimation of degradation in Australia (Burrell et al., 2017). In a variability of extreme fire weather in southeast Australia study, AWAP was used to compute the FFDI (Harris et al., 2017). AWAP data is also considered one of the most accurate gridded datasets over Australia (Contractor et al., 2015).

For maximum wind speed data, the reanalysis maximum daily wind speed is computed from the ERA-Interim wind components dataset, acquired from the European Centre for Medium-Range Weather Forecasts (ECMWF) (Dee et al., 2011). The reanalysis wind components dataset is available globally at approximately 0.8° resolution at a 6 hour interval. ERA-Interim reanalysis datasets are widely used in various field of studies. For instant, ERA-Interim was used in the estimation of sudden burst or drop in wind speed for wind energy production, where the results from the prediction based on the reservoir computing method showed significant improvement over prior models (Dorado-Moreno

et al., 2017). ERA-Interim was also used to compute weighted average characteristics of sea conditions in maritime traffic route in European seas to minimised risk (Vettor and Guedes Soares, 2017). In a climate dynamics study, specifically the surface storm track intensities and spatial patterns, the surface storm tracks in CMIP5 multi-model ensemble were examined against ERA-Interim. The study concluded a dual role in forcing the CMIP5 storm track from aloft and the ocean surface (Booth et al., 2017). For a global scale fire behaviour simulation study based on global topographic, climatic, and fuel bed data, ERA-Interim was used as fire weather inputs. It was found from the global simulations that the most severe fire events were found in grasslands and shrublands in tropical biomes (Pettinari and Chuvieco, 2017).

Point observed climate data are obtained from the past development of historical fire weather dataset (Lucas, 2010). The weather records are daily, ranging from 1973 to 2010 with over 300 observation sites across Australia. The historical fire weather dataset was further analysed for trends in Australia from 1973 to 2010 using FFDI. The discovered trends, found to be consistent with projected impact on climate change, suggested increased fire weather conditions at numerous locations across Australia, with an increase in FFDI magnitude and fire season duration (Clarke et al., 2013b). The historical fire weather dataset was also used in evaluating the fire weather prediction skill of the Weather Research and Forecasting (WRF) model over southeast Australia in 1985 to 2009; it was found that the WRF model predicted FFDI distribution and spatial variation with an overall positive bias, where errors in average FFDI were caused mostly from WRF humidity simulation error and errors in extreme FFDI were caused mostly from WRF wind speed simulation error (Clarke et al., 2013a). Another study that used the historical fire weather dataset was the assessment of climate change impact on fire risk in New South Wales. The study compared the FFDI computed from projected climate changes from regional climate models and a historical weather dataset with a result showing increases in both mean FFDI magnitude and mean number of days with high FFDI across New South Wales (Zhu et al., 2015).

2.1.3 Land Cover, Vegetation Structure, Burned Area, and Digital Elevation Maps

A land cover map of Australia is necessary for classifying dominant vegetation type with each gridded pixel of VOD and NDVI. It is used for calibration purposes when forming empirical models for estimating DOC and fuel load. Here, I use the global 0.05° land cover map based on the MODIS MCD12C1 product. The land cover classification system

is as proposed by the University of Maryland (UMD scheme) (Hansen et al., 2000). Figure 2.2 shows the 0.05° land cover type map of Australia, with observed curing sites marked with crosses. The land cover map used here is from year 2010.

For additional evaluation on estimation of fuel load with AGBC (derived from VOD), I use Australia vegetation height and structure dataset to ensure that the derived AGBC level is consistent with different vegetation structures across various Australian bioregions. The vegetation height and structure dataset is obtained from AusCover product catalogue (Lucas et al., 2014). While vegetation height and plant cover products are available separately, for simplicity, I acquired the plant structure product, which is a categorical dataset that combines vegetation height and plant cover products. The vegetation structure map is a 30 m gridded snapshot of Australia during the year 2009 (Lucas et al., 2015). This vegetation dataset is derived from Advanced Land Observing Satellite (ALOS-1 PALSAR), Landsat, and NASA Ice, Cloud, and Land Elevation (Rosenqvist et al., 2014). The dataset was also reviewed in a recent study on monitoring forest degradation with current remote sensing approaches. The study was a review of various remote sensing approaches for detecting forest degradation at national level, where future improvements were anticipated with the next generation of remote sensing sensors (Mitchell et al., 2017).

A satellite observed burned area map is used for evaluating the GFDI calculated with satellite based DOC and for locating the ignition location of the past fire events selected for fire spread model realistic experiments. I picked the monthly archived MODIS burned area map reprojected for Australia from Remote Sensing at the NCI site (Paget and King, 2008). There are two separate MODIS burned area products: the MCD45A1 and the MCD64A1. The MCD64A1 burned area product is preferred over MCD45A1, since it was proven to be more accurate (Andela and van der Werf, 2014; Padilla et al., 2015; Ruiz et al., 2014). It was previously used in Australia in the studies related to emission factors of Australia forest fire (Paton-Walsh et al., 2014) and estimating emission of greenhouse gases from a past Victoria fires (Surawski et al., 2016). Its spatial specification is the same as the MODIS reflectance dataset, with temporal availability from August 2000 onwards. To ensure high quality of the burned pixels, only pixels with the valid data flag from the provided quality control file are included in the analysis. Over 99 % of pixels from mid-2002 to mid-2011 are classified as unburned. To reduce the number of prescribed burned and other low power anomalies detected by the burned area product,

a fire radiative power (FRP, unit: MW) from MODIS active fire product (MCD14ML) is used to mask out low severity fires.

The digital elevation model (DEM) is needed for realistic fire spread model experiments in Chapter 5 and 6. I obtained 25 m DEM around the three realistic fire spread experimental sites, which are Toodyay, WA, Pulletop, NSW, and Jail Break Inn, NSW areas from Geoscience Australia via the Elevation Information System (ELVIS) service (Geoscience Australia, 2016). Note that the elevation variations around the burned areas in the experiments are quite low (not exceeding 1° slope).

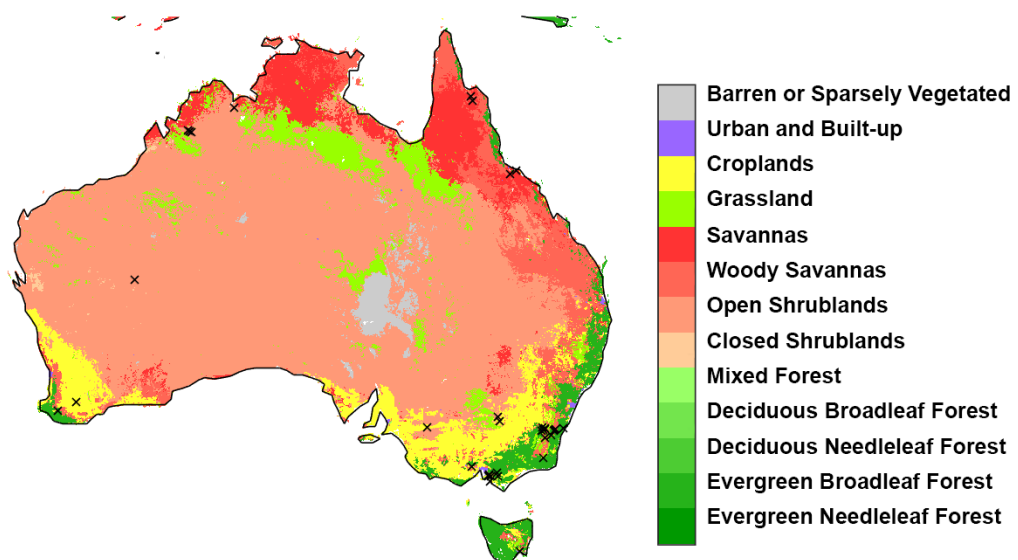


Figure 2.2 MODIS MCD12C1 land cover type map for Australia (Hansen et al., 2000). The locations of observed degree of curing (DOC) sites are marked with crosses.

2.1.4 Site Observed DOC and Fuel Load

Both site observed DOC and fuel load are required for calibrating and evaluating the satellite based estimation models for both DOC and fuel load.

The observed grassland DOC data was provided by Bushfire and Natural Hazards Cooperative Research Centre (BNHCRC) and its partner agencies (Project reference:

<http://www.bushfirecrc.com/projects/a14/grassland-curing>). The observed data were collected from several sites across Australia and New Zealand, ranging from August 2005 to March 2009, usually during summer. Refer to Figure 2.2 for DOC site locations. Selected sites were intended to represent broad coverage of major grassland types. Note that the number of locations and samples taken were highly dependent on the availability of field observers from fire management agencies; data were collected with inconsistent interval between data collection dates (Anderson et al., 2011). Three types of data collection approaches were used: visual estimation, levy rod method, and destructive sampling. Due to the number and availability of data as well as their accuracy, only observed DOC from the levy rod method was used in this study. Anderson et al. (2011) and Newnham et al. (2011) state that the levy rod measurement is reliable with less than 1% bias when compared with destructive sampling. Note that the number of locations and samples taken were highly dependent on the availability of field observers from fire management agencies; data are collected in a disjoint daily period, with inconsistent interval between each data collection date.

The observed fuel load data is extracted from recent prescribed fire effectiveness between Australia bioregion study (Price et al., 2015). There are 31 fuel load records for 31 different bioregions. Note that unlike observed DOC and other observed climate data, the fuel load data is not a daily or near daily data, but a snapshot value, representing the max fuel load for its corresponding bioregion. Other two fuel load datasets available are point observations of past fuel loads from various sites across Australia. The first site-based fuel load data is provided by BNHCRC and consisted of observation sites from South Australia. The second site-based fuel load data is provided by Country Fire Authority (CFA) and consisted of observation sites from Victoria. Both site-based fuel load data are as described in Section 4.1.1.

Every dataset used along with summary of their functions in the study is as summarised in Table 2.1

Table 2.1 List of datasets used in this study in order of appearance.

Dataset Used			
Name	Source	Format	Functions
Vegetation Optical Depth (VOD)	Parinussa et al. (2014)	Gridded (8-day)	Deriving DOC and fuel load (via AGBC).

MODIS MOD09A1 (Reflectance)	Paget and King (2008)	Gridded (8-day)	Deriving NDVI.
AWAP Temperature	Jones et al. (2009)	Gridded (Daily)	For computing GFDI.
AWAP Vapour Pressure	Jones et al. (2009)	Gridded (Daily)	Deriving relative humidity for computing GFDI.
ERA-Interim Wind Components	Dee et al. (2011)	Gridded (Daily)	Deriving wind speed for computing GFDI.
Historical Fire Weather Dataset	Lucas (2010)	Time Series (Daily)	Includes temperature, relative humidity, and wind speed; used as inputs in fire spread modellings.
MODIS MCD12C1 (Land Cover)	Hansen et al. (2000)	Gridded (Snapshot)	Used for Australia land cover classification throughout this study.
AusCover Vegetation Inventory (Vegetation Structure)	Lucas et al. (2014)	Gridded (Snapshot)	For evaluating gridded fuel load derived from VOD (via AGBC).
MODIS MCD64A1 (Burned Area)	Paget and King (2008)	Gridded (Daily)	For evaluating gridded GFDI computed from various DOC estimation models.
MODIS MCD14ML (Active Fire)	Paget and King (2008)	Gridded (Daily)	For reducing low power anomalies detected by MCD64A1.
ELVIS Digital Elevation Model (DEM)	Geoscience Australia (2016)	Gridded (Snapshot)	Used in fire spread modelling (in realistic experiments).
BNHCRC Site Observed DOC	Provided by BNHCRC	Time Series (Disjointed)	For calibrating and evaluating DOC estimation models.
Australia Bioregions Fuel Load	Price et al. (2015)	Gridded (Snapshot)	For calibrating fuel load estimation models.
BNHCRC South Australia Fuel Load	Provided by BNHCRC	Time Series (Disjointed)	For calibrating fuel load estimation models.
CFA Victoria Fuel Load	Provided by CFA	Time Series (Disjointed)	For calibrating fuel load estimation models.

Estimated DOC Method B	Newnham et al. (2010)	Gridded (8- day)	For comparison with estimated DOC developed in this study.
Estimated DOC MapVic	Martin et al. (2015)	Gridded (8- day)	For comparison with estimated DOC developed in this study.

2.2 Models Description

2.2.1 *Phoenix RapidFire Model*

I use two different fire behaviour models to execute the idealised and realistic grassland fire spread experiments. The first model is Phoenix (version 4.0.0.7) (Tolhurst et al., 2008, 2007), which is a dynamic fire behaviour and characterization model. Phoenix fire behaviour's modules are based on two modified fire behaviour models: CSIRO southern grassland fire model (Cheney et al., 1998) and the McArthur's Mark 5 forest fire behaviour model (McArthur, 1967; Noble et al., 1980). Its fire spread algorithms are based on Huygen's principle (Knight and Coleman, 1993). In addition to fire behaviour simulation component, Phoenix also integrates a likelihood and consequence business model.

The CSIRO southern grassland fire spread model (Cheney et al., 1998) underpinning Phoenix's grassland fire behaviour component is a function of pasture type, mean wind speed at 10 m in the open, moisture content of dead grass, and DOC. Two sets of equations are used to predict fire spread, respectively, for the cases where the wind speed is below and above 5 km h⁻¹. The model also supports three different major pasture types with differing fuel loads: undisturbed natural, and grazed, and eaten out pastures. Some modifications to the fire behaviour models in Phoenix have been made to accommodate the dynamic nature of fire and its surrounding environmental interactions (Tolhurst et al., 2008, 2007). The curing coefficient used in Phoenix is the original curing coefficient from Cheney et al. (1998) model, as shown in Equation 2.2.

$$\gamma = \frac{1.120}{1 + 59.2e^{-0.124(DOC-50)}} \quad (2.2)$$

where γ is the curing coefficient, which is a value between 0 to 1 modifying the rate of spread due to the level of presented DOC.

For grassland fuel load the original Cheney et al. (1998) model has three different grass states of natural, grazed, and eaten out which are associated with fuel loads ranging from 6.0 t ha⁻¹ to 1.5 t ha⁻¹. To incorporate continuous changes in state based on equivalent fuel load in Phoenix, the rate of spread is calculated for the natural state and is then modified by a factor proportional to the fuel load greater or less 6.0 t ha⁻¹. A consequence of the implementation in Phoenix is that fuel loads greater than 6.0 t ha⁻¹ can result in spread rates lower than that obtained for 6.0 t ha⁻¹ fuel load. This has been justified by asserting that the additional heat generated would create a greater drawback on the rate of spread (Tolhurst et al., 2007).

2.2.2 *Spark Model*

Spark (version 0.9.4) is a more recently developed system for predicting bushfire spread by CSIRO (Miller et al., 2015). Its fire propagation perimeter is represented by a level set method (Osher and Sethian, 1988). The fire behaviour components can be defined by the user, maximising the customizability of the simulation software

To closely emulate Phoenix's grassland fire behaviour module, I also use CSIRO southern grassland fire model (Cheney et al., 1998). However, I implement a modern revision of curing coefficient from Cruz et al. (2015) study, as shown in Equation 2.3.

$$\gamma = \frac{1.036}{1 + 103.989e^{-0.0996(DOC-20)}} \quad (2.3)$$

The revised curing coefficient allows fire to spread under a condition where DOC is as low as 20%, as opposed to the original DOC threshold of 50%.

To incorporate variability in fuel loads between different pasture states, a fitting curve between the coefficients of the rate of spread equations from three different pasture states and corresponding fuel load of 6.0, 4.5, and 1.5 t ha⁻¹ for natural, grazed, and eaten out pastures is formed. The fitting equations along with the corresponding Cheney et al. (1998) rate of spread models are as shown in Equation 2.4 for the case with wind speed over 5 km h⁻¹ and Equation 2.5 for wind speed under 5 km h⁻¹.

$$\begin{aligned} a &= 0.264 + 0.188Q \\ b &= 0.281Q^{0.614} \\ R_{V \geq 5} &= (a + b(V - 5)^{0.844})(\mu)(\gamma) \end{aligned} \quad (2.4)$$

$$a = 0.054$$

$$b = 0.0489 + 0.0363Q$$

$$R_{V<5} = (a + bV)(\mu)(\gamma) \quad (2.5)$$

Note that a and b are coefficients for Cheney et al. (1998) rate of spread model (R), Q is fuel load (t ha⁻¹), V is wind speed (km h⁻¹), μ is the moisture coefficient, and γ is the curing coefficient.

For lateral and back fire spreads, I have added a template to simulate different spread rates at the flanks and the back of the fires (Alexander, 1985). This is done by adding a 7% flanking and 2% backing spread of the head fire. These flanking and backing spread rates can be derived from an elliptic modelling approach and shape factor from past bushfire modelling studies (Anderson et al., 1982; Luke and McArthur, 1978). I use an elliptical shape to describe the perimeter of a grass fire under a constant wind (at any time period t) as in Equation 2.6, where R_0 is zero-wind rate of spread, f, g, and h are elliptical shape parameters depending on the wind speed, and θ is fire spread direction ranging from 0° to 360° (Anderson et al., 1982).

$$x(t, \theta) = R_0 t (f \cos \theta + g) \text{ and } y(t, \theta) = R_0 t (h \sin \theta) \quad (2.6)$$

In an idealised fire condition, the head, flank, and back fire rate of spread can be described as in Equation 2.7, where R_h , R_f , and R_b are the head, flank, and back fire rate of spread.

$$R_h = R_0(f + g), R_b = R_0(f - g), \text{ and } R_f \approx R_0 h \quad (2.7)$$

Equation 2.7 is then rearranged so that the flank and back fire rate of spread can be expressed as percentages of the head fire rate of spread (α and β) as in Equation 2.8.

$$R_b = \beta R_h \text{ and } R_f = \alpha R_h \quad (2.8)$$

From Luke and McArthur (1987) study, a relationship between length-to-breath ratio ($\frac{L}{B}$) or shape factor of a fire and a wind speed can be established by rearranging Equation 2.7 and 2.8 in term of f and h, as shown in Equation 2.9. The expression can be further simplified to Equation 2.10.

$$f = \frac{R_h(1+\beta)}{2R_0} \text{ and } h = \frac{\alpha R_h}{2R_0} \quad (2.9)$$

$$\frac{L}{B} = \frac{f}{h} = \frac{1+\beta}{2\gamma} \quad (2.10)$$

With a wind speed of 55 km h⁻¹ in idealised experiments, the shape factor is ~7 (Luke and McArthur, 1978). Hence, from Equation 2.10, α and β are approximately 2% for backing and 7% flanking rate of spread, respectively. For simplicity and consistency, I use 7% flanking and 2% backing rate of spread for every Spark experiment.

PART I: SATELLITE BASED DEGREE OF CURING AND FUEL LOAD

3 Estimated Degree of Curing with Satellite Data

In this chapter, I use both optical based (NDVI) and recently developed microwave based satellite data (VOD) along with site observed grassland DOC datasets to calibrate and evaluate a regression based model for prediction of DOC over Australia. The model developed here is then compared with the existing DOC products that are Newnham et al. (2010) Method B and Martin et al. (2015) MapVic models. I compare the GFDI calculated from satellite based models and constant DOC (100%) with the satellite observed burned areas over Australia and how satellite based DOC models help to improve fire severity prediction. Contents in this chapter are from the paper “Estimating Grassland Curing with Remotely Sensed Data” (Chaivaranont et al., 2018).

3.1 Existing Approaches to Estimate DOC with Optical Based Satellite Products

Satellite based DOC estimation over Australia are usually based on optical and infrared wavelength satellite sensor observations. As indicated by past studies (Dilley et al., 2004; Peterson et al., 2008), NDVI has a significant relationship with live fuel moisture content and DOC. Apart from using straight NDVI to establish a relationship with DOC, there are also other variations of modified NDVI, such as RG (Newnham et al., 2011). Newnham et al. (2011) found that RG has a stronger relationship with DOC than NDVI. One of the two alternatives Newnham et al. (2011) proposed is the range based RG, which can be computed by the following Equation 3.1, where the $NDVI_{min}$ and $NDVI_{max}$ are the minimum and maximum NDVI value over a specified time range. .

$$RG = \frac{NDVI - NDVI_{min}}{NDVI_{max} - NDVI_{min}} \quad (3.1)$$

However, estimated DOC using RG over Australia or very large areas is challenging since RG is highly dependent on the time range for minimum and maximum NDVI. Defining an appropriate time range for large areas encompassing various ecosystems is very difficult.

For DOC estimation over Australia, currently there are several products available from Bureau of Meteorology. There are five models available, four are based on Newnham et al. (2010) and one is based on Martin et al. (2015) studies. All models are also based on NDVI and reflectance products (optical and infrared based satellite products). Here, we show only one of Newnham et al. (2010) models (Method B) and the Martin et al. (2015) model (MapVic), since they have the best performance among the five models. Both Method B and MapVic DOC models are as described in Equation 3.2 and Equation 3.3, as shown below.

$$DOC_{Method\ B} = 237.31 - 190.14(NDVI) - 142.66\left(\frac{\rho_7}{\rho_6}\right) \quad (3.2)$$

$$DOC_{MapVic} = 113.80 - 88.41(NDVI) - 67.71(GVMI) \quad (3.3)$$

GVMI is Global Vegetation Monitoring Index, which can be calculated as shown in Equation 3.4. The reflectance bands ρ_2 , ρ_6 and ρ_7 (band two, six, and seven) are from MODIS reflectance dataset (Ceccato et al., 2002; Martin et al., 2015; Newnham et al., 2010).

$$GVMI = \frac{(\rho_2+0.1)-(\rho_6+0.02)}{(\rho_2+0.1)+(\rho_6+0.02)} \quad (3.4)$$

To assess our DOC estimation model performance with the existing products, we compare both Method B and MapVic model with our model. We evaluate them using the same observed DOC sites. In addition, we also compute recalculated GFDI with both Method B and MapVic DOC and assess their burned area prediction capability.

3.2 Calibrating VOD-NDVI-based DOC estimate models

3.2.1 Multiple Linear Regression Model

In this study, we investigate whether the recently developed, microwave based VOD adds any information to satellite based DOC beyond that embodied in the NDVI (optical based product) using a multiple linear regression model. Initially, we investigated modified forms of NDVI, such as RG, since they have better correlation with DOC per Newnham et al. (2011). Note that we did not attempt to compare the other proposed

alternative, the spread based RG, but only range based (per pixel) RG. In Newnham et al. (2011), while range based RG performance is not as good as preferred spread based RG ($r^2 = 0.62$ and $RMSE = 14.2\%$), it is still better than plain NDVI (NDVI had $r^2 = 0.50$ and $RMSE = 16.4\%$, while 2.5 years range based has $r^2 = 0.57$ and $RMSE = 15.1\%$). Note that while we cannot exactly reproduce the 10 year time range Newnham et al. (2011) used, since our study time frame is 9 years, we tried various 2.5 years time ranges that overlapped with Newnham et al. (2011) study period. However, given the same observed DOC data and NDVI dataset, we were unable to reproduce a result where the RG correlation with DOC is stronger than NDVI. Further analysis showed that the RG results were very sensitive to the selected time range for the computation, such that results were inconsistent with relatively small differences in the selected range. Due to this, RG is not used in this study and NDVI is used directly in forming a multiple linear regression model to estimate satellite based DOC.

Our preliminary analysis revealed that the VOD anomalies, computed from the difference between VOD and average VOD over a specified temporal range, yields the best correlation with DOC, but only if the VOD anomalies are computed from the range matching the in situ DOC observation range for each specific site. The range selection for computing VOD anomalies can be quite problematic, since it can heavily influence the correlation result, and no pattern could be found for determining an appropriate VOD range for any other locations outside the observed DOC sites. Thus, we focus our analysis on using the absolute VOD value. The linear regression equation for DOC and VOD correlation can be expressed as Equation 3.5, where a and b are the intercept and slope of the relationship.

$$DOC = a + b(VOD) \tag{3.5}$$

Utilising both VOD and NDVI datasets, the following multiple linear regression equation for estimating DOC can be expanded from Equation 3.5 as Equation 3.6.

$$DOC = a + b(VOD) + c(NDVI) + d(VOD)(NDVI) \tag{3.6}$$

Here a , b , c , and d are the intercept and coefficients of VOD, NDVI and the product of VOD and NDVI (interaction term), respectively. Using a stepwise regression, the calibrated final model with corresponding coefficients can be determined. The stepwise fit algorithm used here selects the significant terms with the lowest p-value, which is

smaller than the entrance tolerance, to be included in the model first. Next, the algorithm chooses the next most significant term that is still less than the entrance tolerance. This process is repeated until either there are no remaining significant terms or all terms are included in the final model (Draper and Smith, 1998).

3.2.2 Observed DOC Site Selection

To build up robust relationships between the site observed DOC and satellite signals, several site selection criteria were applied. Sites meeting these criteria were used for calibration in the VOD and NDVI based DOC estimation models, while all valid records were used for evaluation.

There are several factors considered in the site selection. First is the land use type of the observed DOC site. The 0.05° land cover type map (MCD12C1) is used for classifying the site location land cover (Hansen et al., 2000). Since 0.1° VOD pixel is covered by 2 x 2 0.05° land cover pixels, the corresponding 2 x 2 pixels of land cover type for each observed DOC site can be acquired. The land cover type and homogeneity of each observed DOC site can then be determined, where the site is considered to have a homogeneous land cover only if all four land cover pixels corresponding to the VOD pixel are the same. In case of a site with heterogeneous land cover type, the dominant land cover with the most pixels out of four will be considered as the representative land cover. All observed DOC sites can be categorised into the following land cover types: evergreen broadleaf forest, open shrubland, savannas, woody savannas, grasslands, croplands, and urban. According to the land use information for each 0.1° VOD pixel, sites identified as evergreen broadleaf forest pixels were removed from the analysis. There are three out of 37 sites situated in the evergreen broadleaf forest, which are Darnum, VIC (mixed grass), Simcocks, WA (improved pasture), and Neerim South, VIC (mixed grass). Even though actual locations of all observed curing sites were in grassy areas, the VOD signal is a mixture of grassland and forest when the sites are surrounded by dense forests within the same 0.1° pixel.

All sites were also examined to ensure a negative correlation between VOD and the in situ DOC data. That is, since VOD is a proxy for water content in above ground biomass, an overall negative correlation between VOD and curing is expected. If this is not the case, then there is likely some other activity within the 0.1° pixel that disrupts this basic relationship; this effect was found in three sites (Durran Durra, NSW (native grass),

Monaro, ACT (improved pasture), and Parry Lagoons, WA (native grass)). The sites without the negative correlation with VOD also had no correlation with NDVI suggesting other land cover types were dominating the signal. Thus, six out of 37 sites are excluded from the analysis.

In addition, there are eight sites (Umbigong, ACT (native grass), Kilcunda, VIC (improved pasture), Tooradin, VIC (improved pasture), Tooradin North, VIC (improved pasture), Caldermeade Park, VIC (improved pasture), Kaduna Park, VIC (improved pasture), Hobart Airport, TAS (native grass), and Jerona, QLD (native grass)) in which VOD data are not available. Most of these are due to sites being located near the coast or a large body of water, where the VOD signal is strongly influenced by the water itself. With the remaining 23 out of 37 sites, several site selection criteria were applied for the calibration phase. The criterion used here to maintain consistency in observation time series requires sites to have at least eight consecutive records, where records are considered consecutive when they are separated by no more than 15 days. Only the consecutive series of records within the selected sites are included in the analysis for the calibration phase. This ensures that the derived model contains the temporal evolution of DOC within years. Only five out of 23 sites are retained for this group, containing a total of 122 (out of 238 total) observations. The selected sites are: Majura, ACT (improved pasture), Tidbinbilla, ACT (mixed grass), Ballan, VIC (improved pasture), Murrayville 1, VIC (native grass), and Murrayville 2, VIC (improved pasture). Multiple linear regression models of VOD and NDVI were then calibrated with the observed curing from the final selected sites.

3.2.3 Calibration Results

Across all selected observed DOC sites (excluding the forest areas) from July 2002 to June 2011, the r^2 of VOD and NDVI is 0.52 with an RMSE of 0.11. Using the linear model, as described by Equation 3.5, the DOC and VOD correlation result has a significant relationship and an r^2 of 0.20 with RMSE of 20.80%. The scatter plot showing the correlation between VOD, NDVI and combined VOD and NDVI terms are as shown in Figure 3. 1, while Figure 3.2 shows the residual DOC unexplained by NDVI (differences between observed DOC and NDVI-based DOC) against VOD and combined VOD and NDVI terms.

However, at this level of r^2 , VOD alone is not reliable enough to estimate DOC, especially across Australia in general. The study of Newnham et al. (2011) indicated that NDVI alone can perform better at estimating DOC, with an r^2 of approximately 0.50 for a DOC and NDVI linear relationship. The combined explanatory power of NDVI and VOD is explored using a multiple linear regression analysis, as expressed by Equation 3.6. The first final model includes the VOD and NDVI interaction (d) and NDVI (c) terms, and is as shown in Equation 3.7. The calibrated r^2 for this model is 0.67 with RMSE of 13.40%. VOD was excluded as a predictor in the first final model, as expressed in Equation 3.7, because during the stepwise regression, when the NDVI and (VOD)(NDVI) terms are included as the first and second predictors, the VOD term does not contribute in improving the final model prediction (i.e. p-value exceeds the acceptance threshold, preventing overfitting). When the NDVI term is excluded, the (VOD)(NDVI) term is included first, followed by the VOD term, as expressed in the second final model, shown in Equation 3.8. The second final model has a calibrated r^2 of 0.54 and RMSE of 15.95%. Table 3.1 shows the correlation results for both models. Scatter plots for both DOC models calibration, all sites evaluation, and independent sites evaluation are as shown in Figure 3.3.

$$DOC_1 = 145.57 - 260.82(NDVI) + 137.19(VOD)(NDVI) \quad (3.7)$$

$$DOC_2 = 48.70 + 147.60(VOD) - 259.95(VOD)(NDVI) \quad (3.8)$$

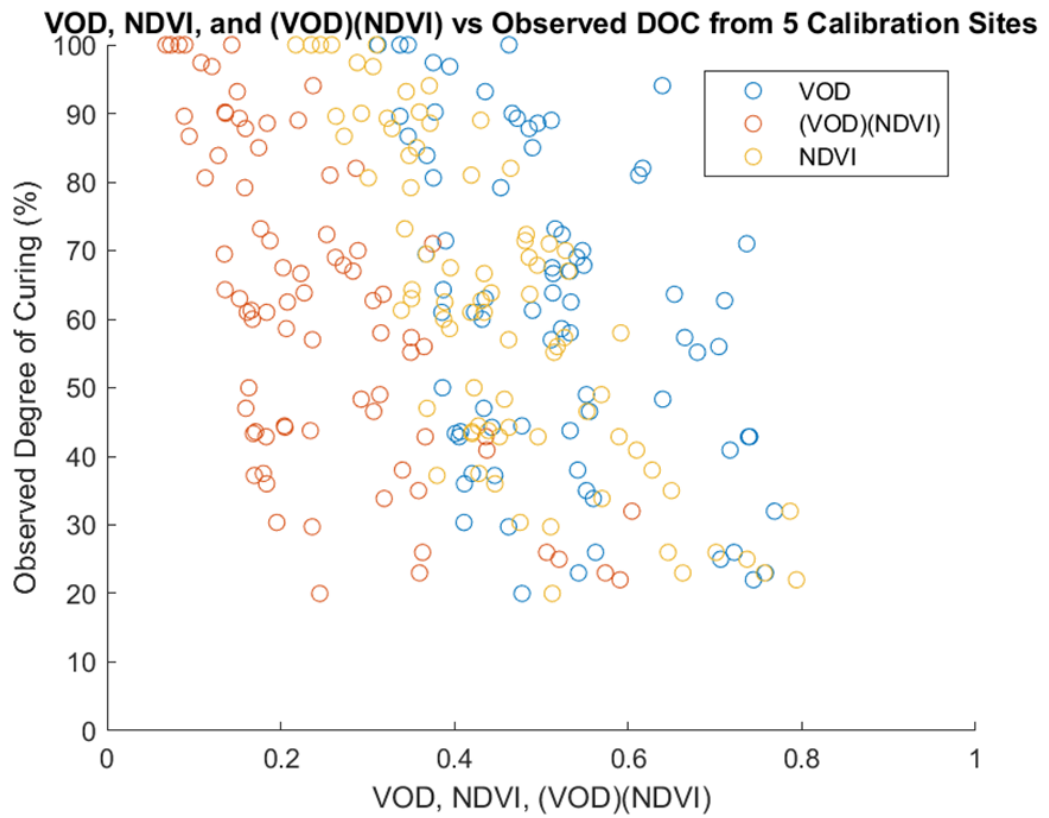


Figure 3.1 Scatter plot of observed degree of curing (DOC) from five calibration sites against VOD, NDVI, and combined VOD and NDVI terms.

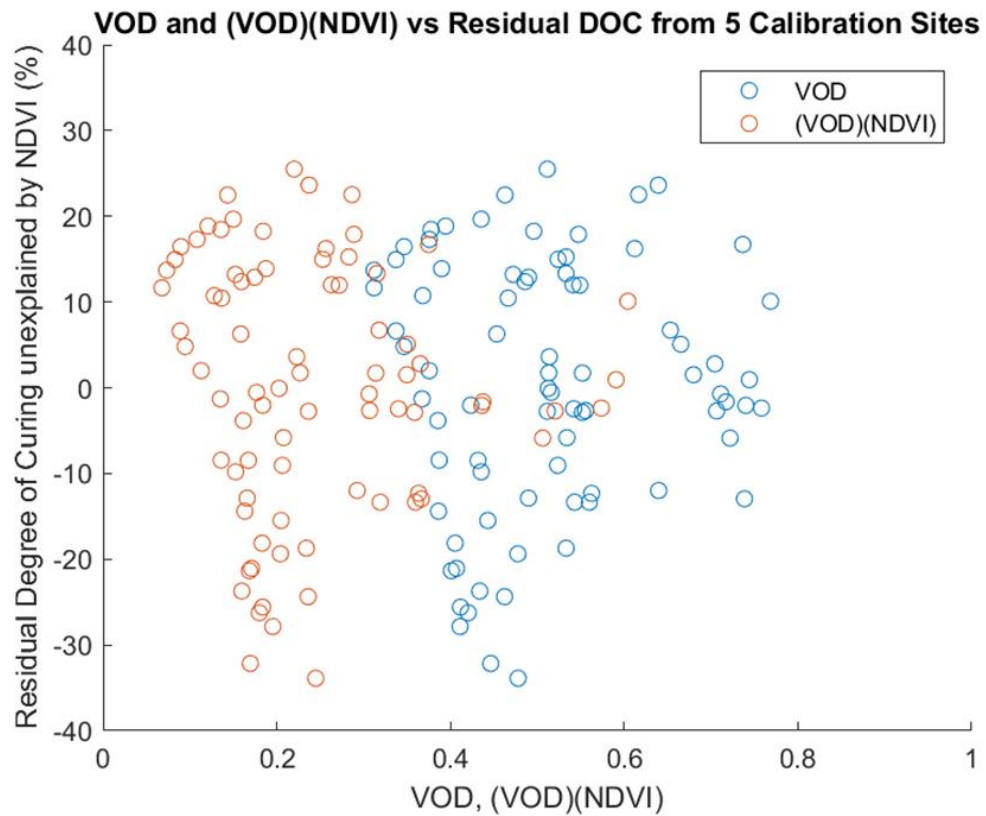


Figure 3.2 Scatter plot of residual observed degree of curing (DOC) from five calibration sites that are unexplained by NDVI against VOD and combined VOD and NDVI terms.

Table 3.1 Calibration and evaluation of satellite based degree of curing (DOC) model derived from Vegetation Optical Depth (VOD) and Normalised Difference Vegetation Index (NDVI). Existing estimated DOC models, Method B (Newnham et al., 2010) and MapVic (Martin et al., 2015), evaluations are also listed below.

Model	Calibration (5/23 sites; 112/238 observations)		All Sites Evaluation (23/23 sites; 238/238 observations)		Independent Sites Evaluation (18/23 sites; 126/238 observations)	
	r ²	RMSE	r ²	RMSE	r ²	RMSE
First DOC-VOD-NDVI Model [Eq. (3.7)]	0.672	13.396	0.550	15.254	0.443	16.760
Second DOC-VOD-NDVI Model [Eq. (3.8)]	0.536	15.950	0.503	15.952	0.542	15.527
Method B [Eq. (3.2)]	N/A	N/A	0.611	14.438	0.632	11.924
MapVic [Eq. (3.3)]	N/A	N/A	0.435	19.801	0.562	14.682

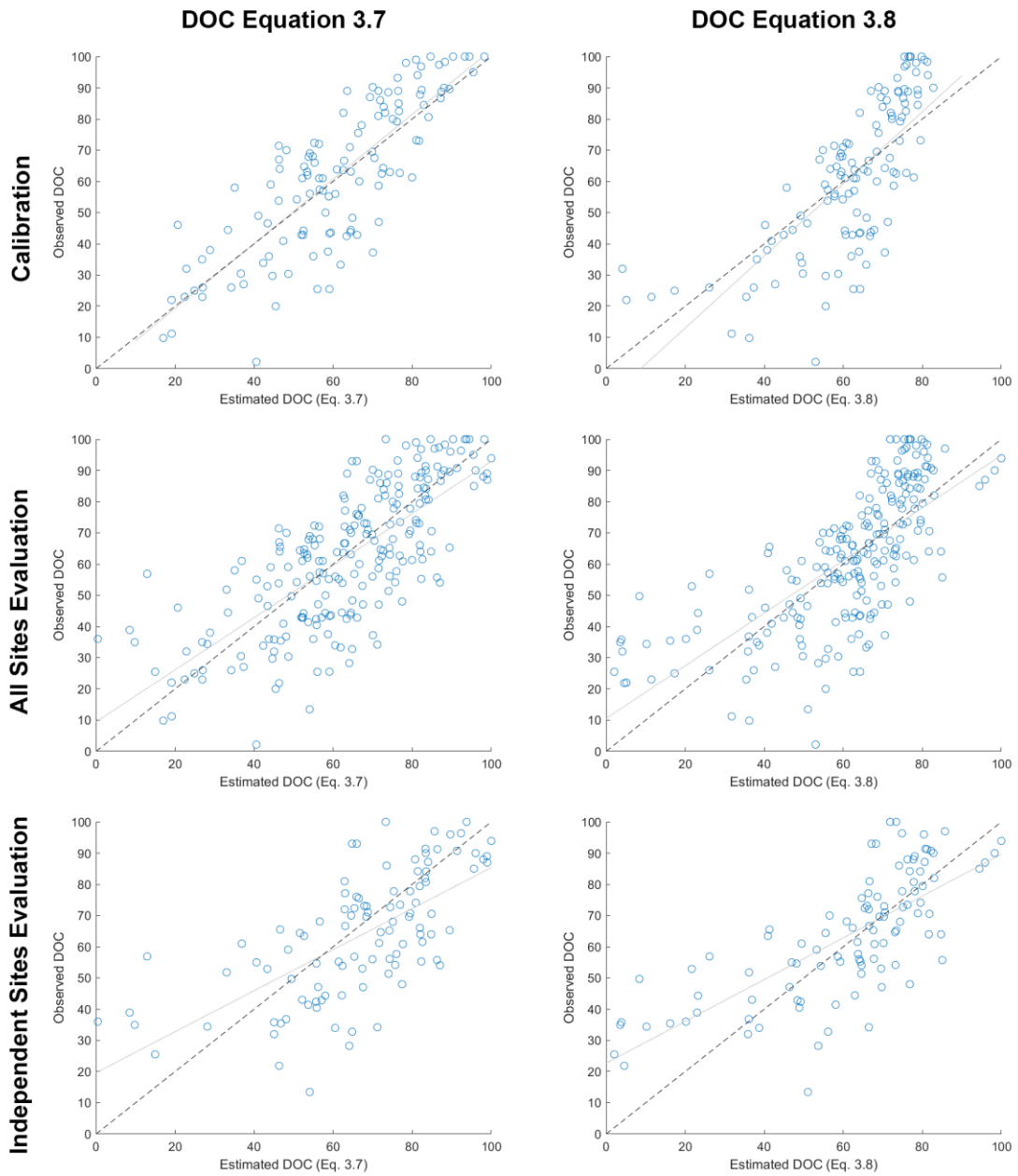


Figure 3.3 Scatter plots between observed and estimated degree of curing (DOC) from the first (Equation 3.7) and second (Equation 3.8) models during calibration, all sites evaluation, and independent sites evaluation stage, corresponding to the information in Table 3.1; dash line represent idealise 1:1 line (perfect fit) while grey solid represent the best fit.

3.3 Evaluating VOD-NDVI-based DOC Estimate Model

3.3.1 Evaluation Results

The DOC models are then evaluated with all (23) valid observed DOC sites and independent (18) observed DOC sites (excludes 5 sites that were used in calibration). The evaluation results for the first model are also shown in Table 1, where the evaluated r^2 is 0.55 and 0.44 with RMSE of 15.25% and 16.76% for all sites evaluation and independent sites evaluation, respectively. The second model evaluations results have r^2 of 0.50 and 0.54, with RMSE of 15.95% and 15.53% for all sites evaluation and independent sites evaluation, respectively. While the evaluations resulted in degradation in model performance over the calibration in most cases, the independent evaluation of the second model has a slightly better evaluation performance.

These results can be compared to those obtained using existing remotely sensed DOC estimates which are also shown in Table 3.1. The MapVic DOC has a lower r^2 and higher RMSE, while the Method B DOC has a higher r^2 and lower RMSE when compared with both of our models in all sites evaluation. This indicates that Method B has the best evaluation among the three models, while MapVic is the worst, and our models sit in the middle between the two. However, during an independent sites evaluation, both models with VOD have the worst performance (lowest r^2 and RMSE). This result is not entirely surprising as all the observations used here were also used in the calibration of Method B (Newnham et al., 2010), a subset is used in the calibration of our method, and MapVic was developed using an independent visual estimates dataset. That is, there is no independent data available for testing Method B, while both our method and MapVic are being tested against independent data. While our first and second models do not have obvious advantages over one another, since the second model only performs better than the first in independent sites evaluation, we decided to pick the first model as our representative model for further comparison with the existing models from this point, since the terms in the first model were selected based on stepwise fit regression with none of our interference (we intentionally removed NDVI term in the second model before applying the stepwise fit regression).

3.3.2 *Spatial and Temporal Variability*

Using the relationship between VOD, NDVI, and observed DOC from the first model, as stated in Equation 3.7, we calculated satellite based DOC for Australia. Figure 3.4 presents maps of satellite based DOC data averaged over the summer periods (December, January, February) for the years 2002-2003 and 2010-2011. From mid-2002 to mid-2011, the overall average DOC for the Australian summer period is the highest during 2003 and the lowest during 2011. Note that the pixels that are classified as any forest types are masked out in white. Comparison time series between satellite based and site observed DOC at Silent Grove, WA (same location as shown in VOD and NDVI example comparison in Figure 2.1) is also shown at the top of Figure 3.4 as an example. Note that the continental mean of DOC across Australia from mid-2002 to mid-2011 is 85.70%.

To determine the amount of spatial variation in DOC across Australia, we computed the standard deviation of all valid DOC estimates across the continent within a single time step. The spatial variation time series can then be plotted for the available time period of mid-2002 to mid-2011, as shown in Figure 3.5. Note that the continental mean spatial DOC standard deviation is 20.39%. This indicates that there is significant spatial variability in DOC that persists across all years, and contains a small seasonal component. For a normally distributed variable, 95% of values would lie within two standard deviations, which is $\pm 40.78\%$ in this case. Further analysis on DOC spatial standard deviation are as shown in Table 3.2. This includes seasonal, monthly, and land cover type spatial standard deviation of DOC. From both seasonal and monthly spatial standard deviation of DOC, it is shown that DOC has the highest spatial variation during winter, which is especially true for northern Australia (Anderson et al., 2011).

In addition, based on time series of satellite based curing data, Figure 3.6 reveals the spatial distribution of standard deviations calculated for each pixel. It shows that most of the strong temporal variation occurs in the south, especially in the southeast and southwest of Australia. Several areas in the midcontinent that have unexpectedly high variation are likely due to rare inundation events. The continental mean temporal standard variation is at 11.88%. Together, Figure 3.5 and 3.6 show the variability in DOC that will impact calculations of fire danger indices.

Though an earlier study for estimating DOC directly with NDVI yielded even smaller RMSE of up to 6.3%, that particular study is focused on data from only three different sites, within a limited study area of 1 km² (Dilley et al., 2004). Older studies that have used NDVI data derived from the National Oceanic and Atmospheric Administration's (NOAA) Advanced Very High Resolution Radiometer (AVHRR) have the same problem of interference from clouds and atmospheric effects, but do not have the advantage of high resolution offered by MODIS (0.05° for AVHRR, but 0.005° for MODIS), or the advantage that VOD is not affected by clouds or aerosol interference.

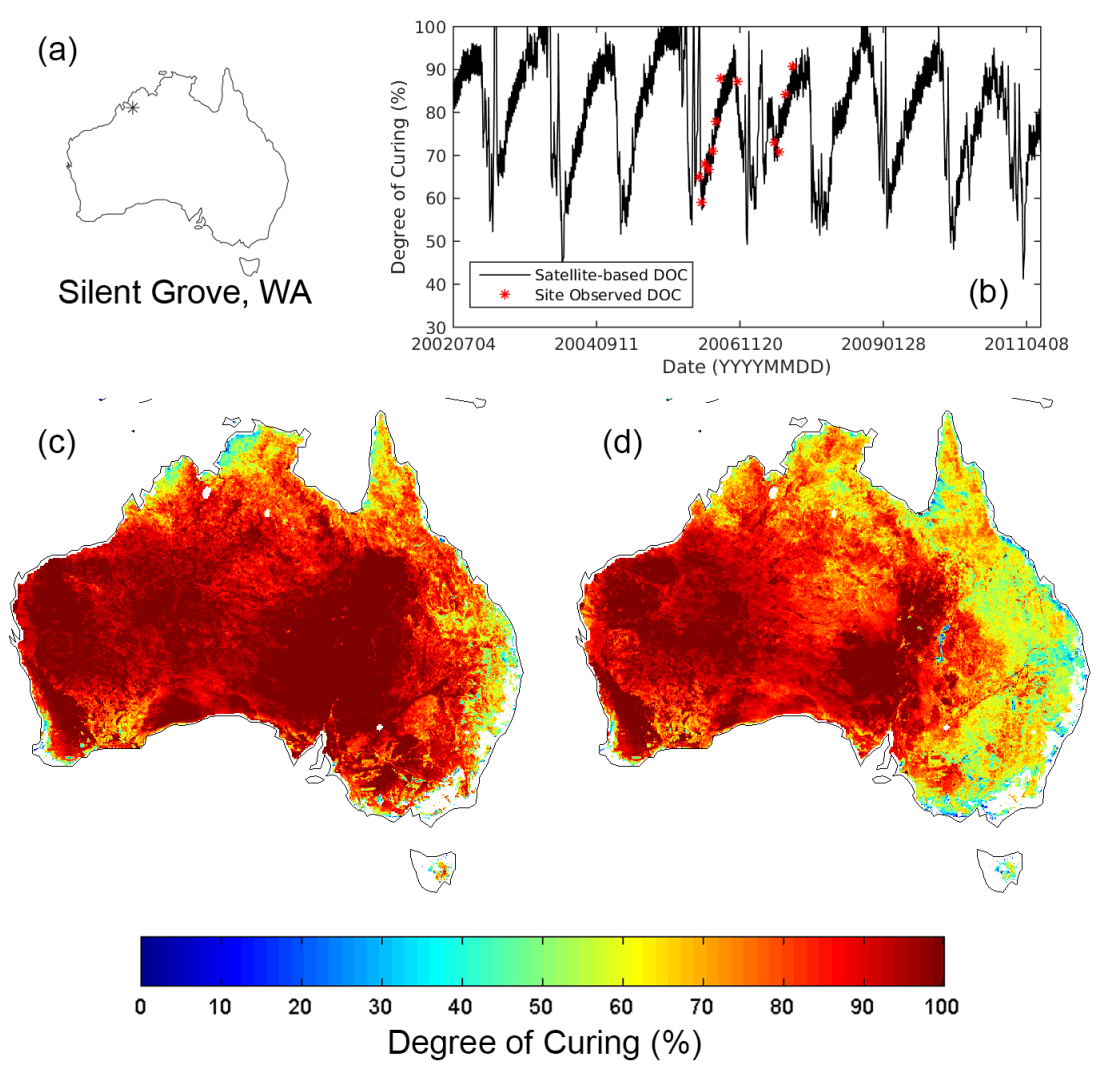


Figure 3.4 Example satellite based and site observed degree of curing (DOC) time series comparison at Silent Grove, WA (17.131° S, 125.374° E) (b), where the star (*) indicate the location of the time series on Australia map (a). Satellite based DOC across Australia during summer (December, January, February) for 2002-2003 (c) and 2010-2011 (d) are shown with forest areas masked out.

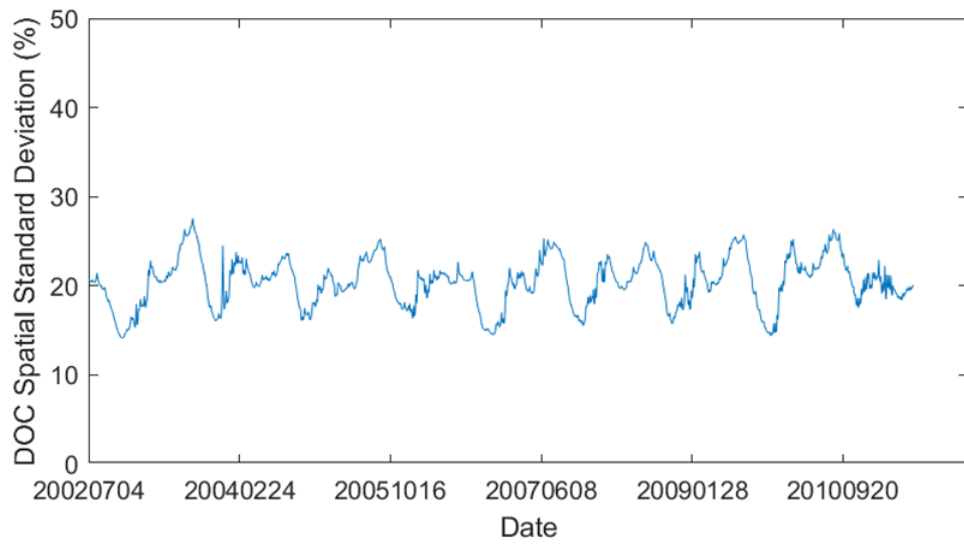


Figure 3.5 Spatial standard deviation of estimated degree of curing (DOC) time series from 4 July 2002 to 26 June 2011.

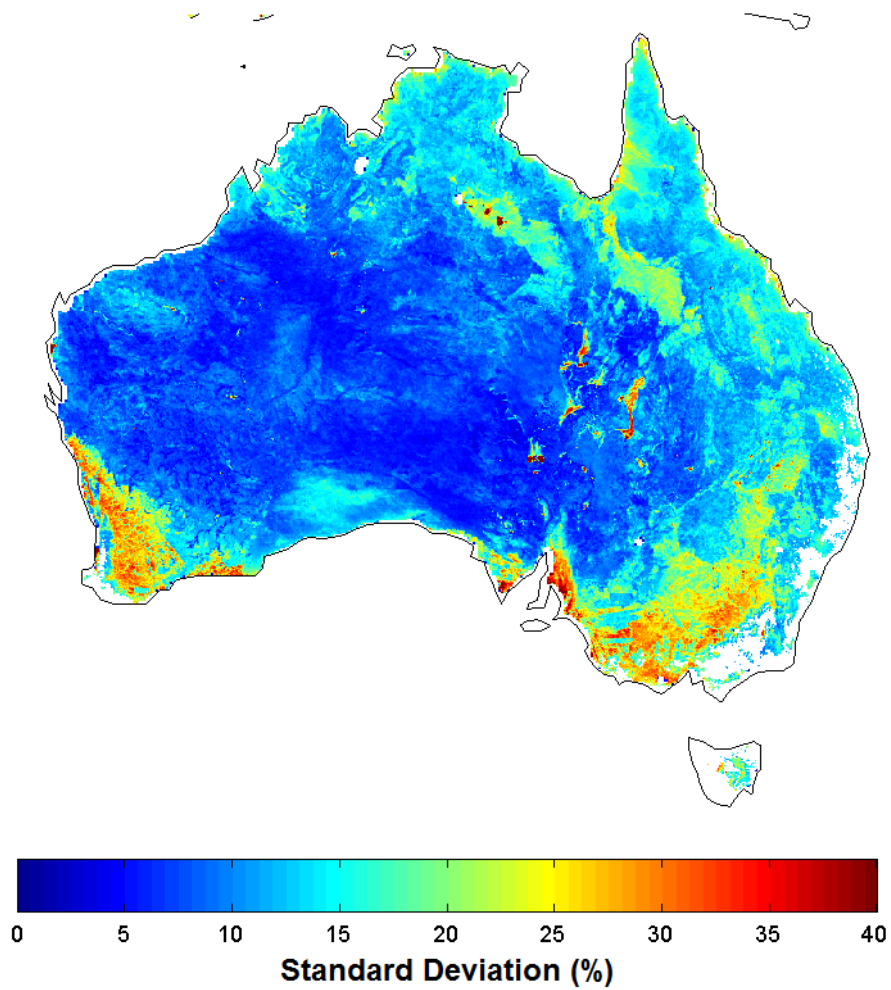


Figure 3.6 Temporal standard deviation of estimated degree of curing (DOC) map from 4 July 2002 to 26 June 2011.

Table 3.2 Spatial standard deviation of estimated degree of curing (DOC) by season, month, and land cover type from 4 July 2002 to 26 June 2011.

DOC Spatial Standard Deviation					
Season	Spatial SD (%)	Month	Spatial SD (%)	Land Cover Type	Spatial SD (%)
Autumn (MAM)	20.636	January	19.050	Closed Shrublands	11.484
Winter (JJA)	22.895	February	21.354	Open Shrublands	13.982
Spring (SON)	18.861	March	21.167	Woody Savannas	17.912
Summer (DJF)	19.161	April	20.228	Savannas	13.432
		May	20.498	Grasslands	19.105
		June	21.770	Croplands	20.995
		July	23.231		
		August	23.634		
		September	21.971		
		October	18.305		
		November	16.325		
		December	17.276		

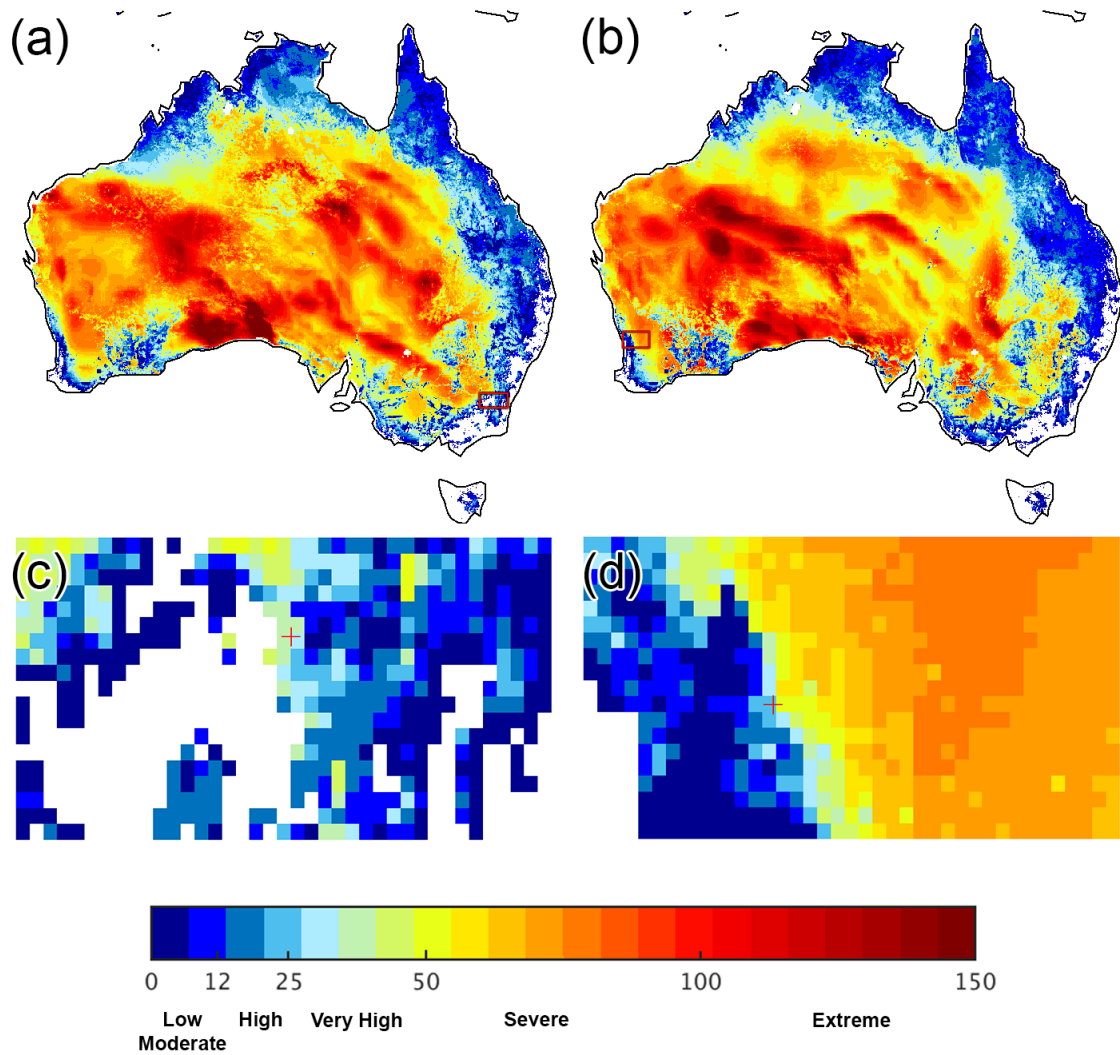
3.4 Comparing GFDI Derived From VOD-NDVI-based and Existing DOC Estimation

3.4.1 Calculating GFDI

GFDI can be calculated as described in Equation 1.1 and 1.2. The spatial plot for maximum summer recalculated GFDI from the DOC multiple linear regression model is shown in Figure 3.7, where the top row (a) and (b) are the maps for summer 2003 and summer 2010, respectively. The magnified regions for example fire events in Weston Creek, ACT 2003 and Toodyay, WA 2010 events can be seen in the bottom row (c) and (d). The fire locations are marked with a red crosshair. White pixels are forest areas that were masked using the land cover map. Overall, summer 2003 has 4.51% more areas indicated as severe or higher GFDI than summer 2010. MCD64A1 burned area map (Figure 3.8) also suggested that summer 2003 had 91.45% more severe wildfire counts than summer 2010. It should be noted that high GFDI values do not guarantee a fire as

there is no accounting for ignition sources, rather a higher GFDI value indicates that if a grassland fire were to start it would spread faster compared to low GFDI values, given no fire suppression activity. Further complicating comparison of Figure 3.7 and 3.8 is the presence of prescribed burns that are deliberately done during low to moderate GFDI conditions, and that some fires shown in Figure 3.8 occur in forested areas where GFDI is not applicable. Nevertheless, they provide a picture of the inter-annual spatial variability in both GFDI and burned area.

The time series plots of recalculated GFDI at Weston Creek, ACT, and Toodyay, WA, for the example 2003 and 2010 fire events were produced, and are shown in Figure 3.9. The black line represents the recalculated GFDI from variable DOC, while the dashed, light green line is for original GFDI with constant DOC at 100%. These locations are marked with red crosshair indicators on the spatial maps (Figure 3.7). Note that the original GFDI time series peaks every year, whereas the recalculated GFDI with variable DOC time series shows sudden peaks in the days near major fires. The Weston Creek fire was part of the 2003 Canberra bushfire complex, where multiple fires merged and rapidly propagated from 18-22 January 2003, burning 1,600 km² (McLeod, 2003). The weather conditions on 18 January 2003 were extreme with temperature as high as 40°C and wind exceeding 60 km h⁻¹. The Toodyay fire was much smaller in magnitude, burning just over 30 km² on 29 December 2009. The Weston Creek area is mostly comprised of forest with mixed land cover, whereas the Toodyay area is mostly a mix between croplands and savannas.



Recalculated GFDI

Figure 3.7 Maximum estimated Grassland Fire Danger Index (GFDI) for summer (December, January, February) of 2002-2003 (a) and 2009-2010 (b). Both zoomed areas marked with red bounding boxes for (a) and (b) are shown in (c) and (d), respectively. The fires locations for Canberra fire (c) and Toodyay fire (d) are marked with red crosshair. Forest areas are masked out in white.

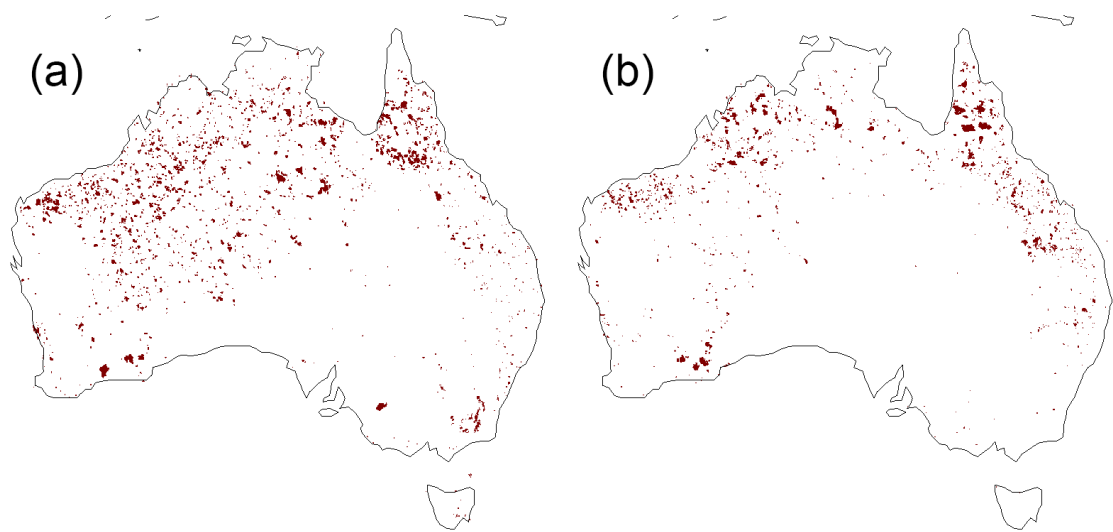


Figure 3.8 MCD64A1 burned area map (Ruiz et al., 2014) during summer (December, January, February) 2002-2003 (a) and 2009-2010 (b) with forest areas masked out.

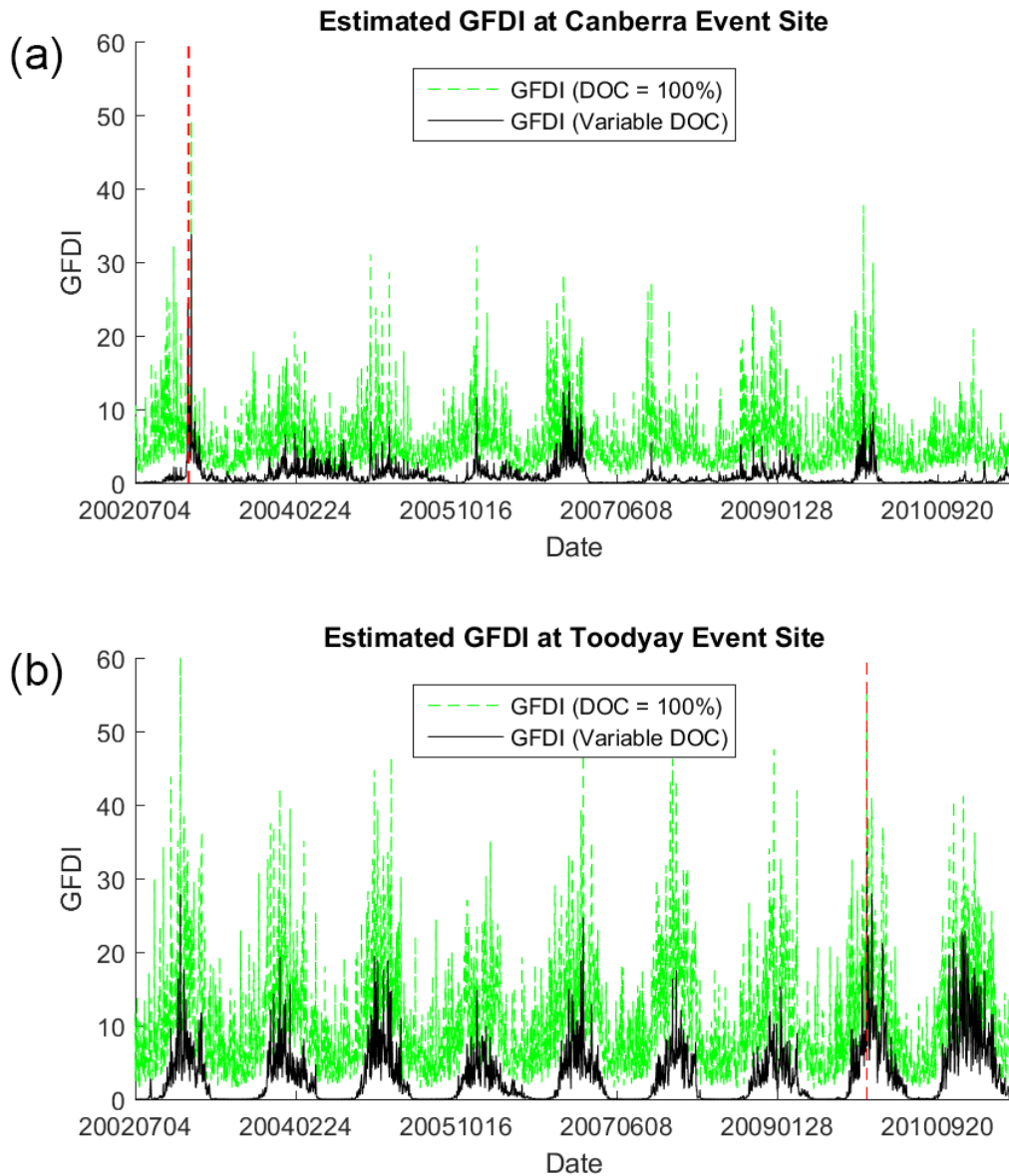


Figure 3.9 Grassland Fire Danger Index (GFDI) time series plot at Weston Creek, ACT, from July 2002 to June 2011 (a) and at Toodyay, WA, from July 2002 to June 2011 (b) where the red vertical dash line indicates the date of fire event on 18 January 2003 for Canberra fire and on 29 December 2009 for Toodyay fire. Solid black line is estimated GFDI time series computed from estimated degree of curing (DOC), whereas green dash line is GFDI time series computed from constant DOC at 100%.

3.4.2 GFDI Severity Level vs Burned and Unburned Areas

By pairing up burned and unburned pixels from burned area observation dataset from MODIS (MCD64A1) with their associated GFDI pixel, we can assess the number of burned and unburned pixels for each GFDI severity level. Using histogram and receiver

operating characteristic (ROC) analysis, the difference between original GFDI with constant DOC at 100% and recalculated GFDI with satellite based dynamic DOC can be assessed (DeLong et al., 1988; Zweig and Campbell, 1993).

Using a burned area observation dataset from MODIS (MCD64A1), we test the effectiveness of GFDI with satellite-based DOC in increasing the probability that fires will occur in high GFDI severity levels compared to the probability that fires will occur in low-moderate GFDI severity levels. Low intensity fires, such as prescribed burned, are removed from the burned area observation by using the FRP provided in MODIS active fire product (MCD14ML) to mask out burned area that have low FRP. We assume any burned area with FRP lower than 100 MW to be unburned (associated with low-moderate GFDI risk). At each burned and unburned daily data point, the corresponding daily GFDI was calculated. The GFDI histogram in Figure 3.10 shows the frequency of satellite based recalculated GFDIs and constant based (DOC = 100%) reference GFDIs over burned and unburned areas. Figure 3.10 shows that the recalculated GFDI places the largest percentage of unburned pixels in the low-moderate GFDI severity class, with ~80 % of all unburned pixels occurring in the low-moderate or high severity classes. Meanwhile the reference (DOC = 100%) GFDI places ~80% of unburned pixels in the high, very high, severe and extreme classes.

We can evaluate the performance in correctly assigning burned and unburned area for both recalculated and reference GFDI by using the concept of ROC. Assume that the MCD64A1 burned area map represents the true condition and that the GFDI severity level represents the predicted condition, where the prediction is positive when GFDI level is classified as high or above for a burned area and low-moderate for an unburned area. Table 3.3 shows the contingency table, including both type I (unburned area with high or above GFDI level; false positive) and type II (burned area with low-moderate GFDI level) errors. Though recalculated GFDI has a lower true positive rate of correctly assigning burned area than reference GFDI (0.86 vs 0.895, it is much better at assigning unburned area correctly, i.e. lower false positive rate (0.38 vs 0.53). Overall accuracy for recalculated GFDI is higher than the reference GFDI (0.62 vs 0.47).

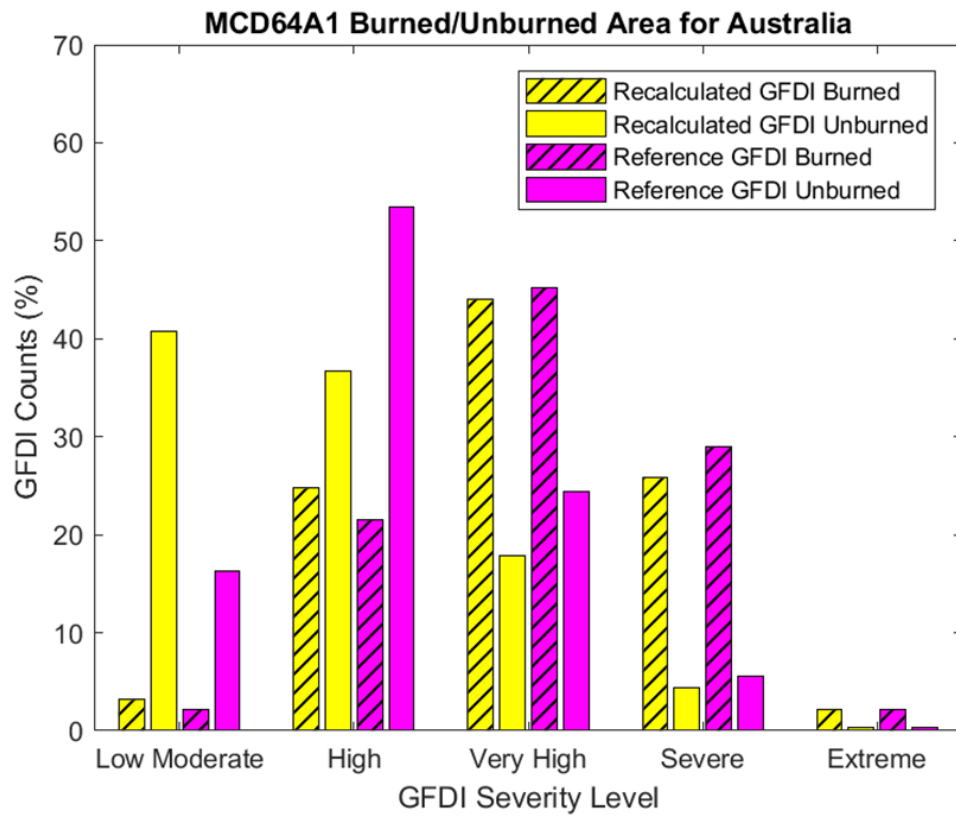


Figure 3.10 Grassland Fire Danger Index (GFDI) severity level histograms at burned and unburned areas over Australia during 4 July 2002 to 26 June 2011 where the dark and light blue shaded bars are recalculated GFDI with satellite estimated variable degree of curing (DOC), while the green and yellow shaded with diagonal hatch bars are reference GFDI with constant DOC at 100%.

Table 3.3 Referenced and recalculated Grassland Fire Danger Index (GFDI) severity and burned-unburned area contingency table for satellite based degree of curing (DOC) derived from Vegetation Optical Depth (VOD) and Normalised Difference Vegetation Index (NDVI). Reference GFDI is computed from constant DOC at 100%, while recalculated GFDI is computed from satellite based DOC.

		Reference GFDI		Recalculated GFDI (First Model – Eq. 3.7)	
		MCD64A1 No. of Pixels			
		Burned	Unburned	Burned	Unburned
GFDI Severity	High or above	88	446,894,217	80	319,386,462
	Low Moderate	5	395,703,734	13	523,211,489

	Reference GFDI	Recalculated GFDI (First Model – Eq. 3.7)
True Positive Rate	0.9462	0.8602
False Positive Rate	0.5304	0.3790
Accuracy	0.4696	0.6210

3.4.3 Comparison with Current DOC Products

Both Method B and MapVic DOC are then used to compute recalculated GFDI and compare with burned area observation dataset in the same manner as our DOC model. From the ROC analysis in Table 3.4 for Method B and MapVic recalculated GFDI, we found that even though Method B has the best DOC evaluation results (highest r^2 , lowest RMSE) and highest overall recalculated GFDI burned and unburned detection accuracy at 0.84, it is the worst at detecting burned area correctly with a true positive rate of only 0.10. This concurs with the findings in Newnham et al. (2010) who found Method B to consistently under predict DOC, and hence it produces fewer cases of high or above GFDI severity.

Though the overall recalculated GFDI from Method B DOC is the best (overall accuracy from best to worst is 0.84 for Method B, 0.62 for our DOC model, 0.59 for MapVic, and 0.47 for GFDI with 100 % constant DOC), we found that it is the worst at detecting burned area correctly (true positive rate from best to worst is 0.94 for GFDI with 100 % constant

DOC, 0.89 for MapVic, 0.86 for our DOC model, and 0.10 for Method B). Our model is in the middle ground between Method B and MapVic in terms of overall accuracy.

Table 3.4 Recalculated Grassland Fire Danger Index (GFDI) severity and burned-unburned area contingency table for degree of curing (DOC) computed with Method B (Newnham et al., 2010) and MapVic (Martin et al., 2015) model. Reference GFDI is computed from constant DOC at 100%, while recalculated GFDI is computed from satellite based DOC.

		Method B GFDI		MapVic GFDI	
		MCD64A1 No. of Pixels			
		Burned	Unburned	Burned	Unburned
GFDI Severity	High or above	9	131413937	83	334095499
	Low Moderate	84	693718749	10	488464724

	Method B GFDI	MapVic GFDI
True Positive Rate	0.0968	0.8925
False Positive Rate	0.1593	0.4061
Accuracy	0.8407	0.5938

3.5 Limitations

It is worth noting here that in an operational setting atmospheric interference by clouds or smoke will cause gaps in the optical and near-infrared (NDVI) data, while the VOD data remains unaffected. We also note that while the VOD data use here was derived from the AMSR-E sensor, which is no longer operational, VOD data derived from currently operating passive microwave sensors, such as Advance Microwave Scanning Radiometer 2 (AMSR2), could be used in an operational setting.

Reducing the chance of incorrectly assigning unburned and burned areas correctly from the ROC analysis made here is purely based on using the burned area map as a true baseline. However, the burned area map may include fires that are deliberately lit in low-moderate conditions, such as prescribed burns and fires that the GFDI is not designed for, such as a fire that burns in forested regions. Prescribed burns and low intensity fires

are however minimised by applying low FRP threshold, using information from the MODIS active fire product. The ROC analysis result here is only used to reinforce the idea that using the reference GFDI with constant curing (100%) leads to overestimating GFDI in some situations, and might result in misleading fire danger warnings.

The satellite based DOC produced here is also at a moderate spatial resolution, which is a limitation of many satellite products. However, DOC in reality can vary over spatial scales much finer than the satellite footprint (less than 0.05°). As such, our model should only be used as a guide for dynamic, near daily assessment of grassland curing at coarse to moderate spatial scales. This is also true for other satellite based DOC models, including Method B and MapVic models.

4 Estimated Fuel Load with Satellite Data

In this chapter, I developed a regression based model for estimating the amount of wildfire fuel load over Australia. The aim here was to produce moderate resolution, temporally varying, gridded fuel load dataset over Australia based on a microwave satellite vegetation product. To achieve this, I produced gridded annual estimated AGBC using VOD based on the technique of Liu et al. (2015). AGBC computed from VOD has been used in various applications, such as assessing the impact of climate and deforestation on the Amazon Basin's AGB (Exbrayat et al., 2017), assessing the greening of the South China Karst (Brandt et al., 2018), and evaluating an even more recent 1.4 GHz (L-band) VOD over biomass in Africa (Rodríguez-Fernández et al., 2018). Other similar usage of VOD, such as linking the VOD to gross primary production (Teubner et al., 2018), is also based on the methodology behind VOD based AGBC. Then, using gridded annual AGBC along with observed fuel load data, I calibrated the fuel load prediction model. Due to the limited records of the available observed fuel load data, there was no remaining independent data for model evaluation. Thus, I used a vegetation structure dataset to evaluate AGBC dataset as a proxy to evaluating the estimated fuel load data.

4.1 Observed Fuel Load Data

4.1.1 *Site-based Fuel Load*

Site observation fuel load datasets were gathered from BNHCRC and CFA for field measurements in South Australia and Victoria, respectively. These observed fuel loads were recorded once at each site rather than a consistent record every day or month, hence, each site usually had only single record rather than a time series illustrating fuel load dynamics over time. The aim here was to find a relationship between site-based fuel load and AGBC computed from modified monthly mean of persistent component of VOD in grassland areas. Thus, only grassland fuel load records were extracted. 18 valid fuel load records with record date ranging from early-2013 to early-2015 were collected from grassland fuel beds (9 from South Australia and 9 from Victoria). Note that since the observations were collected outside the temporal range of AMSR-E (mid-2002 – late-

2011) VOD availability, I used AMSR2 (mid-2012 – present, with similar specification to AMSR-E) VOD to calculate AGBC instead. Note that AMSR2 is an AMSR-E successor and have a very similar specification. It was found that some sites were located nearby each other, resulting in multiple sites falling into the same VOD 0.1° pixel. The fuel load variations within the same VOD pixel can be as high as 3 t ha⁻¹. This high variability in site observations introduced uncertainty in the representativeness of the point based site observations to the mean fuel load over a VOD pixel. Note that site-based fuel load (both from BNHCRC and CFA) are only used for initial fuel load estimation approach described in Section 4.2.1.

4.1.2 *Bioregion Based Fuel Load*

Bioregion fuel load data was obtained from a past study on prescribed fire effectiveness within Australian bioregions (Price et al., 2015). There is a total of 31 fuel load records for each corresponding bioregion across New South Wales and Victoria. The dominant vegetation types for 31 bioregions include a variety of forests, woodlands, and hummock grassland. Fuel load levels for 31 bioregions ranged between 0 to 19 t ha⁻¹ with bioregion areas ranging between approximately 12,900 to 427,300 km². The dominant vegetation classes within each bioregion are as described by Native Vegetation Information System framework (NVIS) (Price et al., 2015). The NVIS framework is provided by the Department of the Environment and Energy. The 100 m spatial resolution, gridded NVIS map (version 4.2) was obtained and used as a dominant vegetation filter. Unlike site-based fuel load, a mean AGBC value for each bioregion was compared with each corresponding bioregion fuel load instead of pixel by pixel comparison. AMSR-E VOD was used here for computing AGBC, since the available period was longer than AMSR2 VOD data. Bioregion fuel load is used for fuel load estimation approach described in Section 4.2.2.

4.2 Estimating Fuel Load with Satellite Products

Most of the past studies of fuel load estimation are based on high resolution satellite images, such as Landsat or MODIS products (Brandis and Jacobson, 2003; Jin and Chen, 2012; Reich et al., 2004; Van Linn et al., 2013). As discussed earlier, while these models have an advantage of high spatial resolution (usually ~500 m or higher), their spatial coverage is limited to at most a regional scale. Some of these studies (Jin and

Chen, 2012; Reich et al., 2004) used detailed ground observations from their selected study areas along with high resolution satellite snapshots to construct fuel load models for different aspects of the fuel. Reich et al. (2004) constructed fuel load models for three custom forest fuel classifications with different fuel sizes using multiple linear regression models and binary regression trees. In Jin and Chen et al. (2012), multiple regression models were constructed for different fuel ages and sizes and total fuel based on tree stand characteristics. While these two studies covered multiple fuel types and characteristics, they both required very high spatial resolution satellite dataset and detailed field records of vegetation characteristics, i.e. tree heights, diameter at breast height, etc. Brandis and Jacobson (2003) opted for a more generalised fuel prediction method by only computing remaining litterfalls (fine fuels), but the models also required high resolution satellite data and field observation of tree characteristics. An even more simplified fuel load model was constructed in a study by Van Linn et al. (2013), using NDVI, temperature, elevation, and aspect data as inputs. Note that none of the past fuel load prediction studies were done exclusively for grassland areas.

Since I aimed for total spatial coverage over Australia and at least several years of temporal coverage, I decided to opt for a moderate spatial resolution satellite product (VOD) and a very simplified fuel load prediction model (only total estimated fuel is computed) as a compromise. VOD has previously been shown to provide a good indication of above ground biomass globally (Liu et al., 2015). Since there are no exact methods for estimating fuel load at a continental scale from past studies, I attempted two different approaches in calibrating the fuel load estimation model.

4.2.1 Estimating Fuel Load Using VOD and Site-based Observations

The first method involved using the modified, long term VOD trend to compute AGBC. A brief summary regarding the methodology can be outlined as follows:

1. Compute and separate the long term trend (persistent component) of VOD.
2. Apply a litterfall decay to the decreasing trend of the separated persistent component of VOD.
3. Use the modified persistent component of VOD computed from step 2 to calculate monthly AGBC.
4. Calibrate the fuel load estimation model using AGBC computed from step 3 and site-based fuel load observations described in Section 4.1.1.

To be precise, the first step was to segregate the persistent and recurrent components in the VOD time series. The persistent component represented the base moisture in the vegetation or existing fuel load, while the recurrent component represented the shorter-term weather induced changes in vegetation moisture. The idea of separating persistent and recurrent trends in VOD is based on a past study over Australia that did this using a different vegetation index (Donohue et al., 2009). Only persistent component will be kept for further analysis, while recurrent component will be discarded.

For the second step, it is known that fuel load depends on the vegetation type and the litter accumulation since the last fire (Brandis and Jacobson, 2003; Olson, 1963). Using the persistent component of VOD as a proxy of fuel load, I then applied the litterfall decay function to the decreasing trend in persistent VOD. The idea behind the litterfall decay is that during the decline of vegetation moisture content, the accumulated litter decays according to the decomposition rate rather than being directly related to moisture decreases. The equation for computing the remaining litterfall after decay is as shown in Equation 4.1, where L_{rem} is the remaining litter after time period t ($t \text{ ha}^{-1}$), L_0 is the rate of litterfall, k is the decomposition rate, and t is the period of litterfall (Olson, 1963).

$$L_{rem} = \frac{L_0}{k} (1 - e^{-kt}) \quad (4.1)$$

Note that the decomposition rate (k) is estimated using the litter half-life from past studies of litterfall and organic matter turnover in South Australia, where the half-life of litter from leafy component can range between 1.9 (wet condition) to 4.2 years (dry condition) (Hutson, 1985). Decomposition rate equation is as described in Equation 4.2, where $T_{1/2}$ is the half-life of litter.

$$k = \frac{0.693}{T_{1/2}} \quad (4.2)$$

Using the above litterfall decay and decomposition rate, the persistent VOD with applied litterfall decay on the decreasing trend is computed and referred to modified persistent component.

During the third step, the modified persistent component of VOD was then used to calculate gridded monthly AGBC. Note that the AGBC computation based on VOD is from Liu et al. (2015) study, as discussed in Section 4.2.2. The monthly AGBC was then calibrated with grassland site observed fuel load data from BNHCRC (South Australia)

and CFA (Victoria) in the fourth step. It was intended that this fuel load estimation model for Australian grasslands would have up to monthly temporal coverage in addition to 0.1° spatial coverage over Australia. However, no significant correlation was found between the derived AGBC and grassland site observed fuel load data (only 18 records are from grasslands). There were various possible causes for this including the spatial mismatch between site observations and VOD pixels (0.1° x 0.1° or ~100 km²).

Many variations on this method were attempted, however no satisfactory solution was found when comparing directly with site observations. Thus, this method was deemed to be unsuccessful for creating a fuel load estimation model. The valid approach for calibrating fuel load estimation model is as described in the following Section 4.2.2 and 4.3.

4.2.2 Annual AGBC Estimation Using VOD

The second method was much simpler when compared with the first. Here, annual mean VOD was directly converted to gridded annual AGBC. The annual AGBC was then calibrated with observed fuel load based on Australian bioregions (Price et al., 2015). Using this method yielded a general fuel load model for Australia, but the temporal resolution was reduced to annual, while the spatial resolution was kept at 0.1°. This method yielded a significant correlation between annual mean AGBC and fuel load representing each bioregion.

Calculating AGBC from VOD data was based on a past study on the recent reversal of biomass loss in Australia (Liu et al., 2015). Firstly, since VOD can be affected by RFI and large bodies of water, quality control of the VOD dataset prior to AGBC calculation was needed. The VOD6 (i.e. VOD derived from relatively low frequency of 6.9 GHz) was used as a base for AGBC calculation. A separate RFI mask was then applied over all VOD6 data; this mask contained RFI flags indicating whether the VOD6 pixel is: 1) free of interference, 2) affected by RFI and can be replaced by VOD10 (derived from relatively high frequency of 10.7 GHz), 3) affected by RFI and must be removed, and 4) on large body of water and must be removed.

In the case where the VOD10 pixel was needed as a replacement pixel for VOD6 per RFI mask, the VOD10 to VOD6 conversion equation was required. I established a simple linear relationship between VOD6 and VOD10 by correlating all available daily VOD data

from mid-2002 to mid-2011. The relationship was significant with r^2 of 0.82 and RMSE of 0.087 for AMSR-E VOD. The associated conversion equation for VOD6 replacement pixel is as described in Equation 4.3.

$$VOD6 = 0.0145 + 0.903VOD10 \quad (4.3)$$

Then, the filtered 8 day VOD (VOD6 variant) data was combined into monthly or annual average dataset. In Liu et al. (2015) study, three different relationships between VOD and AGBC were presented for high, mean, and low AGBC estimates. I used mean AGBC estimates, since it had the least RMSE (RMSE = 6.45 t ha⁻¹) and best correlation (r^2 = 0.99). The VOD to AGBC conversion equation is as shown in Equation 4.4 (Liu et al., 2015).

$$AGBC = 0.5[(320.6) \left[\frac{\arctan(9.10(VOD-0.95)) - \arctan(9.10(0-0.95))}{\arctan(9.10(Inf-0.95)) - \arctan(9.10(0-0.95))} \right] + 5.5] \quad (4.4)$$

Using Equation 4.4, the annual AGBC can be computed from monthly or annual average VOD dataset. An example time series comparison between annual average VOD and resultant AGBC at Silent Grove, WA is as shown in Figure 4.1. Note that VOD is unit less value ranging from 0 to 1.3, while AGBC is in t ha⁻¹.

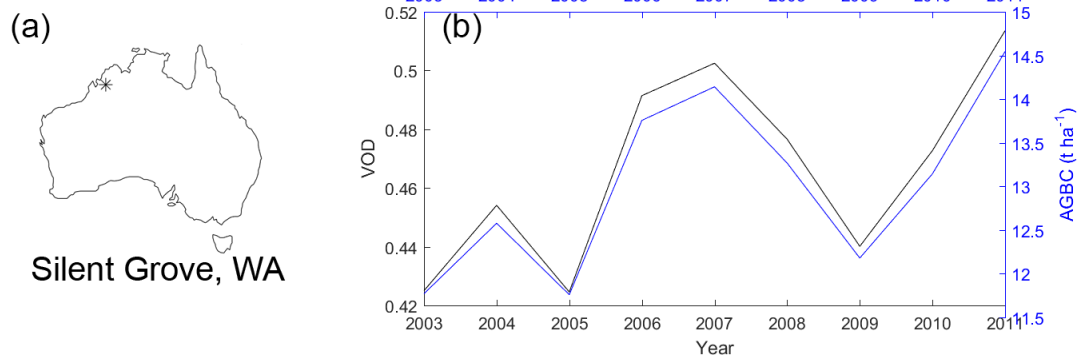


Figure 4.1 Example annual average VOD (black) and AGBC (blue) time series comparison at Silent Grove, WA (17.13° S, 125.37° E) (b), where the star (*) indicate the location of the time series on Australia map (a).

4.3 Fuel Load Model Calibration

Annual estimated AGBC based on VOD was used for calibration with bioregion fuel load. Since each bioregion had a single fuel load value representing a very large area, the mean value of AGBC from 2003 to 2011 at every pixel within the corresponding bioregion area was computed and compared with bioregion fuel load. 29 out of 31 bioregions were used for calibration; the other two regions had no corresponding VOD pixels, since they were located along the coastline and were relatively small. For each bioregion, only AGBC pixels that were located on the dominant vegetation type according to NVIS map was retained for the mean value computation. I tried different types of fitting functions for correlation between bioregion fuel load and AGBC, including linear, polynomial (2nd and 3rd degree), exponential, logarithm, and 2nd order power fitting functions. It was found that an exponential function provided the most significant relationship with r^2 0.74 of and RMSE of 3.26 t ha⁻¹ and also predicted fuel load of approximately 0 t ha⁻¹ when AGBC is at 0 t ha⁻¹. This fuel load prediction equation is as described in Equation 4.5, where Q is fuel load in t ha⁻¹.

$$Q = -18.7e^{(-0.0408AGBC)} + 18.4 \quad (4.5)$$

Note that ignoring the NVIS map (as a dominant vegetation filter) reduced the predicted fuel load model correlation. It should also be noted that this fuel load estimates from Equation 4.5 does not and was never meant to capture any fine variabilities in fuel litters, since a stationary bioregion fuel load map with 29 valid data points is used for the fuel load model calibration (Price et al., 2015). It is also due to the fact that the base VOD product used has a resolution of 0.1° (~100 km² area) as discussed clearly in Section 2.1.1. Variability of fuel elements can occur at very small scales (metres) but the satellite can only see the aggregate signal from all fuel elements within a given pixel.

The uncertainties in the AGBC estimates from VOD are, as described in Liu et al. (2015), measured using RMSE between three different AGBC models. I used the model with the least RMSE (as stated in Section 4.2.2) to minimise uncertainties from estimated AGBC. While this resulted in multiple uncertainties both from estimated AGBC (RMSE = 6.45 t ha⁻¹) and our estimated fuel load (RMSE = 3.26 t ha⁻¹), the scale for fuel load data we produced here is at continental scale with annual temporal interval.

4.4 Fuel Load Model Evaluation

4.4.1 *Spatial and Temporal Variability*

Using Equation 4.5, annual estimated fuel load over Australia can be computed. Example fuel load map for year 2003 and 2011 are as shown in Figure 4.2, where the year 2003 (panel c) has the smallest mean fuel load of 5.88 t ha^{-1} and the year 2011 (panel d) has the largest mean fuel load of 7.17 t ha^{-1} . The year 2003 and 2011 are selected as an example of dry (during the Millennium Drought in Australia from late 1996 to mid-2010) and wet (La Nina period during 2010 to 2011) year, respectively. Example fuel load time series at the same location as shown in Figure 2.1 (Silent Grove, WA) is also shown here in Figure 4.2. The continental mean of fuel load across Australia from 2003 to 2011 is 5.92 t ha^{-1} .

The standard deviation was computed to represent the amount of spatial and temporal variation of fuel load across Australia. For spatial variation, the standard deviation of all valid fuel load estimates was computed within a single time step. An annual spatial variability time series is plotted in Figure 4.3. Here, it can be seen that the annual spatial variability is on an overall increasing trend with 2003 having the lowest and 2011 having the highest spatial variations. The mean standard deviation of spatial variation across all years is 2.50 t ha^{-1} .

For annual temporal variation, the standard deviation was calculated for each pixel across Australia. This temporal variation map is shown in Figure 4.4. While the temporal variations are minimal across mid-continent and along the west coast, there are strong temporal variations along the east coast, especially in Queensland. The mean standard deviation of temporal variation across all pixels is 0.54 t ha^{-1} .

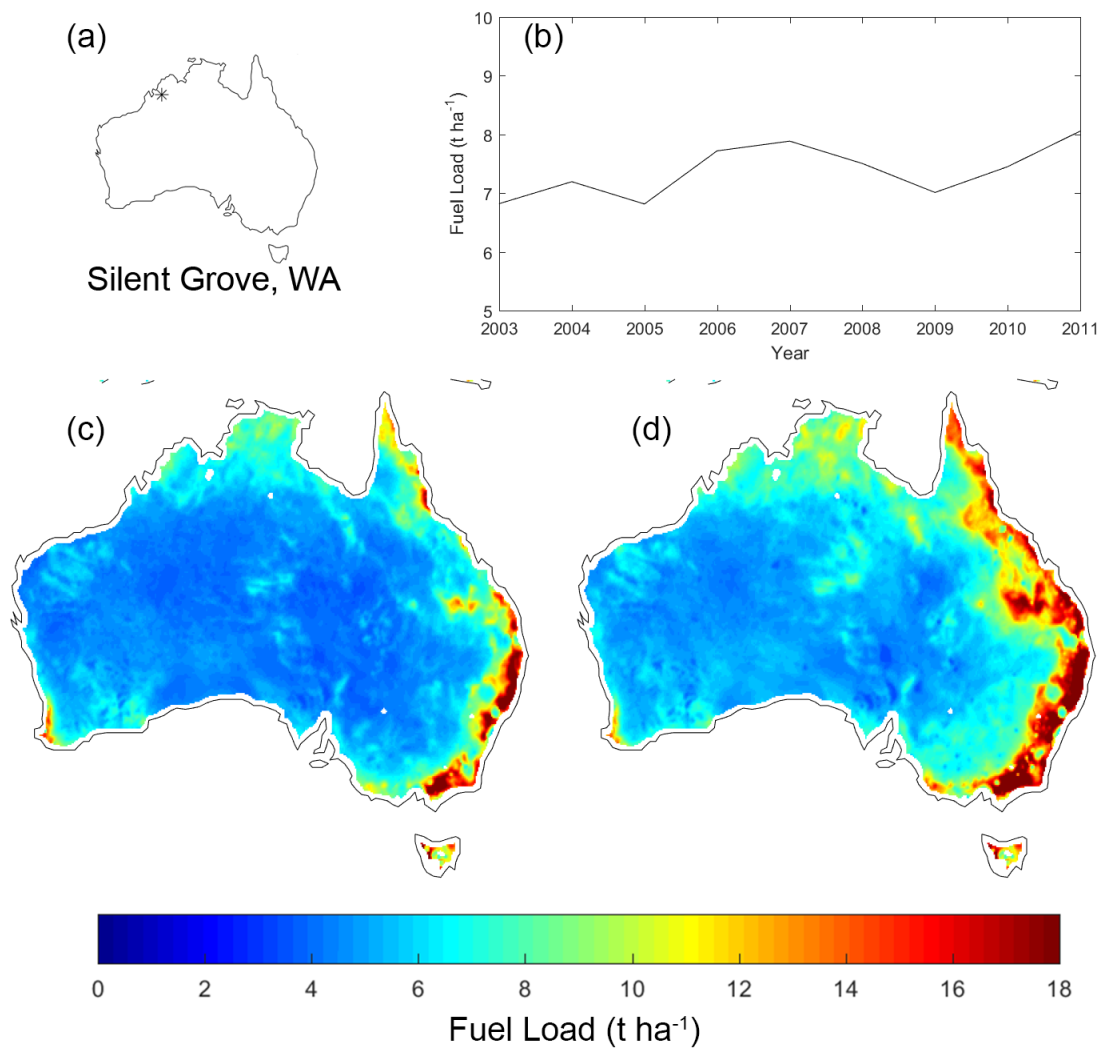


Figure 4.2 Example satellite based fuel load time series comparison at Silent Grove, WA (17.13° S, 125.37° E) (b), where the star (*) indicate the location of the time series on Australia map (a). Annual satellite based fuel load across Australia during 2003 (c) and 2011 (d) are shown.

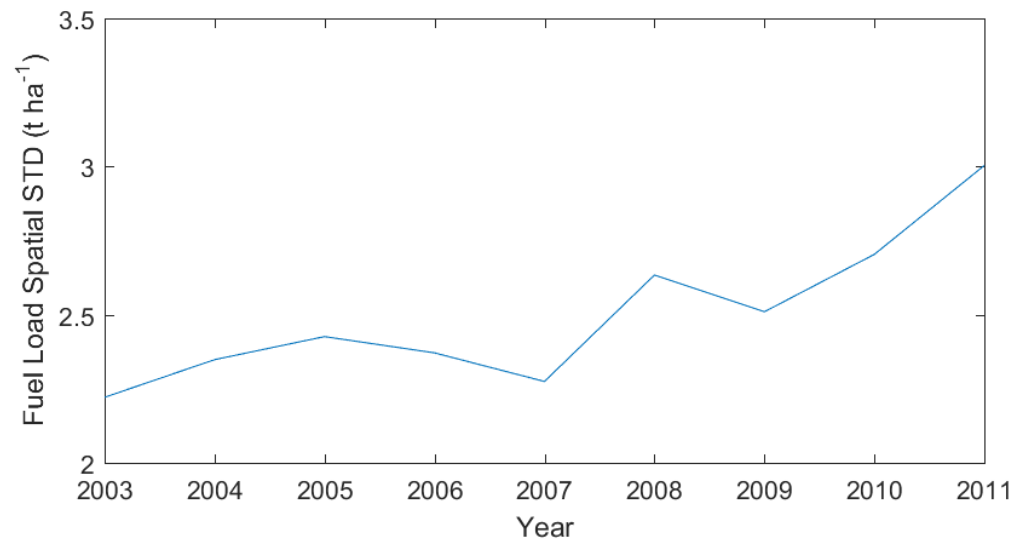


Figure 4.3 Spatial standard deviation of estimated fuel load time series from 2003 to 2011.

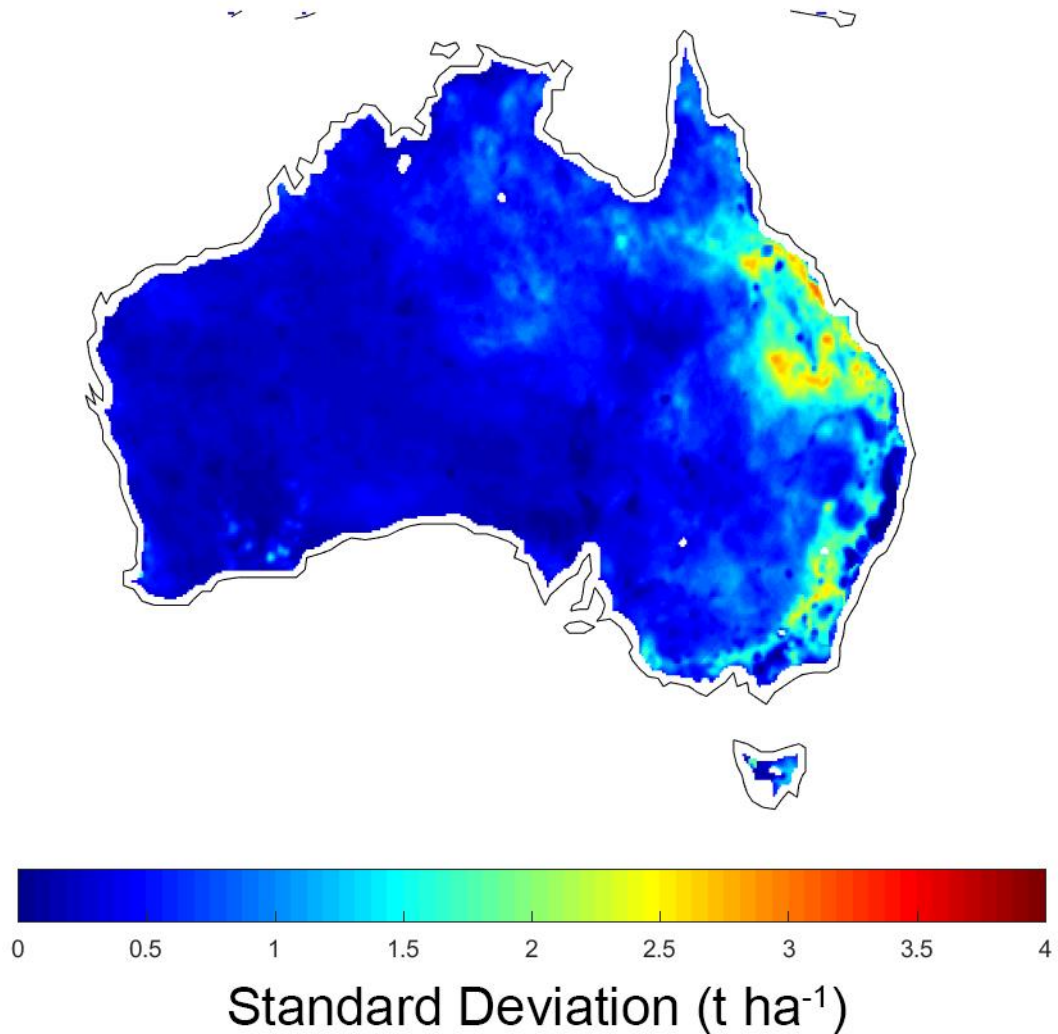


Figure 4.4 Temporal standard deviation of estimated fuel load map from 2003 to 2011.

4.4.2 Comparison with Vegetation Structure Data

Since there was no independent bioregion fuel load data for evaluating the fuel load prediction model, I assessed the AGBC used in calibrating the fuel load model with the vegetation structure dataset (Lucas et al., 2014). Since the vegetation structure dataset is basically a classification of how dense the vegetation is (based on total plant coverage and 95th percentile height), I made a simple assumption that the amount of AGBC is proportional to the density (plant coverage and height) of the vegetations. Originally, the vegetation structure dataset was 30 m gridded snapshot of Australia during the year 2009, but I rescaled it to 0.1°, matching the resolution of estimated AGBC data (and VOD). Each pixel on the vegetation structure map is labelled as a structure formation,

as shown in Figure 4.5. Corresponding detailed description of each structure formation (total plant cover fraction and 95th percentile height) is as listed in Table 4.1.

For all 29 usable bioregions, only four dominant structure formations were presented, which were low scatter trees (14 bioregions), medium scatter trees (5 bioregions), tall open forest (1 bioregion), and very tall closed forest (7 bioregions). The remaining two bioregions had “no data” structure as a dominant formation and thus were removed from the vegetation structure analysis. A comparison between 27 bioregions AGBC and corresponding dominant vegetation structure formations was made, where region with high AGBC was expected to be associated with high density structure formation that has high plant cover fraction such as very tall closed forest, and vice versa. From this comparison, I found a significant relationship with an r^2 of 0.82 and RMSE of 0.57 t ha^{-1} . The results showed that Australia wide AGBC estimates from VOD can roughly explain the vegetation structure (the higher the AGBC is, the denser the vegetation cover is). This also implied that fuel load estimates from AGBC corresponds with the vegetation structure, and thus, was predicting a sensible amount of fuel load across Australia (the higher the fuel load is, the taller and denser the vegetation cover is).

Comparing between the fuel load map shown in Figure 4.2 (panel c and d) and the vegetation structure map in Figure 4.5, it can be seen that the dominant vegetation structures around South Australia areas are a combination of low scattered trees and low woodland that correspond well with the fuel load patterns. Victoria generally has denser forest along the coast (Tall Open and Closed Forest), which is also reflected in Figure 4.2 (panel c and d) as high (over 16 t ha^{-1}) fuel load. Southern part of Western Australia also shows a similar trend where the areas with dense forest are associated with higher fuel load. Fuel load patterns in Tasmania are potentially the least representative of how dense the forests in the area are, due to Tasmania’s smaller area that is surrounded by water (which negatively impacted VOD performance). Overall, the fuel load maps in Figure 4.2 reflected the vegetation structure patterns in Figure 4.5 well.

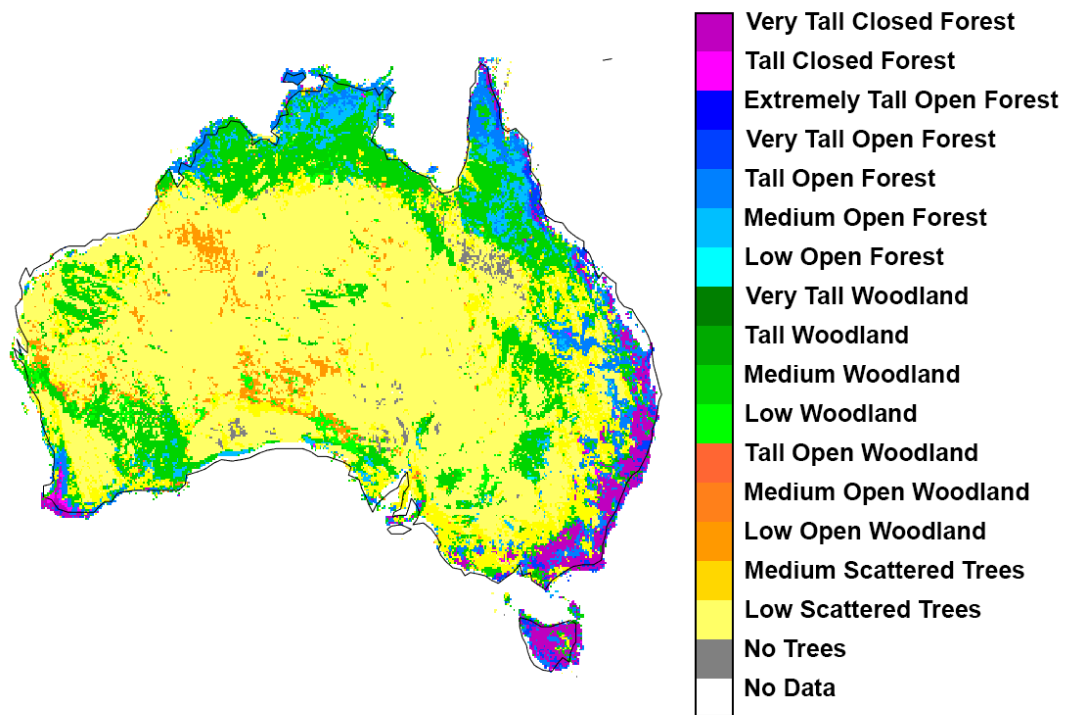


Figure 4.5 Vegetation structure map (rescaled to 0.1°) across Australia (Lucas et al., 2014).

4.5 Limitations

It should be noted that the estimated fuel load produced here does not and is not intended to capture fine scale fuel variations nor discriminate between litter, herbaceous, and woody fuels. It provides an aggregate estimate of the fuel status as seen from the satellite. In addition, the calibration of the fuel load model (Equation 4.5) is performed with observation data only from the south eastern Australian Bioregions and no data tropical regions are available. However, the overall fuel dynamics over Australia is still well captured as demonstrated in the evaluation with vegetation structure dataset, as stated in Section 4.4.2 (with a significant relationship to the vegetation structure, where $r^2 = 0.82$ and $RMSE = 0.57 \text{ t ha}^{-1}$).

Table 4.1 List of vegetation structural formations (as shown in Figure 4.5) and their corresponding total vegetation cover fraction and 95th percentile height.

Vegetation Structural Formation	Total Plant Cover Fraction (%)	95th Percentile Height (m)
No Data	N/A	N/A
No trees	0%	N/A
Low scattered trees	0% to 6%	< 9 m
Medium scattered trees	0% to 6%	9 m to 17 m
Low open woodland	6% to 11%	< 9 m
Medium open woodland	6% to 11%	9 m to 17 m
Tall open woodland	6% to 11%	17 m to 27 m
Low woodland	11% to 30%	< 9 m
Medium woodland	11% to 30%	9 m to 17 m
Tall woodland	11% to 30%	17 m to 27 m
Very tall woodland	11% to 30%	27 m to 57 m
Low open forest	30% to 70%	< 9 m
Medium open forest	30% to 70%	9 m to 17 m
Tall open forest	30% to 70%	17 m to 27 m
Very tall open forest	30% to 70%	27 m to 57 m
Extremely tall open forest	30% to 70%	> 57 m
Tall closed forest	> 70%	17 m to 27 m
Very tall closed forest	> 70%	27 m to 57 m

PART II: FIRE SPREAD MODELLING

5 Modelled Grassland Fire Spread Behaviour due to DOC Variations

In this chapter, I examine the changes in the rate of grassland fire spread due to spatial variations in DOC. Research questions being addressed include: How are DOC variations translated into fire spread variations by models? How do models differ in their fire spread response to DOC variation?

Two Australian fire spread models, Phoenix and Spark, are used to predict both idealised and realistic (based on past fire events) fire spreads. To test the changes in the rate of spread prediction from Phoenix and Spark, I use artificial DOC patterns in idealised scenarios and satellite based DOC dataset, developed in Chapter 3, in realistic scenarios. Fire spread results from both Phoenix and Spark are then compared and the differences between the predictions are discussed.

In previous studies, Phoenix was mostly used for forest fire behaviour prediction (Collins et al., 2015; Louis and Matthews, 2015; Penman et al., 2013; Pugnet et al., 2013). These past studies did not test the variability in fire spread prediction due to variation in DOC, understandably due to their focus on forest fires. Recent fire spread simulation report compared both Phoenix and Spark in various case studies and found both model to performed at median range in grassland fire (Deslandes and Jacobs, 2017).

Since Phoenix and Spark utilised different curing factor as discussed earlier (see Equation 2.2 and 2.3), the predicted grassland fire rate of spreads is expected to be different between the two models especially at low DOC levels. Phoenix's curing factor (Cheney et al., 1998) dictates that fire is struggling to spread when DOC is at 50% or lower, while this threshold is much lower in Spark's curing factor (Cruz et al., 2015) that is DOC at 20% or lower. If the rate of spread is solely based on the curing factor, Spark is expected to predict a much faster rate of spread at low DOC level, while the differences in the predicted rate of spread will approach zero as the DOC level reaches 100%.

5.1 Experiment Setups

The spatial and temporal domains were set to be the same for every test. Fires are ignited within a 100 x 200 km gridded, rectangular domain with a spatial resolution of 200 m. Simulation time is set to 10 hours, with the temporal interval dynamically determined by both models. Temporal intervals in Phoenix and Spark can be as long as 6 minutes. Since we are exclusively interested in the effect of grassland curing, we assume a homogeneous, undisturbed grassland fuel bed as a fuel layer input for all experiments. Both Phoenix and Spark model descriptions and initial configurations are as stated in Chapter 2.2.

5.1.1.1 DOC and Topography Data

The satellite based DOC is calibrated and evaluated with DOC field data collected from a past study of field based curing assessment in Australia and New Zealand (Anderson et al., 2011), as discussed in Chapter 3. Figure 5.1 shows the DOC patterns used in both the idealised (artificial pattern as shown in a, b, and c) and realistic (satellite based DOC pattern as shown in d, e, and f) grass fire spread simulations at Toodyay, WA, Pulletop, NSW, and Jail Break Inn, NSW, along with experimental domain and fire ignition locations.

DEM data is acquired from Geoscience Australia via ELVIS service (Geoscience Australia, 2016). The gridded DEM is available at 25 m spatial resolution.

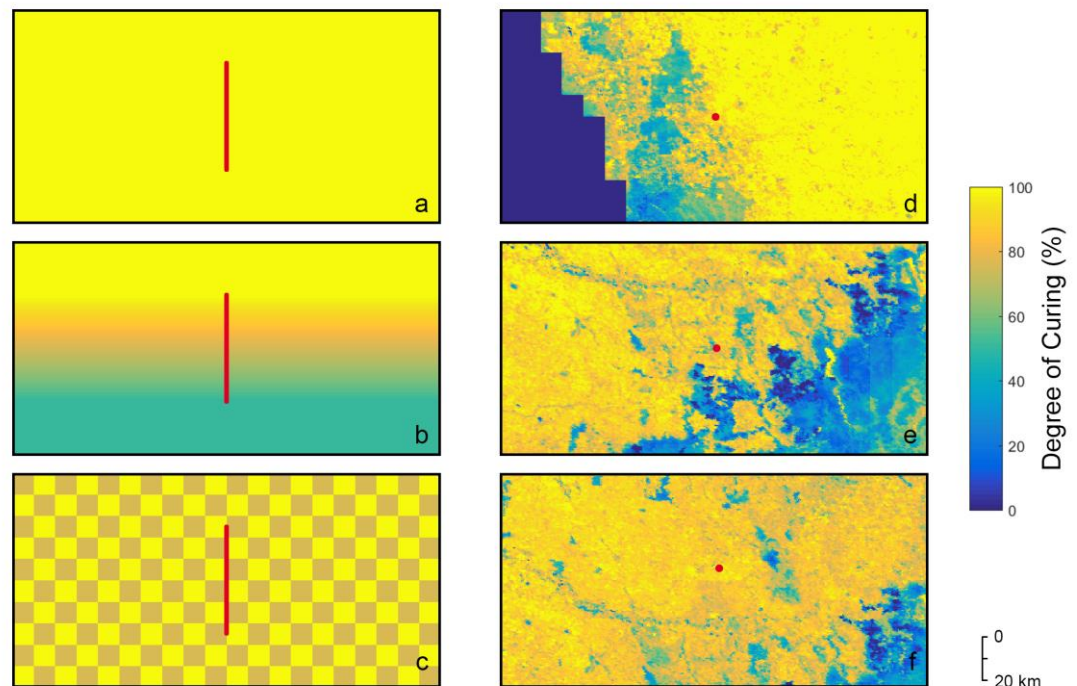


Figure 5.1 DOC spatial maps for a) idealised experiment scenario I1a (only I1 with DOC = 100% is shown here), I4, and I5, b) idealised experiment scenario I2, c) idealised experiment scenario I3, d) realistic experiment scenario R1 (Toodyay, WA), e) realistic experiment scenario R2 (Pulletop, NSW), and f) realistic experiment scenario R3 (Jail Break Inn, NSW). Black borders indicate the 100 x 200 km experiment domain. Red dots or lines indicate the fire ignition location for each experiment.

5.1.2 Idealised Experiments

For idealistic fire spread simulations, we setup 4 different DOC patterns and terrain on a homogeneous grassland fuel bed as follows:

- homogeneous DOC at 100%, 90%, 80%, 70%, 60%, 50%, and 40% on flat terrain (scenario I1)
- DOC gradient from 100 to 50% in southward direction on flat terrain (scenario I2)
- 10 x 10 km checkerboard pattern, alternating between 75% and 100% curing on flat terrain (scenario I3)
- homogeneous DOC at 100% on a 1°, 5°, and 10° slope for downhill direction (scenario I4)
- homogeneous DOC at 100% on a 1°, 5°, and 10° slope for uphill direction (scenario I5)

Note that the different levels of homogeneous DOC in scenario I1 are distinguished with suffix a to g for DOC at 100% to 40% (i.e. scenario I1a has homogeneous DOC at 100%, scenario I1b has homogeneous DOC at 90%, and so on); different slopes for both down and uphill in scenario I4 and I5 are distinguished with suffix a to c for slope at 1° (I4a and I5a), 5° (I4b and I5b), and 10° (I4c and I5c), respectively. Note that the changes in rate of spread due to variation in surface slope can be described as in Equation 5.1 (Noble et al., 1980).

$$R_{\eta} = R e^{0.069\eta} \quad (5.1)$$

where R is the rate of spread on flat terrain (km h^{-1}), η is the slope of ground surface ($^{\circ}$), and R_{η} is the rate of spread on ground of slope η .

Fire ignitions for these idealised experiments are all along a 50 km long north-south line in the middle of the rectangular domain. All points on the line are ignited simultaneously.

Weather conditions for idealised experiments are as listed in Table 5.1. Note that cloud cover is a percentage fraction of cloud in the sky during the fire event, where 0% cloud cover indicates a clear sky. Topography is assumed to be homogeneous flat or uniformly sloping terrain.

5.1.3 Realistic Experiments

For realistic fire spread simulations of past fire events in Australia, several gridded and station datasets are used. These include satellite based gridded DOC, observed weather data from the nearest weather station, gridded topography, and satellite derived burned area data. Three past fire events in Australia are chosen for realistic fire spread experiments. These three past fire events are:

- Toodyay, WA (29/12/2009) (scenario R1)
- Pulletop, NSW (6/2/2006) (scenario R2)
- Jail Break Inn, NSW (1/1/2006) (scenario R3)

These small to large fire events (with Toodyay, WA burned area of $\sim 30 \text{ km}^2$, Pulletop, NSW burned area of $\sim 90 \text{ km}^2$, and Jail Break Inn burned area of $\sim 300 \text{ km}^2$) have mixed fuel types with significant grasslands and little to no forest fuels. For each of the three scenarios, we test 3 different DOC and topography configurations, including a control

scenario with homogeneous 100% DOC pattern and flat terrain (scenario with suffix A), satellite based DOC pattern and flat terrain (scenario with suffix B), and satellite based DOC pattern and terrain data from a 25 m DEM (scenario with suffix C). For instance, scenario R1A is a control scenario with homogeneous 100% DOC pattern for the Toodyay fire. Ignition location is set at the centre of the rectangular domain, based on the actual burned area and observed wind direction.

Weather conditions for realistic fire spread experiments, including temperature, relative humidity, wind speed, and wind direction, are obtained from the past development of historical fire weather dataset (Lucas, 2010). Extracted weather information is as listed in Table 5.2. The location of past fire events and their associated nearest fire weather stations are shown in Table 5.3. The weather records are daily, ranging from 1973 to 2010 with over 300 observation sites across Australia. Note that observed cloud cover data is not available, thus, cloud cover is always assumed to be 0% (clear sky) for both idealised and realistic experiments.

The fire rate of spread and area burned from the Phoenix and Spark models are compared across the different experiments.

Table 5.1 List of weather inputs for idealised fire spread experiment.

Wind Direction	Wind Speed (km h⁻¹)	Temperature (°C)	Relative Humidity (%)	Cloud Cover (%)
East	55	40	5	0

Table 5.2 Observed weather conditions from the nearest weather station for realistic fire spread experiments.

Location	Event Date	Wind Direction	Wind Speed (km h⁻¹)	Temperature (°C)	Relative Humidity (%)	Cloud Cover (%)
Toodyay, WA	29/12/2009	Northwest	16.6	42.7	20.0	0
Pulletop, NSW	6/2/2006	West Southwest	31.3	35.5	12.0	0
Jail Break Inn, NSW	1/1/2006	Northwest	50.0	44.6	8.0	0

Table 5.3 List of chosen fire events for realistic fire spread experiments with corresponding nearest weather stations.

Fire Event			Nearest Weather Station	
Site Name	Event Date	Coordinate	Site Name	Coordinate
Toodyay, WA	29/12/2009	31.55° S, 116.46° E	Perthap, WA	31.93° S, 115.98° E
Pulletop, NSW	6/2/2006	35.40° S, 147.72° E	Wagga Wagga, NSW	35.16° S, 147.46° E
Jail Break Inn, NSW	1/1/2006	34.92° S, 147.66° E	Wagga Wagga, NSW	35.16° S, 147.46° E

5.2 Grassland Fire Spread with Variable DOC Results

5.2.1 Idealised Experiments

For each idealised experiment, we examine the average fire spread speed, area burned, and flame height, as shown in Table 5.4. Note that Spark does not compute flame height, thus only rate of spread and area burned are shown. The corresponding scatter plot showing the changes in rate of spread due to changes in DOC with computed rate of spread from Cheney et al., 1998 and Cruz et al. 2015 curing coefficients are shown in Figure 5.2. Corresponding burned time step and flame height map for each scenario are shown in Figure 5.3 (I1a, I4b, and I5b are only shown for I1, I4, and I5). For area burned listed in Table 5.4, we use the total area that was burned after 5 hours, since the fire front in some experiments reached the border of the experiment domain well before the end of the experiment (10 hours).

For scenario I4 and I5, the slight changes in terrain elevation can affect the fire severity, where uphill slope increases the fire severity (increase in spread speed and area burned) and vice versa. Note that the steeper the uphill slope is, the faster the rate of spread (McArthur, 1967). As the slope becomes steeper for both down and uphill (scenario I4a to I4c for downhill and I5a to I5c for uphill), the rate of spread decreases significantly for downhill (I4) and increases significantly for uphill (I5), as expected (Noble et al., 1980).

Changes in DOC pattern (scenario I2 and I3) significantly impede the fire severity. With 50% changes in DOC from north to south of the experiment domain (100% to 50%), the

fire front is significantly slowed down, as shown in Figure 5.3 for scenario I2 in both Phoenix and Spark. In scenario I3, where an abrupt change in DOC with a checkboard pattern alternating between 75% and 100% curing occurred, the rate of spread and advancement in fire front is slightly hindered. Note that Phoenix's head fire is significantly impeded by alternating DOC pattern, whereas Spark's head fire is not as strongly affected as Phoenix. Both fires in scenario I2 and I3 have variable average spread speed across different east to west transects due to changes in the DOC in the domain.

Area burned directly corresponds to the rate of spread, i.e. the faster the fire spread, the more area burned. However, Spark's area burned at the end of simulation (10 hours) are much larger than Phoenix due to larger flanking and backing fire spread. Though area burned from both Phoenix and Spark at 5 hours mark in scenario I1a is more comparable, it has a different shape. Note that the average flame heights in Phoenix vary little between each scenario, because the grassland fire flame height is limited due to fuel bed structure and height. However, the faster the fire spread, the higher the flame height (Cheney and Sullivan, 2008).

Table 5.4 Average fire spread speed, area burned, and average flame height for idealised experiments.

Scenario	Degree of Curing Configuration	Terrain Configuration	Spark		Phoenix		
			Average Fire Spread Speed (km h ⁻¹)	Area Burned (km ²) after 5 hours	Average Fire Spread Speed (km h ⁻¹)	Area Burned (km ²) after 5 hours	Average Flame Height (m) after 5 hours
I1a	Homogeneous (100%)	Flat	17.49	4,754.40	17.64	4,769.36	2.40
I1b	Homogeneous (90%)	Flat	16.52	4,501.52	13.97	3,712.64	2.25
I1c	Homogeneous (80%)	Flat	14.34	3,937.48	8.12	2,106.68	1.91
I1d	Homogeneous (70%)	Flat	10.69	2,942.24	3.33	844.00	1.45
I1e	Homogeneous (60%)	Flat	6.28	1,756.84	1.11	282.08	1.03
I1f	Homogeneous (50%)	Flat	3.00	854.28	0.35	90.52	0.71
I1g	Homogeneous (40%)	Flat	1.29	377.44	0.12	30.04	0.48
I2	Gradient Curing (100% to 50%)	Flat	2.18 to 12.11	2,878.80	0.30 to 18.44	2,159.64	2.23
I3	Checkerboard Pattern (75% and 100%)	Flat	8.98 to 13.36	3,905.00	7.88 to 15.28	2,418.48	2.01
I4a	Homogeneous (100%)	1° Downhill	16.45	4,568.40	16.37	4,421.44	2.37
I4b	Homogeneous (100%)	5° Downhill	13.38	4,000.84	12.03	3,249.60	2.16
I4c	Homogeneous (100%)	10° Downhill	11.49	3,611.68	7.70	2,068.96	1.88
I5a	Homogeneous (100%)	1° Uphill	18.33	4,929.52	18.88	5,104.32	2.48
I5b	Homogeneous (100%)	5° Uphill	22.37	5,485.12	24.87	5,439.76	2.72
I5c	Homogeneous (100%)	10° Uphill	27.47	6,044.92	34.65	5,426.36	3.03

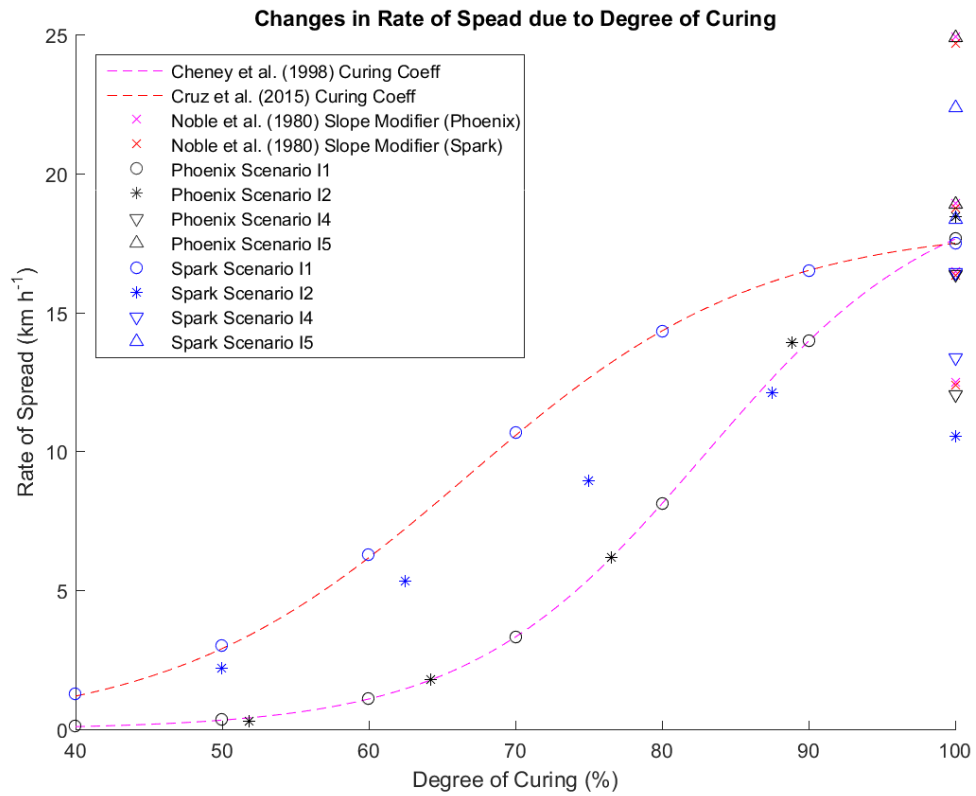


Figure 5.2 Scatter plot showing the changes in the rate of spread due to changes in DOC from idealised experiments I1a to I1g, I2, I4a to I4b, and I5a to I5b for both Phoenix and Spark models. Calculated rate of spread from Cheney et al. (1998) and Cruz et al. (2015) are shown as dash lines. Predicted rate of spread with slope modifier from Noble et al. (1980) are shown as crosses.

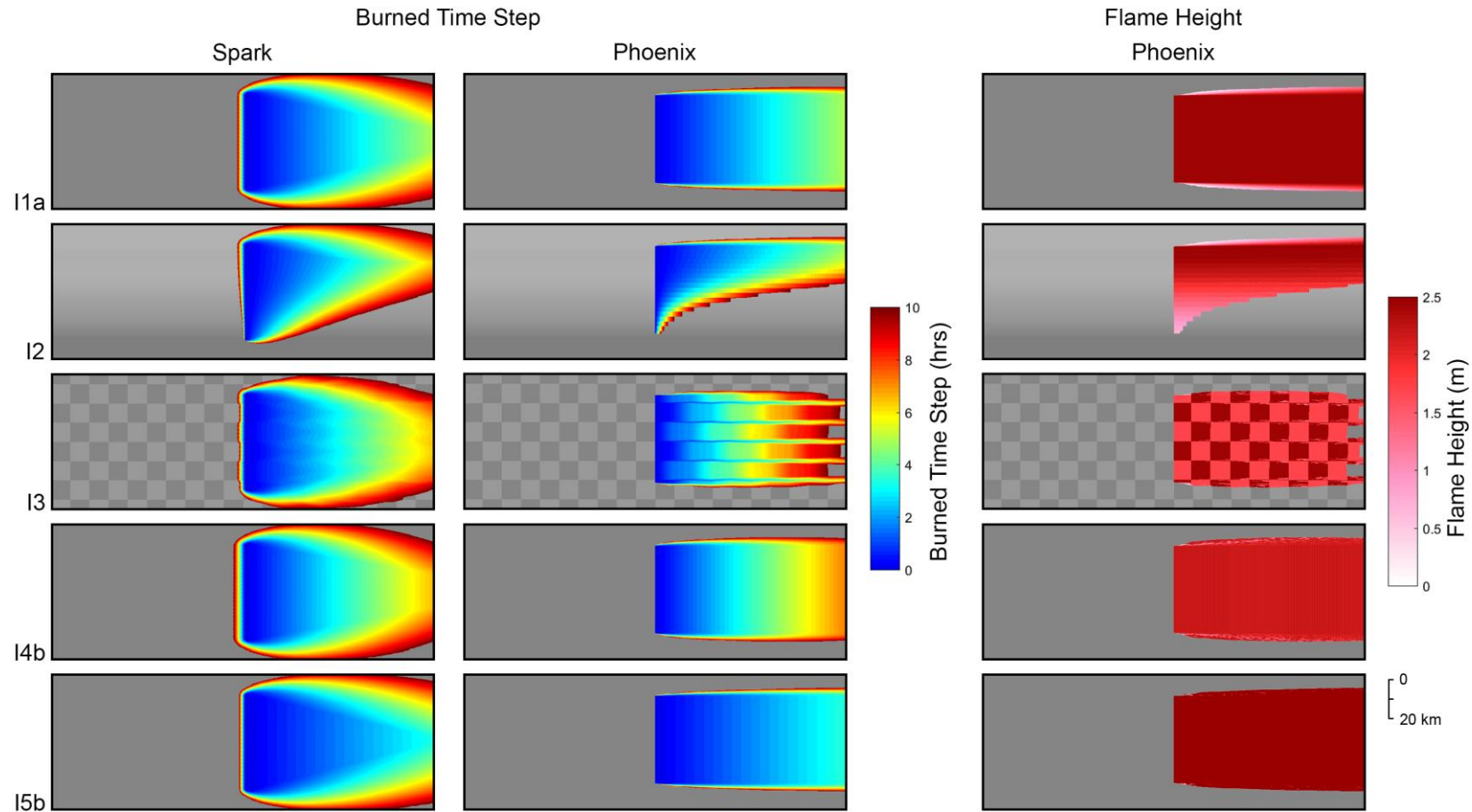


Figure 5.3 Burned time step (2 left columns for Spark and Phoenix) and flame height (right column for Phoenix) over the burned area in the idealised experiments (only I1a, I4b, and I5b are shown for scenario I1, I4, and I5), where the background shows the corresponding DOC spatial map in greyscale (as shown in Figure 5.1).

5.2.2 Realistic Experiments

For realistic experiments, we also observe the same output parameters with an emphasis on the rate of fire spread. Table 5.5 summarises the average rate of fire spread, area burned, and average flame height for 3 realistic scenarios, each with 3 different DOC and terrain configuration combinations. Corresponding weather information for each location is as listed in Table 5.2. Every scenario uses the same location-specific weather conditions regardless of DOC and terrain configuration combinations.

Comparing the fire severity between control scenarios (DOC = 100%) and scenarios with satellite based DOC and 25 m DEM included, the magnitude of both spread speed and area burned are quite different. Control scenarios have faster fire spread and larger burned area for both Phoenix and Spark. The difference between scenarios with flat and realistic elevation is, however, not very large, similar to the idealised experiments at 1° slope. This is due to the maximum slopes in each burned domain being 1.00°, 1.98°, and 0.21° for experiment R1-C, R2-C, and R3-C, respectively. Note that the estimated slope loses its accuracy when the DEM resolution is low (Chang and Tsai, 1991; Zhang et al., 1999).

Differences in rate of fire spread between each DOC and terrain configuration combination at each time step for a 10 hour fire are shown in Figure 5.4. Similar to the average speed, the rate of fire spread at each time step for control scenarios with DOC = 100% are the highest, while the fire spread speed for satellite based DOC and flat or realistic elevation combinations are similar. These apply for all 3 fire event locations. The sudden stop of fire spread after ~4 to ~5 hours for DOC = 100% in scenario R3 is because the fire front reaches the border of the experiment domain before the end of 10 hours experiment period. See Figure 5.5 for visual comparisons between area burned, burned location at each time step, and flame height for each scenario (scenarios with DEM are not shown).

Note that differences in average flame height between each scenario are small, similar to the idealised experiments. Again, flame height does seem to be higher as the fire spreads faster (Cheney and Sullivan, 2008)

Table 5.5 Average fire spread speed, area burned, and average flame height for realistic experiments.

Scenario	Location	Degree of Curing Configuration	Terrain Configuration	Spark		Phoenix		
				Average Fire Spread Speed (km h ⁻¹)	Area Burned (km ²) after 5 hours	Average Fire Spread Speed (km h ⁻¹)	Area Burned (km ²) after 5 hours	Average Flame Height (m) after 5 hours
R1-A (Control)	Toodyay, WA	Homogeneous (100 %)	Flat	3.31	55.60	4.95	87.12	1.24
R1-B	Toodyay, WA	Satellite based DOC	Flat	2.19	43.76	1.08	14.64	1.19
R1-C	Toodyay, WA	Satellite based DOC	DEM (Max slope = 1.00°)	2.18	42.44	1.08	18.48	1.21
R2-A (Control)	Pulletop, NSW	Homogeneous (100 %)	Flat	5.42	133.84	8.57	141.40	1.63
R2-B	Pulletop, NSW	Satellite based DOC	Flat	2.99	20.72	0.22	0.76	0.60
R2-C	Pulletop, NSW	Satellite based DOC	DEM (Max slope = 1.98°)	3.03	20.80	0.20	0.76	0.63
R3-A (Control)	Jail Break Inn, NSW	Homogeneous (100 %)	Flat	11.35	554.72	16.00	288.00	1.72
R3-B	Jail Break Inn, NSW	Satellite based DOC	Flat	10.24	466.12	11.64	161.84	2.16
R3-C	Jail Break Inn, NSW	Satellite based DOC	DEM (Max slope = 0.21°)	9.48	458.68	11.58	163.76	2.17

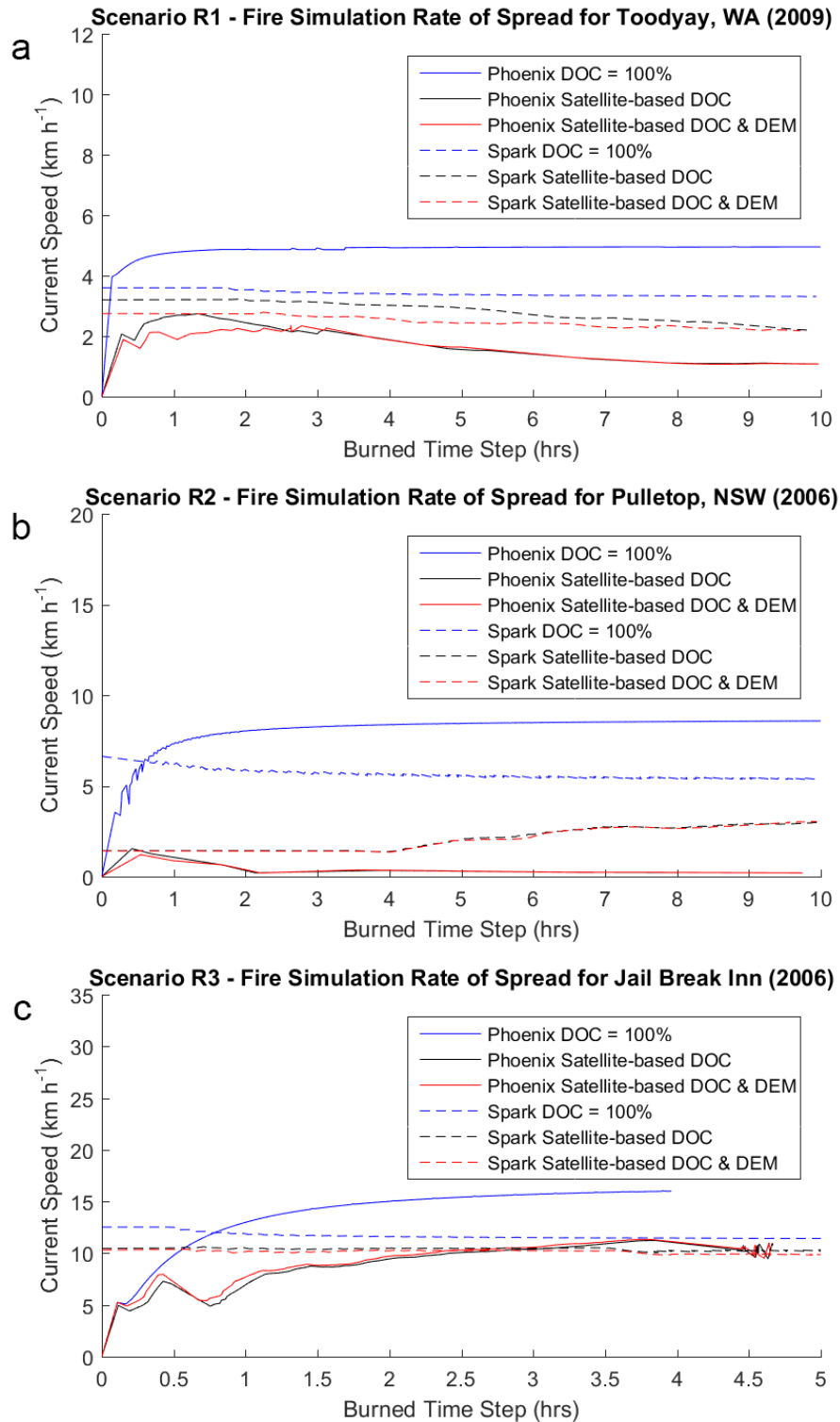


Figure 5.4 Fire propagation speed at each burned time step comparison time series for all realistic experiments (a, b, and c for scenario R1, R2, and R3), where the blue line shows control scenarios with homogeneous DOC = 100%, the black line shows scenarios using satellite based DOC, and the red line shows scenarios using satellite based DOC and digital elevation model. Solid lines are for Phoenix model, whereas dash lines are for Spark models.

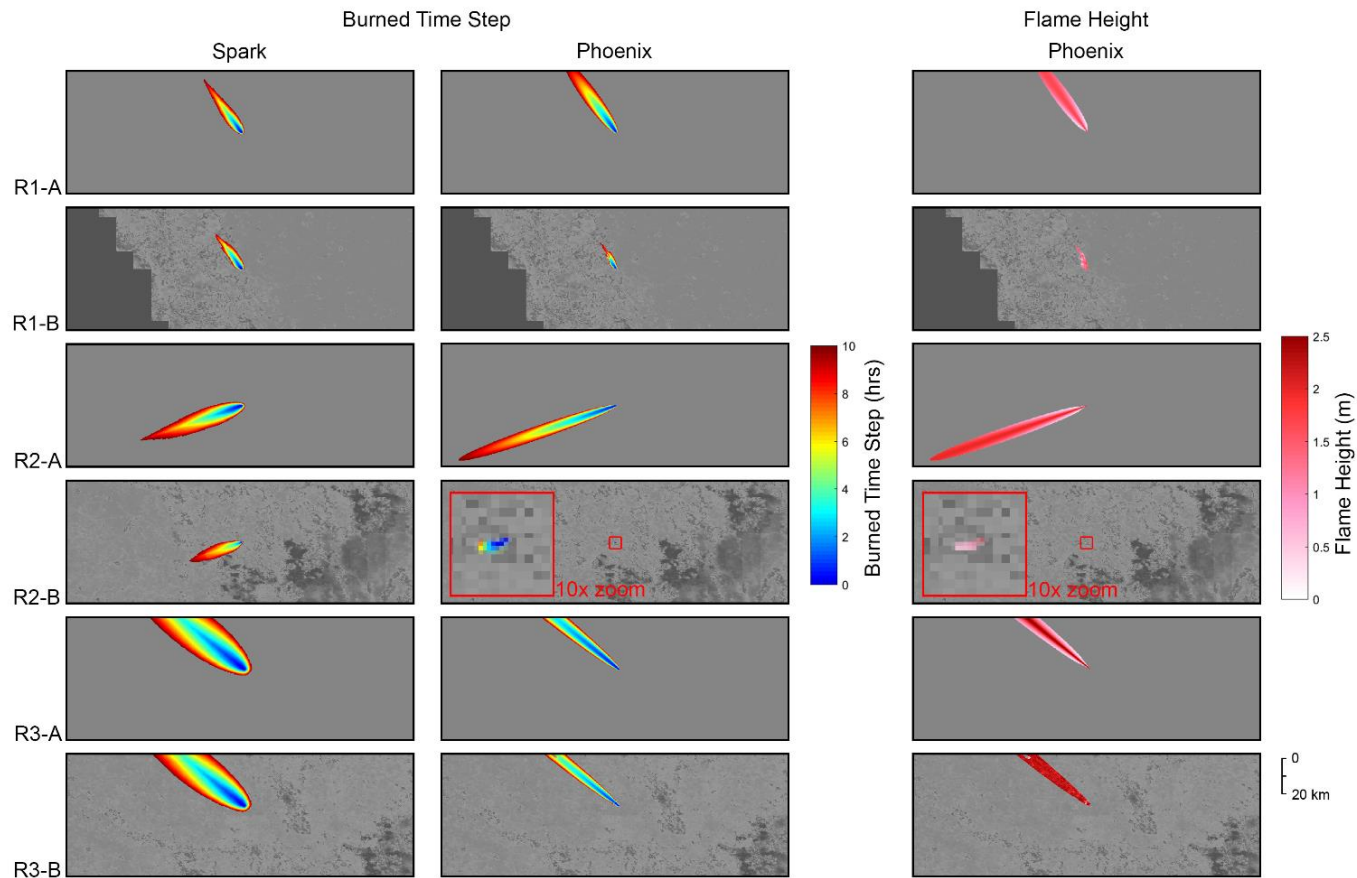


Figure 5.5 Burned time step (2 left columns for Spark and Phoenix) and flame height (right column for Phoenix) area burned maps for realistic experiment, where the background shows the corresponding DOC spatial map in greyscale (as shown in Figure 5.1). The scenarios with digital elevation map (R1-C, R2-C, and R3-C) are not shown here due to negligible changes in spreads. For Phoenix's scenario R2-B, a 10 times magnifying burned area are shown with red bounding box insets.

5.3 Discussion

5.3.1 Grass Fire Spreads in Idealised Condition

During idealised experiments, we found that changes in DOC can significantly affect the fire spread rate and area burned. There is a non-linear reduction in the rate of spread due to changes in DOC as described by Cheney et al. (1998) and Cruz et al. (2015) curing coefficients shown in Figure 5.2. In scenario I1, both Phoenix and Spark predicted rate of spread follows Cheney et al., 1998 (Phoenix) and Cruz et al., 2015 (Spark) curing coefficient closely. In scenario I2, for Phoenix, the fastest front in I2 where DOC is at 100% is interestingly slightly faster than I1a, while at a lower DOC level, I2 (in the area with 50 % DOC) the fire front is slightly slower than I1e. This demonstrates a slightly higher variation in fire spread in a non-homogeneous DOC environment than a homogeneous DOC environment for Phoenix. In contrast, Spark shows severe underestimation of rate of spread when compared with its I1 results and Cruz et al. (2015) curing coefficient. In addition, Spark's highest rate of spread does not occur at the point where DOC is at maximum 100%, but at slightly lower DOC. These are due to the implementation of flanking and backing spread in Spark. The differences in flanking and backing spread implementation in Phoenix and Spark also heavily influence the fire perimeters. Without any flanking and backing spread implementation, Spark's severe underestimation and shift in the location of highest rate of spread do not occur, and the predicted rate of spreads are closer to I1 results. While Phoenix simulations have some degree of lateral spreading and no back spreading at all, Spark simulations have a significantly larger lateral and back spread.

Immediately altering between 2 different DOC level of 75% and 100% with a 10 x 10 km checkerboard pattern in scenario I3 also further obstructs the fire front advancement speed for both models (34.35% and 36.13% slower than I1a on average for Phoenix and Spark). This spread rate is slower than the likely spread rate for a uniform DOC of 87.50%, the average of the DOC levels used in the checkerboard, especially for Spark. It is interesting to note that at the boundary between two rows in the I3 checkerboard pattern the fire is able to spread at a rate much closer to that in I1a (only 13.38% slower) for Phoenix. It does this by spreading perpendicular to the fire just enough to light the 100% DOC square at each intersection. This small lateral spread is a consequence of Phoenix's use of an elliptic stencil when calculating fire propagation. In general, however, this may suggest that Phoenix allows little spread perpendicular to the wind direction and

most of the checkerboard squares are unaffected by these rapidly spreading fire tendrils. However, this behaviour suggests that in realistic DOC landscapes, where complex patterns of varying levels of DOC exist, the actual fire spread rate may be difficult to estimate and is unlikely to resemble the fire spread rate over an area with an “average” DOC level. These fire tendrils are much less prominent in the Spark simulation, due to its wider lateral spread and higher spread speed at 75% DOC. At 5 hours of simulation time with no fire suppression and any disruption in the terrain, the burned area for I2 and I3 scenarios are still relatively large, but much smaller than I1a (54.72% and 49.29% for Phoenix and 39.45% and 17.87% for Spark which has a smaller area burned for I2 vs I1a and I3 vs I1a, respectively). This suggests that DOC plays an important role in determining the magnitude of grassland fire spread under extreme weather conditions with no fire suppression. Note that at the end of 10 hours simulation, Spark’s area burned are larger than Phoenix. From Figure 5.3, it can be seen that while Spark’s head fires are getting smaller as the simulation time approaches the end, which differs from Phoenix’s constant head fire size, the flank and back fires are much larger in Spark.

5.3.2 Modelled Grass Fire Spreads from Past Events

For more realistic experiments, we see considerable spatial variability in DOC in the satellite based observations. These DOC variations substantially affect the magnitude of grassland fire spread during all 3 past fire events. Assigning control scenarios with DOC = 100%, the differences in fire rate of spread and area burned between control scenarios and scenarios with satellite based DOC are very large. We found 78.18%, 98.60%, and 27.25 % reduction in spread speed for Phoenix (compared to 100% DOC) and 33.84%, 44.83%, and 9.78% for Spark in scenario R1-B when compared with R1-A, scenario R2-B when compared with R2-A, and scenario R3-B when compared with R3-A, respectively. Spark clearly suffered significantly less rate of spread reduction due to more generous curing coefficient for all cases.

Scenario R3 is characterised by more severe fire weather conditions than R1 and R2, and the smallest rate of spread and area burned reduction difference from DOC = 100% control scenario for both Phoenix and Spark, because the fire front (determined by wind direction) advances through an area with consistently high DOC (~85 to 95%). In scenario R1 and R2 the fire encounters areas with lower DOC, as seen in Figure 5.5, which heavily impedes the advancement of the fire, especially in Phoenix cases. In scenario R1, the initial area that the fire ignited and burned before the rate of spread

begins to drop has DOC of ~75 to 85%. The surrounding DOC tiles after ~6 hour mark have a relatively low DOC between ~50 to 60%, thus it became more difficult for the fire to spread for Phoenix. Spark's fire can spread further than Phoenix, even with smaller spread in control scenario prediction due to its curing coefficient, as shown in Figure 5.4a. For scenario R2, we have a consistently lower DOC from the ignition (~45 to 55%), resulting in a very slow rate of spread for scenario R2 and very small final area burned after 10 hours for Phoenix, but a much larger spread and area burned in Spark. This is again, due to different curing coefficients in Phoenix and Spark, where Phoenix's curing coefficient is much lower than Spark's (0.019 vs 0.166 at DOC = 50% for Phoenix and Spark curing coefficient; computed with Equation 2.2 and 2.3) (Cheney et al., 1998; Cruz et al., 2015). For scenario R3, at the northwest of the burned area, there is a small area where the fire rate of spread is severely reduced to the point that it is not burned after 10 hours for Phoenix, while this is not the case for Spark. This area has a DOC level of ~38%, thus, the curing coefficient for Phoenix and Spark are 0.004 and 0.057. We also redid all realistic experiments using the same severe weather setting as the idealised runs, and found the rate of spread is still strongly affected by DOC.

In terms of influence on fire spread due to changes in terrain, both idealised and realistic experiments suggested that the effect of terrain at around 1° slope on fire spread rate is small, with a change by a factor of 1.07 per Equation 5.1 (Noble et al., 1980). On more extreme terrain elevation changes, such as a 10° slope in I4c and I5c, the changes in the rate of spread are much more significant with a factor of 1.99 for uphill and 0.50 for downhill slope. For Phoenix, the uphill slope increases the rate of spread by 17.01 km h⁻¹ (factor of 1.96), while rate of spread decline due to downhill slope is 9.94 km h⁻¹ (factor of 0.44). For Spark, the rate of spread is increased by 9.98 km h⁻¹ (factor of 1.57) and decrease by 5.99 km h⁻¹ (factor of 0.66). Spark uses Kataburn framework to calculate slope effects (Sullivan et al., 2014), while Phoenix uses standard slope factor developed by McArthur (1967). Spark has less reduction in spread speed in a downhill slope because Kataburn framework reduces the underprediction in downhill rate of spread from earlier slope modifier models. Other variations in speed differences in both up and downhill slope are due to lateral and backing spread implementations. In terms of flame height, we can see slight differences in flame height due to differences in terrain elevation in the realistic cases, or rather, elevation patterns on the flame height distribution. It is not clear how Phoenix incorporates elevation variations with small changes in flame height though. The area burned differences are also small on a 1° slope, while quite significant on a 10° slope for both models.

The impact of DOC on flame height is arguably more uncertain, since flame height is consistently low in grassland fires. Scenario R3 also shows that the average flame height from fire with DOC = 100% is lower than flame height from fire with satellite based DOC from Table 5.5. This is due to the flame height along the outer edge of the burned area on a homogeneous DOC (100%) field is much lower than the flame height along the edge of same fire on a variable, satellite based DOC field (Figure 5.5, scenario R3-A and R3-B), thus lowering the overall mean flame height. It appears to be due to how the flank and back fires are handled in Phoenix. Though there is a relationship that can be clearly seen in experiment I3, it should be noted that the flame height and DOC relationship is only applicable at the head fire (Cheney and Sullivan, 2008). This is consistent with Cheney and Sullivan (2008) who suggested that DOC and flame height have a positive relationship (the higher the DOC is, the higher the flame height is).

It should be noted that the area burned simulated from the realistic scenarios differs from the actual area burned during the fire events, with simulated area burned of 14.64 km², 0.76 km², and 161.84 km² for Phoenix and 43.76 km², 20.72 km², and 466.12 km² for Spark and actual area burned of ~30 km², ~90 km², and ~300 km² for Toodyay, WA (R1), Pulletop, NSW (R2), and Jail Break Inn, NSW (R3), respectively. This is not unexpected, because there are major assumptions made in our realistic fire spread simulations, including homogeneous grassland fuel bed, single wind direction, exclusion of fire suppressions and disruptions, and the burned duration. The simulations are setup this way, since we aim to make a clear evaluation of the effects of DOC on fire spread in case of a grassland fire within the Phoenix and Spark models, rather than recreate the past fire events with precision

Different curing coefficient and flank and back fire implementations heavily influenced the predicted results.

5.3.3 Model Uncertainties

In addition to variabilities in fire spread prediction due to various assumptions I made during the realistic experiments, due to lack of climatological inputs with sub-daily (i.e. hourly) timestep, and better understanding of the evolution of past events, there are uncertainties that can be introduced due to the way the model is configured (i.e. implementing flank and back fire in Spark affects the fire spread prediction) and from the

model itself (i.e. both rate of spread prediction from Cheney et al. (1998) and Cruz et al. (2015) assume no disruption along the fire's path). While both Phoenix and Spark both tried to incorporate as many features as possible (e.g. disruption and road proximity), in reality, there is very likely to be a higher degree of variability in both the weather and fuel measurements. Cheney et al. (1998) recommended fire suppression agencies to plan their logistics on the basis that there are 15% chance that the fire spreads are going to exceed the predicted spread.

6 Grasslands Fire Spread Behaviour due to Fuel Load Variations

In this chapter, I examine the changes in the rate of grassland fire spread due to spatial variation in fuel load. Research questions of interest include: How are fuel load variations translated into fire spread variations by models? How do models differ in their fire spread response to fuel load variation? How much of this variation is due to model structure and configuration aspects rather than the head fire rate of spread algorithm used?

As in Chapter 5, I use Phoenix and Spark to predict both idealised and realistic (based on past fire events) fire spread. Artificial fuel load patterns and satellite based fuel load spatial maps developed in Chapter 4 are used in idealised and realistic experiments. Fire spread results from both Phoenix and Spark are then compared and the differences between the prediction from both models are discussed. The contents in this chapter is from the paper “Effect of Fuel Load on Grassland Fire Spread within the Phoenix RapidFire and Spark Fire Spread Models” (in review).

Since most of the past studies that used Phoenix are focused on forest fire behaviour, the fuel classes used in fire spread predictions have both surface and elevated fuel (Penman et al., 2013; Pugnet et al., 2013). Phoenix will only engage its grassland fire spread model when only surface fuel is present (elevated fuel is zero). For studies that, in addition to forest fuels, also involved grassland or pasture fuel loads, where only surface fuel is present, the fuel load levels are usually lower than 6 t ha^{-1} , thus not engaging the spread reduction factor in Phoenix grassland fire spread (Collins et al., 2015; Louis and Matthews, 2015). However, there is a study on how revegetation alters fire intensity that set pasture fuel load at 7 t ha^{-1} in one of the three revegetation test scenarios (the revegetation scenarios are: low pasture fuel at 2 t ha^{-1} , moderate pasture fuel at 4.5 t ha^{-1} , and high pasture fuel at 7 t ha^{-1}) (Collins et al., 2015). They found that at low pasture fuel, increasing the coverage of higher biomass native woody vegetation will increase fire size and intensity, while at both moderate and high pasture fuel, the fire intensity will generally reduce instead. The trends discovered also corresponded with patterns observed in South Africa, as stated by Collins et al. (2015) that the evidence from South African savannahs suggested that when the vegetation cover exceeds 40%, the annual area burnt is reduced. Since the high pasture fuel level is only at 7 t ha^{-1} , I suspect that the spread reduction effect from Phoenix is not very prominent, and the fire intensity prediction might not be affected in a similar manner as the fire spread.

It should also be noted that the effect of fuel load on grassland fire spread is debatable. In some past grassland fires, the rate of spread was considered directly proportional to the amount of fuel (Cheney and Sullivan, 2008). In contrast, there were several large fires in a very fine grass with low fuel load ($\sim 2.5 \text{ t ha}^{-1}$) that spread as fast as the fires on coarser and heavier grasses (Cheney et al., 1998). It was later found that fuel load directly affects the grassland fire's rate of spread only if the changes in fuel load also reflect changes in fuel condition, such as fuel continuity (extent of fuel coverage on ground surface). Fuel continuity can be vastly different between pasture types due to the natural distribution of grasses. Fuel load by itself was found to have more influence on flame height and fire intensity (Cheney and Sullivan, 2008). For this study, I assume the changes in fuel load to reflect the change in fuel continuity similarly with CSIRO southern grassland fire spread model.

6.1 Experiment Setups

The experiments for both Phoenix and Spark are conducted in the same domain configurations as in Chapter 5, where fires are ignited within a 100 x 200 km rectangular gridded domain at a spatial resolution of 200 m. The time allows for fire to spread is set to 10 hours without any suppression or obstruction to the fire front.

6.1.1 *Fuel Load, DOC and Topography Data*

The satellite based fuel load used here is as discussed in Chapter 4. Figure 6.1 shows the surface fuel load patterns used in both the idealised (artificial pattern as shown in panels a, b, and c) and realistic (satellite based fuel load pattern as shown in panels d, e, and f) fire spread experiments, along with experimental domain and fire ignition locations.

DOC spatial pattern is also used in some realistic experiments to demonstrate the effect of variable DOC in grassland fire spread. The DOC spatial maps used in realistic experiments are the same as those used in Chapter 5 (see Figure 5.1 panels d, e, and f).

DEM data used here is as described in Chapter 5.

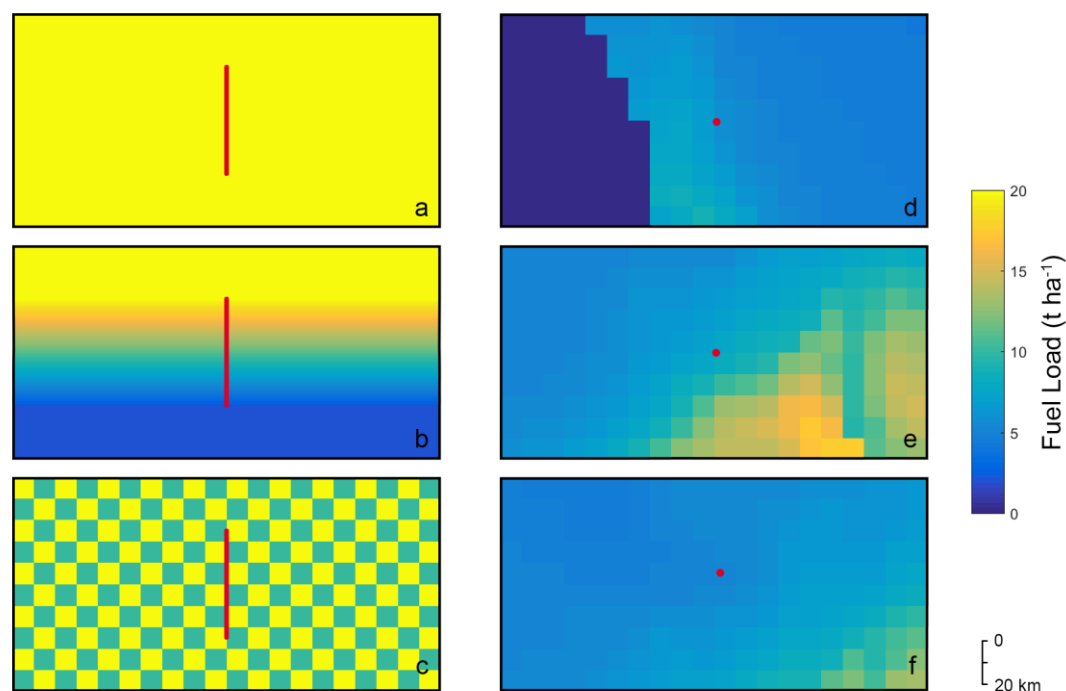


Figure 6.1 Artificial fuel load for idealised experiments (a, b, and c) and satellite based fuel load at Toodyay, WA (d), Pulletop, NSW (e), and Jail Break Inn, NSW (f) for realistic experiments. Red lines and dots indicate the fire ignition locations. Only 20 t ha⁻¹ fuel load is shown for idealised experiment scenarios with homogeneous fuel load.

6.1.2 Idealised Experiments

For idealised grassland fire experiments, we specified 4 different fuel load patterns and terrain combinations on a grassland fuel bed with DOC at 100% as followed:

- homogeneous fuel load at 20, 15, 10, 5, and 2 t ha⁻¹ on a flat terrain (scenario I1)
- fuel load gradient from 20 to 2 t ha⁻¹ in southward direction on a flat terrain (scenario I2)
- 10 x 10 km checkerboard pattern, alternating between 4 and 8 t ha⁻¹ fuel load on flat terrain (scenario I3)
- homogeneous fuel load at 20 t ha⁻¹ on a 1°, 5°, and 10° slope for downhill direction (scenario I4)
- homogeneous fuel load at 20 t ha⁻¹ on a 1°, 5°, and 10° slope for uphill direction (scenario I5)

The different level of homogeneous fuel load in scenario I1 is distinguished with suffix a to e for fuel load at 20 (I1a) to 2 t ha⁻¹ (I1e). For scenario I4 and I5, different slopes for both down and uphill are distinguished with suffix a to c for slope at 1° (I4a and I5a), 5° (I4b and I5b), and 10° (I4c and I5c). In theory, the changes in rate of spread due to different surface slope is as previously described as in Equation 5.1.

The fire is ignited along a 50 km long north-south line in the middle of the testing domain for all idealised experiments. The list of weather data used in idealised experiments can be seen in Table 5.1. Artificial fuel load patterns are as shown in Figure 6.1a (scenario 1 and 4), 6.1b (scenario 2), and 6.1c (scenario 3).

6.1.3 *Realistic Experiments*

We selected three past fire events with various sizes in Australia as references for realistic experiments. Several gridded and weather station datasets are used to emulate the condition of these past events. These three past fire events are:

- Toodyay, WA (29/12/2009) (scenario R1)
- Pulletop, NSW (6/2/2006) (scenario R2)
- Jail Break Inn, NSW (1/1/2006) (scenario R3)

These small to large fire events (with Toodyay, WA burned area of ~30 km², Pulletop, NSW burned area of ~90 km², and Jail Break Inn burned area of ~300 km²) have mixed fuel types with significant grasslands and little to no forest fuels. For each scenario, we run 4 different fuel load and terrain configurations, including a control scenario with homogeneous fuel load of 5.1 t ha⁻¹, homogenous DOC at 100%, and flat terrain (scenario with suffix A), satellite based fuel load with 100% DOC and flat terrain (scenario with suffix B), satellite based fuel load and DOC with flat terrain (scenario with suffix C), and satellite based fuel load and DOC with terrain data from a DEM (scenario with suffix D). For instance, scenario R2-B is a Pulletop fire simulation with satellite based fuel load and 100% DOC on a flat terrain. Note that for scenario with homogeneous fuel load (suffix A), fuel load is set to 5.1 t ha⁻¹ because it is the same amount of fuel load when fuel type is set to grassland in Phoenix's default fuel table.

Fires in all realistic experiments are point ignition at the middle of the experiment domain, based on the actual burned area and observed wind direction. The ignition location coordinates are as listed in Table 5.3. List of observed weather data from the nearby

weather stations are as shown in Table 5.2. Satellite based fuel load patterns are as shown in Figure 6.1d (scenario R1), 6.1e (scenario R2), and 6.1f (scenario R3). Corresponding satellite based DOC patterns for scenarios with suffix C and D are as shown in Figure 5.1d (scenario R1), 5.1e (scenario R2), and 5.1f (scenario R3).

6.2 Grassland Fire Spread with Variable Fuel Load Results

6.2.1 *Idealised Experiments*

For each idealised experiment, we examine the mean fire spread speed and area burned after 5 hours as shown in Table 6.1 for both Phoenix and Spark models. Figure 6.2 shows a corresponding scatter plot for Phoenix's (black) and Spark's (blue) changes in mean rate of spread due to fuel load, respectively. Corresponding burned time step map for both Phoenix and Spark experiments are as shown in Figure 6.3. Note that the total area burned shown here is after 10 hours (at the end of the simulation). Figure 6.4 compares the rate of spread from the same idealised experiment scenarios between Phoenix and Spark models.

For scenario I1a to I1e, where fuel load gradually reduces from 20 to 2 t ha⁻¹, the rate of spread also decreases in proportion to the amount of available fuel for Spark. However, in case of Phoenix, the rate of spread oscillates between ~10 to ~18 km h⁻¹. This oscillation of rate of spread behaviour in Phoenix can also be clearly seen in scenario I2. Note that in scenario I2 for Spark, the rate of spread at the area with the highest fuel load (northern edge of the ignition line) is not the fastest, and the overall rate of spread at the area with equivalent fuel load level is slower than scenario I1 (see Figure 6.3). Overall rate of spread at high fuel load level is much faster in Spark than Phoenix.

For checkerboard pattern fuel load in scenario I3, the rate of spread is visibly hindered in Spark, showing a vertical wave pattern along the fire front and back fire, whereas in the case of Phoenix model, the rate of spread does not seem to be obstructed as much. Changes in terrain slope have similar influences on both Phoenix and Spark models, where the rate of spread is increased on the uphill and decreased on the downhill slope. The steeper the slope is, the larger the changes in the spread speed are.

Table 6.1 Idealised experiments average fire spread speed and area burned for Phoenix and Spark models.

Scenario	Fuel Load Configuration	Terrain Configuration	Phoenix		Spark	
			Average Fire Spread Speed (km h ⁻¹)	Area Burned (km ²) after 5 hours	Average Fire Spread Speed (km h ⁻¹)	Area Burned (km ²) after 5 hours
l1a	Homogeneous (20 t ha ⁻¹)	Flat	13.18	3,491.28	41.40	9,031.64
l1b	Homogeneous (15 t ha ⁻¹)	Flat	9.51	2,483.88	34.48	8,188.32
l1c	Homogeneous (10 t ha ⁻¹)	Flat	15.84	4,246.92	26.67	6,931.44
l1d	Homogeneous (5 t ha ⁻¹)	Flat	17.54	4,731.44	17.27	4,700.64
l1e	Homogeneous (2 t ha ⁻¹)	Flat	10.24	2,679.08	9.93	2,745.60
l2	Gradient (20 to 2 t ha ⁻¹)	Flat	9.36 to 18.39	3,565.80	7.29 to 27.41	6,556.88
l3	Checkerboard (4 & 8 t ha ⁻¹)	Flat	16.93 to 18.07	4,582.00	11.27 to 16.28	4,829.56
l4a	Homogeneous (20 t ha ⁻¹)	1° Downhill	12.23	3,245.20	38.93	9,009.44
l4b	Homogeneous (20 t ha ⁻¹)	5° Downhill	8.99	2,384.04	31.68	8,886.52
l4c	Homogeneous (20 t ha ⁻¹)	10° Downhill	5.76	1,521.44	27.20	8,718.48
l5a	Homogeneous (20 t ha ⁻¹)	1° Uphill	14.10	3,734.64	43.40	9,045.60
l5b	Homogeneous (20 t ha ⁻¹)	5° Uphill	18.57	4,923.56	52.94	9,101.96
l5c	Homogeneous (20 t ha ⁻¹)	10° Uphill	25.88	5,332.00	65.08	9,154.68

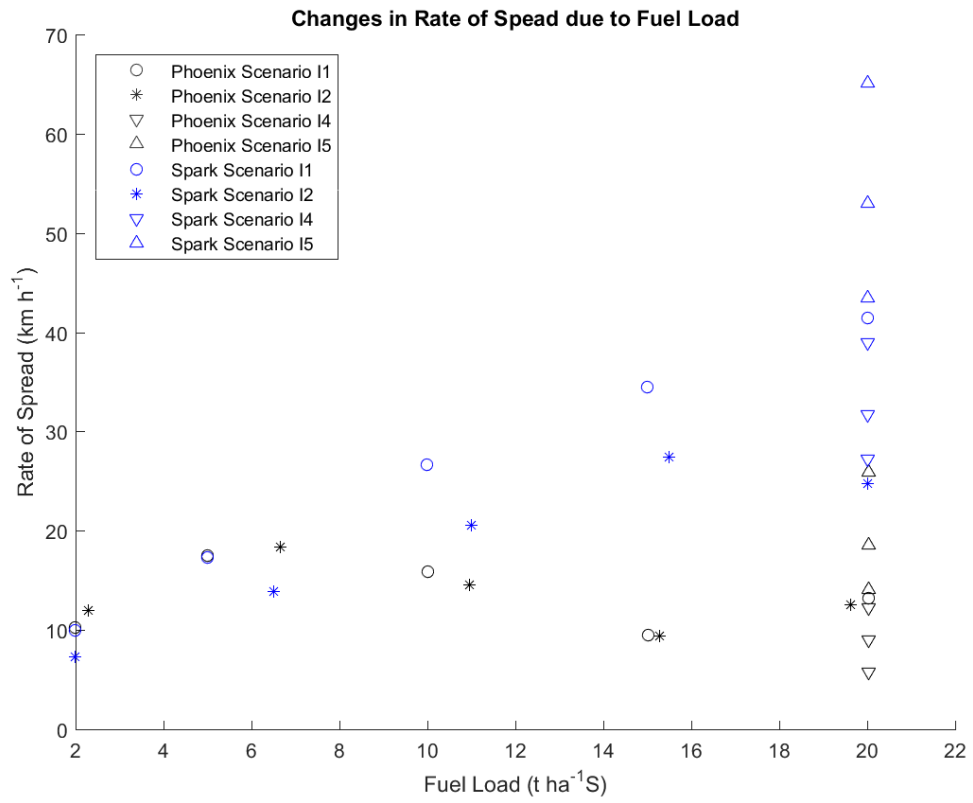


Figure 6.2 Changes in rate of spread due to changes in fuel load from Phoenix (black) and Spark (blue) idealised experiments.

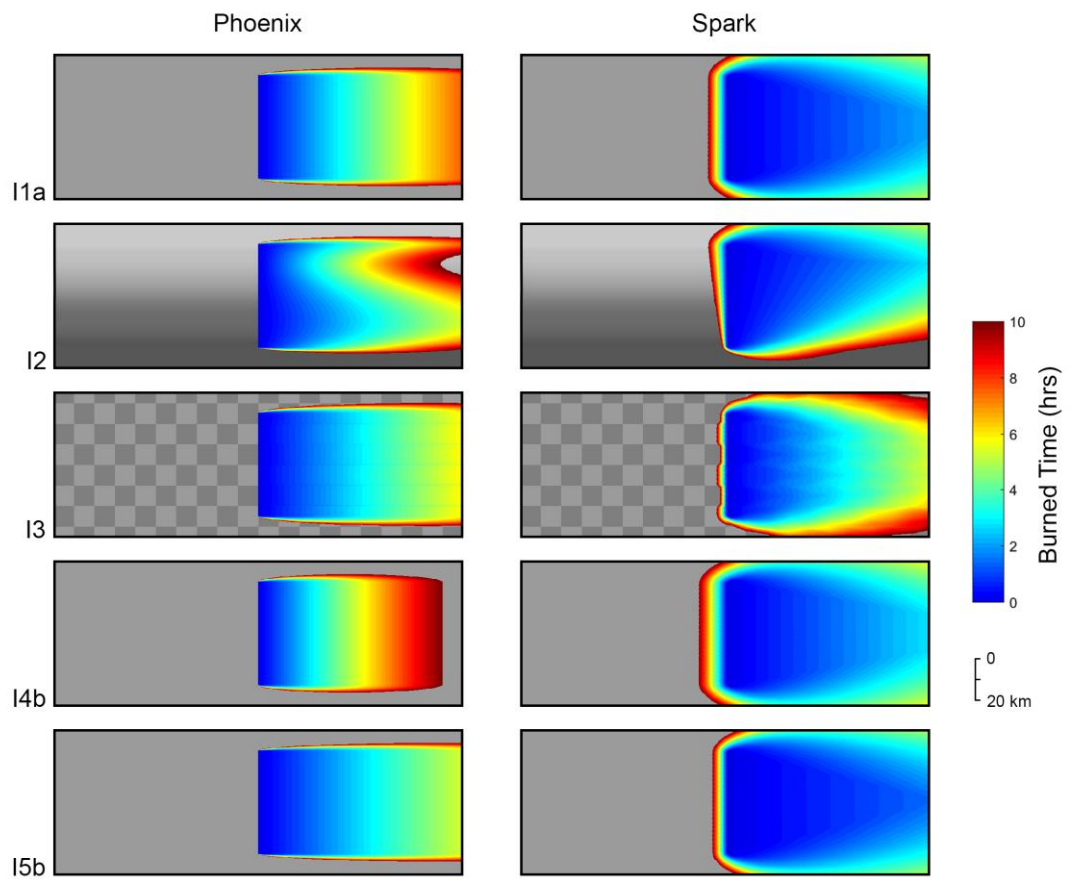


Figure 6.3 Phoenix and Spark idealised experiments burned time spatial maps. Grayscale backgrounds show the corresponding fuel load map from Figure 6.1. Only experiments I1a, I4b, and I5b are shown for scenario I1, I4, and I5.

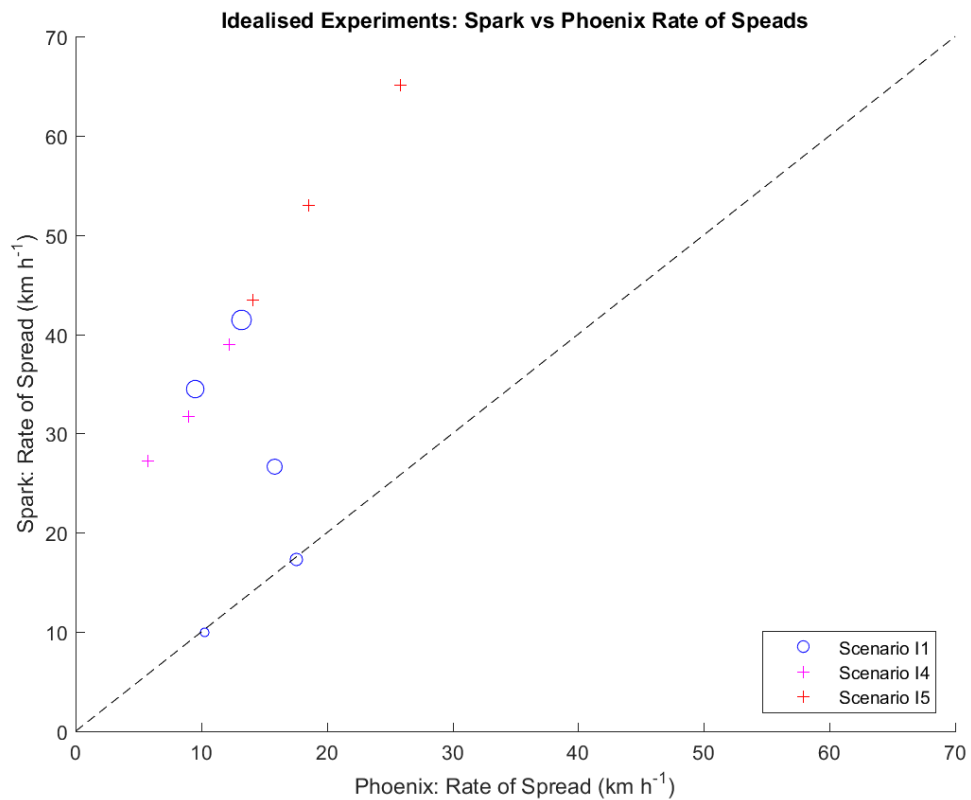


Figure 6.4 Rate of spread comparison between Phoenix and Spark idealised experiments. Only scenario I1, I4, and I5 are shown. The marker size of I1 represents the fuel load level (larger circle represents higher fuel load).

6.2.2 Realistic Experiments

For realistic experiments, we also examine the mean rate of spread and area burned after 5 hours, similarly to idealised experiments. Results are as shown in Table 6.2 for both Phoenix and Spark models. Corresponding burned time step map for both Phoenix and Spark experiments are as shown in Figure 6.5. Comparison between Phoenix and Spark rate of spread for each realistic scenario can be seen in the scatter plot in Figure 6.6.

The general satellite based fuel load within the fire perimeters for all scenarios are ranged between ~ 4 to ~ 7 t ha⁻¹, thus the variabilities between control fuel load scenario (suffix A) and other scenarios with satellite based fuel load are not very high (see Figure 6.1). However, this is not the case for DOC as shown in Figure 5.1 (panels d, e, and f), where DOC can be as low as $\sim 35\%$ and as high as $\sim 95\%$ across three locations. Since

fuel load level and variability is generally low for all scenarios, Phoenix rate of spread results are expected to be more stable than in idealised experiments.

For scenario R1 and R2, the rate of spreads for both Phoenix and Spark slightly increase when compared between homogeneous and satellite based fuel load (scenarios with suffix A and B), since overall satellite based fuel load within fire perimeters for both scenarios are slightly higher than homogeneous 5.1 t ha^{-1} fuel load, whereas for scenario R3, the satellite based fuel load is slightly lower, thus slight decrease in the rate of spread. There are large decreases in the rate of spreads, especially for scenario R1 and R2 when satellite based DOC is introduced (scenarios with suffix C). This is due to high variability of DOC and the large influence of DOC on the rate of spread. Note that DOC is at a consistently high level for scenario R3, thus a much less significant reduction in the rate of spread. The inclusion of digital elevation models to simulated realistic terrain has relatively small impact to the rate of spread in all scenarios (scenarios with suffix D), since the maximum changes in slopes are small (1.00° , 1.98° , and 0.21° for scenario R1, R2, and R3).

Both Phoenix and Spark models generally have similar behaviours when satellite based fuel load, satellite based DOC, and DEM are added. The changes in rate of spread and area burned are much more prominent when satellite based DOC is added. While the changes in the rate of spread in Phoenix and Spark are generally in the same direction, Spark's rate of spread are usually lower in control and scenarios with high DOC but higher when DOC is low (scenario R1-C, R1-D, R2-C and R2-D). Area burned in Spark can be larger than Phoenix, especially in more severe weather condition even if the spread speed is lower (scenario R3).

Table 6.2 Realistic experiments average fire spread speed and area burned for Phoenix and Spark models.

Scenario	Fuel Load Configuration	DOC Configuration	Terrain Configuration	Phoenix		Spark	
				Average Fire Spread Speed (km h ⁻¹)	Area Burned (km ²) after 5 hours	Average Fire Spread Speed (km h ⁻¹)	Area Burned (km ²) after 5 hours
R1-A (Control)	Homogeneous (5.1 t ha ⁻¹)	Homogeneous (100%)	Flat	4.95	87.12	3.31	55.60
R1-B	Toodyay, WA (Satellite)	Homogeneous (100%)	Flat	5.15	92.32	3.83	70.00
R1-C	Toodyay, WA (Satellite)	Toodyay, WA (Satellite)	Flat	1.14	15.20	2.38	52.24
R1-D	Toodyay, WA (Satellite)	Toodyay, WA (Satellite)	DEM (Max slope = 1.00°)	1.11	19.12	2.27	51.80
R2-A (Control)	Homogeneous (5.1 t ha ⁻¹)	Homogeneous (100%)	Flat	8.57	141.40	5.45	133.84
R2-B	Pulletop, NSW (Satellite)	Homogeneous (100%)	Flat	8.86	153.32	6.92	234.32
R2-C	Pulletop, NSW (Satellite)	Pulletop, NSW (Satellite)	Flat	0.24	0.76	4.19	65.12
R2-D	Pulletop, NSW (Satellite)	Pulletop, NSW (Satellite)	DEM (Max slope = 1.98°)	0.26	0.80	4.27	67.16
R3-A (Control)	Homogeneous (5.1 t ha ⁻¹)	Homogeneous (100%)	Flat	16.00	288.00	11.35	554.72

Scenario	Fuel Load Configuration	DOC Configuration	Terrain Configuration	Phoenix		Spark	
				Average Fire Spread Speed (km h ⁻¹)	Area Burned (km ²) after 5 hours	Average Fire Spread Speed (km h ⁻¹)	Area Burned (km ²) after 5 hours
R3-B	Jail Break Inn, NSW (Satellite)	Homogeneous (100%)	Flat	15.99	290.24	11.09	573.00
R3-C	Jail Break Inn, NSW (Satellite)	Jail Break Inn, NSW (Satellite)	Flat	11.59	163.96	9.94	484.40
R3-D	Jail Break Inn, NSW (Satellite)	Jail Break Inn, NSW (Satellite)	DEM (Max slope = 0.21°)	11.46	165.80	9.24	477.08

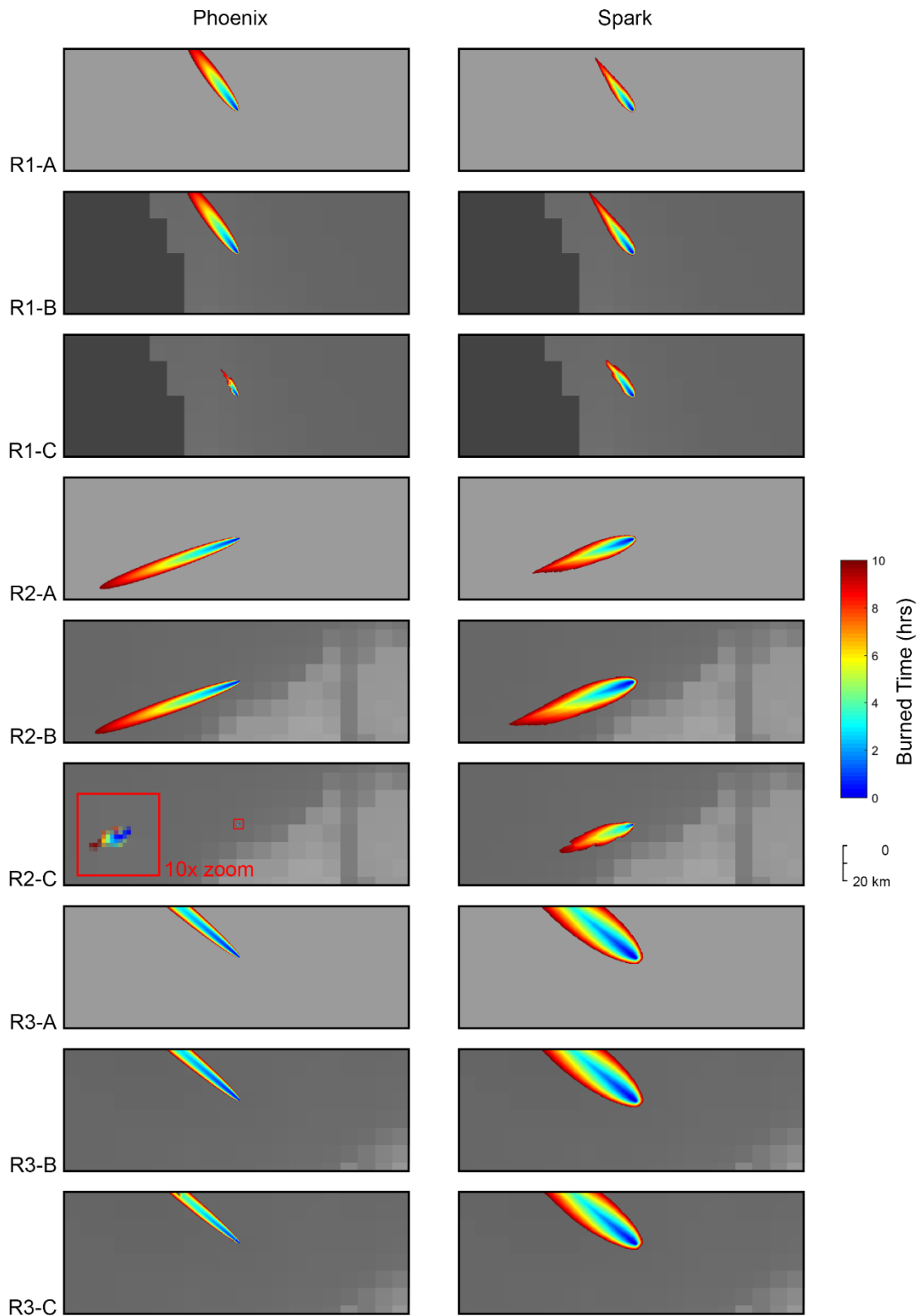


Figure 6.5 Phoenix and Spark realistic experiments burned time spatial maps. Grayscale backgrounds show the corresponding fuel load map from Figure 6.1. Scenarios with suffix D are not shown. For Phoenix's scenario R2-C, a 10 times magnifying burned area are shown with red bounding box insets.

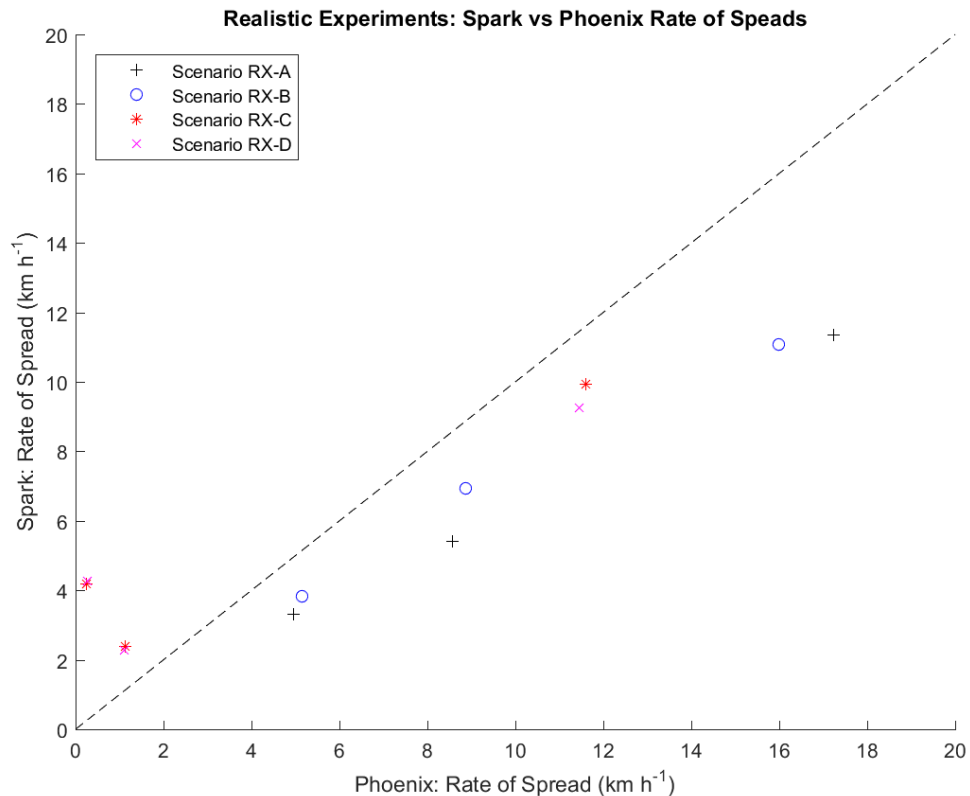


Figure 6.6 Rate of spread comparison between Phoenix and Spark realistic experiments, where X represents number ranging from 1 to 3 (scenario R1, R2, and R3).

6.3 Discussions

6.3.1 Grass Fire Spreads in Idealised Condition

From the idealised experiment results, the rate of spreads and their corresponding area burned for Phoenix are vastly different from Spark at fuel loads higher than 6.0 t ha⁻¹ due to the implementation of a reduction factor. According to Phoenix documentation, the rate of spread scaling factor should start to decrease from one when fuel load level is over 6.0 t ha⁻¹ (Tolhurst et al., 2007). We found that the rate of spread does decrease when fuel load is over 6.0 t ha⁻¹, but starts to rise again after ~15 t ha⁻¹, as seen in Figure 6.2 (black) for scenario I1 and I2. We are not aware of any physical mechanism that might account for this. Note that fuel load in grassland of certain pasture types can be as high as 14 t ha⁻¹, such as hummock grasses in Spinifex grasslands (Burrows et al.,

2009). Even Phoenix's default fuel table suggested that hummock grass fuel load level is at 15.5 t ha^{-1} . At a lower fuel load level (scenario I1d and I1e), we found that both Phoenix and Spark have a very similar rate of spread and area burned (see Figure 6.3 and Figure 6.4).

In contrast, Spark has a near direct linear relationship between fuel load level and the rate of spread (scenario I1). Though, there seems to be a slight drop off at the highest fuel load level on a gradient fuel layer (scenario I2). Overall rate of spread in gradient fuel scenario (I2) also seems to be slower than equivalent homogeneous fuel load scenario (I1), as seen in Figure 6.2 (blue). This is due to the effect of flank and backing fire spread rates.

For checkerboard pattern fuel load layer (scenario I3), Phoenix has a much more stable rate of spread pattern across the fuel bed than Spark. Alternating fuel load patterns does seem to slightly hinder the rate of spread in Phoenix, but the variation between the slowest and faster fire front is low (1.14 km h^{-1}), whereas the variation between the slowest and fastest fire front in Spark is a lot more prominent (5.01 km h^{-1}). This is due to the fact that the Phoenix's rate of spread peaked at fuel load of 6 t ha^{-1} (when ranged between 4 to 8 t ha^{-1}) as a result of the fire spread reduction factor in Phoenix. This is not the case for Spark experiments.

Changes in terrain slope in scenario I4 and I5 seem to result in similar trend for both Phoenix and Spark, as expected. As the slope becomes steeper, the rate of spread increases much more rapidly on an uphill slope. For downhill slope, the rate of spread decreases gradually, as shown in Figure 6.2 and 6.4. Note that the rate of spread and area burned in Spark is faster and larger than Phoenix due to the fire spread reduction factor in Phoenix.

6.3.2 Modelled Grass Fire Spreads from Past Events

For realistic experiments, the variability in fuel load between each scenario and past fire location is not as high as the variability in idealised experiments, with the fuel load level in the fire perimeters ranging from ~ 4 to 7 t ha^{-1} (control scenario fuel load is 5.1 t ha^{-1}). Phoenix and Spark have a closer rate of spread predictions than idealised experiments due to narrower fuel load range. Note that some of Phoenix's spread rate and burned area results are faster and larger than Spark's (scenario R1-A, R1-B, and R2-A), as

opposed to the comparison results in idealised test. Though, in scenario R3, while Phoenix has a faster rate of spread, Spark's area burned is larger. This is due to the way Spark handles fire ignition, where line ignition (in idealised experiments) is considered as a very thin rectangular ignition shape and point ignition (in realistic experiments) is considered as a very small circular ignition shape. Thus, having a larger ignition area, fire lit by line ignition spreads faster than fire lit by point ignition. For Phoenix, we do not know how point and line ignition is handled differently. We also make an idealised comparison between Phoenix and Spark with point ignition and found that Phoenix indeed has faster rate of spread prediction, as opposed to line ignition.

The changes made by swapping the homogeneous 5.1 t ha^{-1} gridded fuel load with satellite based fuel load (scenarios with suffix A to B) results in much smaller changes in both spread rate and area burned than swapping the homogenous 100% gridded DOC with satellite based DOC (scenarios with suffix B to C). This is expected, since it is suggested in past studies that DOC has a larger influence on a grassland fires severity than fuel load (Cheney et al., 1998; Cruz et al., 2015; Kidnie et al., 2015). It is also partly due to spatial variability in DOC being larger than that in fuel load. Both Phoenix and Spark react similarly with the changes from homogeneous to satellite based fuel load, where the rate of spread increases when overall fuel load is higher (scenario R1-A to R1-B and R2-A to R2-B) and decreases when overall fuel load is lower (scenario R3-A to R3-B) as shown in Figure 6.5 and Figure 6.6. Note that the area burned is not necessarily smaller as the rate of spread is decreased in scenario R3 for both Phoenix and Spark. This is due to the differences in fire propagation on a homogeneous gridded fuel load and spatially variable fuel load.

While Phoenix and Spark handle gradual changes in fuel load in a similar manner, changes in DOC (scenarios with suffix B to C) lead to different responses in Phoenix and Spark. For scenario R1-C and R2-C, where the DOC within some areas of the fire perimeter is generally low (~50 to 60% for R1-C and ~45 to 55% for R2-C), Spark predicts a significantly faster rate of spreads than Phoenix. In contrast, for scenario R3-C, where the DOC within the fire perimeter is consistently high (~85 to 95%) throughout the fire perimeter, Phoenix predicts a faster spread rate than Spark. This can be clearly seen in Figure 6.6 as the data points for the low DOC scenarios are the only data points indicating that Spark's spread rate is faster than Phoenix's. This is due to the different curing coefficients used (Cheney's in Phoenix and Cruz's in Spark), where Cheney's curing coefficient suggested that fire is not likely to spread when DOC is less than 50%

(Cheney et al., 1998), as opposed to a more recent finding by Cruz that suggested a grassland fire can spread on a fuel complex with DOC as low as 20% (Cruz et al., 2015).

The added DEM in scenarios with suffix D slightly alters the rate of spreads similarly for both Phoenix and Spark. The changes in area burned due to the inclusion of a more realistic terrain are, however, not always in the same direction for Phoenix and Spark. In the changes from R1-C to R1-D and R3-C to R3-D, Phoenix suggested the area burned to be larger, whereas Spark suggested the opposite. This is likely due to Phoenix and Spark handling fire propagation and slope modification differently, but since we do not have access to Phoenix source codes, this dissimilarity is unclear.

6.3.3 *Limitations*

Both Phoenix and Spark have their own distinct features. Phoenix is well-established and feature rich, since it was developed well before Spark, whereas Spark has much more flexibility in letting the users define their own rate of spread and post processing model. However, there are certainly some concerning limitations with both Phoenix and Spark.

Though Phoenix is very feature rich, its source code is not available so the model behaviour can be unexpected. We found that at high fuel load scenarios (fuel load over 15 t ha^{-1}), which is possible for some pasture types, there is no clear explanation why Phoenix's predicted rate of spread starts to increase again after being suppressed by drawback from the high heat generated when fuel load is over 6 t ha^{-1} as asserted in Tolhurst et al. (2007). If we no longer considered the effect of drawback, then the overall rate of spread prediction is even odder, since the rate of spread drops and rise again even when fuel load is constantly increasing (see Figure 6.2). Thus, we do not recommend using Phoenix to predict grassland fire spread where fuel load is significantly higher than 6 t ha^{-1} .

While Spark customisability is its strong suite, it can be a double edge sword for novice users. Though its online database has a small collection of fire behaviour models to choose from, inexperienced users are stuck with using simple fire behaviour simulation, since more advance components need to be added manually. Note that the predicted results can be vastly different from one another, depending on the specified behaviour

components. Though Phoenix offers multiple output variables, Spark only outputs the shape of the burned area and associated time steps.

7 Conclusions

With a coverage of nearly 75% over Australia, grassland is one of the most widespread fuel type in Australia (Cheney and Sullivan, 2008). While there are efforts being dedicated to grassland fire management and prediction, there are still uncertainties in assessing the grassland fire severity. To help close the gap in grassland fire studies, the first part of this thesis (Chapter 3 and 4) focused on monitoring grassland degree of curing (DOC) and fuel load over Australia with satellite observations. This helps expand the limited observation of both DOC and fuel load in Australia both spatially and temporally. In the second part of this thesis (Chapter 5 and 6), the influence of DOC and fuel load (produced as gridded data in the first part) on grassland fire spread were assessed with grassland fire behaviour models. The research questions addressed here are: How does DOC and fuel load vary spatially and temporally over Australia? How do variations in DOC and fuel load impact modelled fire spread?

During the first part of this study, the new methods for estimating grassland DOC and fuel load across Australia using recently developed microwave based satellite data (VOD) were established. For DOC estimation, various past studies (Martin et al., 2015; Newnham et al., 2011, 2010) suggested using optical based satellite data, such as NDVI, to construct DOC estimation model for regional and continental scale. After several combinations of calibration tests with both VOD and NDVI and observed DOC sites, the two best performing calibrated models for estimating DOC over Australia at 0.05° spatial and 8 day temporal interval were selected ($r^2 = 0.67$ for the first model and $r^2 = 0.54$ for the second model). Both model was then evaluated with partially and totally independent observation data and found to have a good fit ($r^2 = 0.55$ and 0.44 for the first model and $r^2 = 0.50$ and 0.54 for the second model in case of all sites and independent evaluation, respectively). The first model is chose in this case, since the included terms in the model are selected with stepwise fit algorithm without my interference. It was found that the continental mean of DOC over Australia from mid-2002 to mid-2011 is 85.70% with mean spatial standard deviation of 20.39% indicating significant spatial variability across all years and mean temporal standard deviation of 11.88% with strong temporal variability in southeast and southwest areas. GFDI over Australia for predicting fire risk can be computed with DOC estimated from VOD and NDVI. Comparing the GFDI calculated from VOD and NDVI model with existing DOC products (Method B and MapVic), showed that the model I developed had a comparable and arguably more balanced performance

in predicting the observed burned area through GFDI. While there are still some uncertainties in the predicted DOC (RMSE ranging from 15.25% to 16.76% for both first and second DOC model), my models (partly microwave and optical-based) can also be used as an alternative to other solely optical-based models.

After the DOC estimation model was constructed, a fuel load estimation model over Australia was considered. However, this was more challenging than DOC estimation model, since there were no previous studies that successfully constructed a fuel load estimation model at a continental scale. Most past studies (Brandis and Jacobson, 2003; Jin and Chen, 2012; Reich et al., 2004) were focused on high resolution fuel load estimation model at a regional or smaller scale. To achieve a total spatial coverage over Australia and at least annual temporal interval, I decided to use AGBC data that was based on VOD for calibrating fuel load estimation model. Though it should be noted that the resultant estimated fuel load data will have only moderate (0.1°) spatial resolution. After multiple attempts with several site observed fuel load data and methods, a significant correlation between AGBC and observed fuel load is only found at bioregion level. This was due to the spatial mismatch between fuel load observation at site level and AGBC (VOD) pixels, while this was not an issue for fuel load observation at bioregion level, since the spatial scale was more comparable to AGBC (VOD) pixels. The Australian general fuel load model was then developed from the calibration of AGBC and bioregion fuel load data ($r^2 = 0.74$). Since there was no additional fuel load data available for model evaluation, a vegetation structure dataset was used to evaluate the AGBC data used for developing fuel load model. It was found that AGBC had an excellent fit ($r^2 = 0.82$) with vegetation structure data. The continental mean of fuel load from 2003 to 2011 was 5.95 t ha^{-1} with mean spatial standard deviation of 2.50 t ha^{-1} (highest spatial variability in 2011) and mean temporal standard deviation of 0.54 t ha^{-1} with strong temporal variability along the east coast.

For the second part of this study, the grassland fire behaviour, particularly the rate of fire spread, was assessed using the previously developed satellite based estimations of DOC and fuel load data and fire spread prediction software, Phoenix and Spark. To test the sensitivity of the predicted rate of spread in grasslands to DOC and fuel load, I used sets of idealised and realistic experiments examine the changes in the rate of spread in various conditions. For varying DOC, fire propagation over a homogeneous grassland fuel bed was heavily dictated by the level of DOC, according to each models' respective curing coefficient. Fire propagation became difficult and started to stagnate when the

DOC was below the suggested propagation threshold of 50% for Phoenix (Cheney et al., 1998) and 20% for Spark (Cruz et al., 2015). Extreme weather conditions were also required for fire propagation under a low DOC level. Phoenix and Spark had quite different predictions in terms of the rate of spread at low and uneven DOC levels, burned perimeters, and slope effects on spread rate, which can be clearly observed in the realistic experiments. For instance, in a realistic experiment at Pulletop, NSW (scenario I2-B), the predicted rate of spread by Phoenix was 0.22 km h^{-1} , while Spark prediction was 2.99 km h^{-1} .

As for the variability in the rate of spread due to variation in fuel load for both Phoenix and Spark model, I assumed that the fuel load was related to the changes in grassland continuity. Though both Phoenix and Spark had some similarity in grassland fire spread prediction at low fuel load levels (6 t ha^{-1} or less), the differences in the predicted results at high fuel load were very large. In idealised experiments with high fuel load (i.e. scenario I1a, where Phoenix and Spark rate of spreads were 13.18 km h^{-1} and 41.40 km h^{-1} , respectively), Phoenix's rate of spread predictions questionable due to its internal implementation of rate of spread modification factor, while Spark was more consistent. On the other hand, in realistic experiments with generally low fuel load and high DOC, both Phoenix and Spark simulated results were more consistent (i.e. scenario R2-B, where Phoenix and Spark rate of spreads were 8.86 km h^{-1} and 6.92 km h^{-1} , respectively). It should also be noted that the effect of fuel load on the rate of spread was not as prominent as the effect of DOC. Great care was recommended when simulating a grassland fire with high fuel load or low DOC, since the predicted results can be very different depending on the model selected (Phoenix or Spark), and how the behaviour components were specified in case of Spark, since different curing coefficients, flank and back fire algorithms, and slopes can alter the magnitude of the rate of spread and burned area.

With comparable performance to the current DOC products, the DOC model developed here can be an appealing alternative for GFDI computation and fire risk modelling. For the developed estimated fuel load data, though its spatial and temporal resolutions are quite limited when compared with the developed DOC model (and other existing fuel load models in terms of spatial resolution), the fuel load model developed here can provide a good overall annual snapshot of fuel load variation across Australia. It was found that both DOC and fuel load had significant spatial variabilities that persist across all available temporal periods, while temporal variabilities were strong in particular areas (southeast

and southwest area for DOC and east coast for fuel load). Both satellite based DOC and fuel load data developed here were shown to be useful in the rate of spread prediction by different fire behaviour software packages (Phoenix and Spark). Though there was no exact indication of which was the best model between Phoenix and Spark, the study illustrated how similarly and differently Phoenix and Spark reacted to variations in DOC and fuel load. It should also be noted that while Phoenix had more additional features and a more complete fire risk package, Spark offered a much higher degree of flexibility in defining the fire spread behaviour components and updating the model. With enough support from the bushfire communities, Spark is a more appealing alternative. Better climatological observations and remote sensing techniques that can provide higher temporal (preferably sub-daily or hourly interval) and spatial resolutions to both weather and fuel data are a must for better fire spread predictions in the future. This thesis highlights the importance of monitoring the current spatial variation in fuel properties for accurate fire spread modelling and risk assessment, such as using satellite estimated DOC in GFDI yields better fire danger classification based on past burned areas comparison. Fire spread models' prediction results and sensitivities can also be explored in a more realistic simulation with estimated DOC and fuel load. This thesis also demonstrates the utility of using idealised experiments to test and understand fire spread model behaviour that, for instance, shows how different Phoenix's and Spark's predictions are at high grasslands fuel load. Further development and improvement of the models, such as improving Phoenix's flexibility to allow user modification to the embedded spread model or push for Spark adoption instead of Phoenix when it is fully developed.

References

- Alexander, L.V., Arblaster, J.M., 2017. Historical and projected trends in temperature and precipitation extremes in Australia in observations and CMIP5. *Weather Clim. Extrem.* 15, 34–56. <https://doi.org/10.1016/j.wace.2017.02.001>
- Alexander, M.E., 1985. Estimating the length-to-breadth ratio of elliptical forest fire patterns. Presented at the Proceedings of the Eighth Conference on Fire and Forest Meteorology, Detroit, Michigan, pp. 287–304.
- Allan, G., Johnson, A., Cridland, S., Fitzgerald, N., 2003. Application of NDVI for predicting fuel curing at landscape scales in northern Australia: can remotely sensed data help schedule fire management operations? *Int. J. Wildland Fire* 12, 299–308.
- Andela, N., Liu, Y.Y., van Dijk, A.I.J.M., de Jeu, R.A.M., McVicar, T.R., 2013. Global changes in dryland vegetation dynamics (1988–2008) assessed by satellite remote sensing: comparing a new passive microwave vegetation density record with reflective greenness data. *Biogeosciences* 10, 6657–6676. <https://doi.org/10.5194/bg-10-6657-2013>
- Andela, N., van der Werf, G.R., 2014. Recent trends in African fires driven by cropland expansion and El Niño to La Niña transition. *Nat. Clim. Change* 4, 791–795. <https://doi.org/10.1038/nclimate2313>
- Anderson, D.H., Catchpole, E.A., De Mestre, N.J., Parkes, T., 1982. Modelling the spread of grass fires. *J. Aust. Math. Soc., B* 23, 451–466.
- Anderson, S.A.J., Anderson, W.R., Hollis, J.J., Botha, E.J., 2011. A simple method for field-based grassland curing assessment. *Int. J. Wildland Fire* 20, 804–814.
- Arroyo, L.A., Pascual, C., Manzanera, J.A., 2008. Fire models and methods to map fuel types: the role of remote sensing. *Fire Ecol. Manag.* 256, 1239–1252.
- Booth, J.F., Kwon, Y.-O., Ko, S., Small, R.J., Msadek, R., 2017. Spatial patterns and intensity of the surface storm tracks in CMIP5 models. *J. Clim.* 30, 4965–4981. <https://doi.org/10.1175/JCLI-D-16-0228.1>
- Bradstock, R.A., Hammill, K.A., Collins, L., Price, O., 2010. Effects of weather, fuel and terrain on fire severity in topographically diverse landscapes of south-eastern Australia. *Landsc. Ecol.* 25, 607–619. <https://doi.org/10.1007/s10980-009-9443-8>
- Brandis, K., Jacobson, C., 2003. Estimation of vegetative fuel loads using Landsat TM imagery in New South Wales, Australia. *Int. J. Wildland Fire* 12, 185–194.
- Brandt, M., Yue, Y., Wigneron, J.P., Tong, X., Tian, F., Jepsen, M.R., Xiao, X., Verger, A., Mialon, A., Al-Yaari, A., Wang, K., Fensholt, R., 2018. Satellite-Observed Major Greening and Biomass Increase in South China Karst During Recent Decade. *Earths Future* 6, 1017–1028. <https://doi.org/10.1029/2018EF000890>
- Burrell, A.L., Evans, J.P., Liu, Y., 2017. Detecting dryland degradation using Time Series Segmentation and Residual Trend analysis (TSS-RESTREND). *Remote Sens. Environ.* 197, 43–57. <https://doi.org/10.1016/j.rse.2017.05.018>
- Burrows, N.D., Ward, B., Robinson, A., 2009. Fuel dynamics and fire spread in Spinifex grasslands of the Western Desert. *Proc. R. Soc. Qld.* 115, 69.
- Ceccato, P., Gobron, N., Flasse, S., Pinty, B., Tarantola, S., 2002. Designing a spectral index to estimate vegetation water content from remote sensing data: Part 1: Theoretical approach. *Remote Sens. Environ.* 82, 188–197. [https://doi.org/10.1016/S0034-4257\(02\)00037-8](https://doi.org/10.1016/S0034-4257(02)00037-8)
- Chaivaranont, W., Evans, J.P., Liu, Y.Y., Sharples, J.J., 2018. Estimating grassland curing with remotely sensed data. *Nat Hazards Earth Syst Sci* 18, 1535–1554. <https://doi.org/10.5194/nhess-18-1535-2018>

- Chang, K., Tsai, B., 1991. The effect of DEM resolution on slope and aspect mapping. *Cartogr. Geogr. Inf. Syst.* 18, 69–77. <https://doi.org/10.1559/152304091783805626>
- Chen, T., de Jeu, R.A.M., Liu, Y.Y., van der Werf, G.R., Dolman, A.J., 2014. Using satellite based soil moisture to quantify the water driven variability in NDVI: a case study over mainland Australia. *Remote Sens. Environ.* 140, 330–338. <https://doi.org/10.1016/j.rse.2013.08.022>
- Cheney, N., Gould, J., Catchpole, W., 1998. Prediction of fire spread in grasslands. *Int. J. Wildland Fire* 8, 1–13.
- Cheney, P., Sullivan, A., 2008. *Grassfires: Fuel, weather and fire behaviour*, 2nd ed. CSIRO Publishing, Melbourne.
- Chladil, M., Nunez, M., 1995. Assessing grassland moisture and biomass in Tasmania - the application of remote-sensing and empirical-models for a cloudy environment. *Int. J. Wildland Fire* 5, 165–171.
- Clarke, H., Evans, J.P., Pitman, A.J., 2013a. Fire weather simulation skill by the Weather Research and Forecasting (WRF) model over south-east Australia from 1985 to 2009. *Int. J. Wildland Fire* 22, 739–756. <https://doi.org/10.1071/WF12048>
- Clarke, H., Lucas, C., Smith, P., 2013b. Changes in Australian fire weather between 1973 and 2010. *Int. J. Climatol.* 33, 931–944. <https://doi.org/10.1002/joc.3480>
- Cobb, R.C., Meentemeyer, R.K., Rizzo, D.M., 2016. Wildfire and forest disease interaction lead to greater loss of soil nutrients and carbon. *Oecologia* 1–12. <https://doi.org/10.1007/s00442-016-3649-7>
- Collins, L., Penman, T.D., Price, O.F., Bradstock, R.A., 2015. Adding fuel to the fire? Revegetation influences wildfire size and intensity. *J. Environ. Manage.* 150, 196–205. <https://doi.org/10.1016/j.jenvman.2014.11.009>
- Contractor, S., Alexander, L.V., Donat, M.G., Herold, N., 2015. How well do gridded datasets of observed daily precipitation compare over Australia? *Adv. Meteorol.* 2015. <https://doi.org/10.1155/2015/325718>
- Cruz, M.G., Gould, J.S., Kidnie, S., Bessell, R., Nichols, D., Slijepcevic, A., 2015. Effects of curing on grassfires: II. effect of grass senescence on the rate of fire spread. *Int. J. Wildland Fire* 24, 838–848. <https://doi.org/10.1071/WF14146>
- Dee, D.P., Uppala, S.M., Simmons, A.J., Berrisford, P., Poli, P., Kobayashi, S., Andrae, U., Balmaseda, M.A., Balsamo, G., Bauer, P., Bechtold, P., Beljaars, A.C.M., van de Berg, L., Bidlot, J., Bormann, N., Delsol, C., Dragani, R., Fuentes, M., Geer, A.J., Haimberger, L., Healy, S.B., Hersbach, H., Hólm, E.V., Isaksen, I., Kållberg, P., Köhler, M., Matricardi, M., McNally, A.P., Monge-Sanz, B.M., Morcrette, J.-J., Park, B.-K., Peubey, C., de Rosnay, P., Tavolato, C., Thépaut, J.-N., Vitart, F., 2011. The ERA-Interim reanalysis: configuration and performance of the data assimilation system. *Q. J. R. Meteorol. Soc.* 137, 553–597. <https://doi.org/10.1002/qj.828>
- DeLong, E.R., DeLong, D.M., Clarke-Pearson, D.L., 1988. Comparing the areas under two or more correlated receiver operating characteristic curves: a nonparametric approach. *Biometrics* 44, 837–845.
- Deslandes, R., Jacobs, H., 2017. An evaluation of fire simulators used in Australia (No. 1.81). *Bushfire Predictive Services*, Bureau of Meteorology.
- Dilley, A.C., Millie, S., O'Brien, D.M., Edwards, M., 2004. The relation between Normalized Difference Vegetation Index and vegetation moisture content at three grassland locations in Victoria, Australia. *Int. J. Remote Sens.* 25, 3913–3930. <https://doi.org/10.1080/01431160410001698889>
- Donohue, R.J., McVicar, T.R., Roderick, M.L., 2009. Climate-related trends in Australian vegetation cover as inferred from satellite observations, 1981–2006. *Glob. Change Biol.* 15, 1025–1039. <https://doi.org/10.1111/j.1365-2486.2008.01746.x>
- Dorado-Moreno, M., Cornejo-Bueno, L., Gutiérrez, P.A., Prieto, L., Hervás-Martínez, C., Salcedo-Sanz, S., 2017. Robust estimation of wind power ramp events with

- reservoir computing. *Renew. Energy* 111, 428–437. <https://doi.org/10.1016/j.renene.2017.04.016>
- Draper, N.R., Smith, H., 1998. *Applied regression analysis*, 3rd ed. Wiley-Interscience, Hoboken, NJ.
- Evans, J., Geerken, R., 2004. Discrimination between climate and human-induced dryland degradation. *J. Arid Environ.* 57, 535–554. [https://doi.org/10.1016/S0140-1963\(03\)00121-6](https://doi.org/10.1016/S0140-1963(03)00121-6)
- Exbrayat, J.-F., Liu, Y.Y., Williams, M., 2017. Impact of deforestation and climate on the Amazon Basin's above-ground biomass during 1993–2012. *Sci. Rep.* 7, 15615. <https://doi.org/10.1038/s41598-017-15788-6>
- Falkowski, M.J., Gessler, P.E., Morgan, P., Hudak, A.T., Smith, A.M.S., 2005. Characterizing and mapping forest fire fuels using ASTER imagery and gradient modeling. *For. Ecol. Manag.* 217, 129–146.
- Gazzard, R., McMorrow, J., Aylen, J., 2016. Wildfire policy and management in England: an evolving response from Fire and Rescue Services, forestry and cross-sector groups. *Phil Trans R Soc B* 371, 20150341. <https://doi.org/10.1098/rstb.2015.0341>
- Geoscience Australia, 2016. ELVIS - Elevation Information System [WWW Document]. ELVIS - Elev. Inf. Syst. URL <http://www.ga.gov.au/elvis/> (accessed 6.8.16).
- Gilroy, J., Tran, C., 2009. A new fuel load model for eucalypt forests in Southeast Queensland. *Proc. R. Soc. Qld.* 115, 137–143.
- Guglielmetti, M., Schwank, M., Mätzler, C., Oberdörster, C., Vanderborght, J., Flüher, H., 2007. Measured microwave radiative transfer properties of a deciduous forest canopy. *Remote Sens. Environ.* 109, 523–532. <https://doi.org/10.1016/j.rse.2007.02.003>
- Hansen, M.C., Defries, R.S., Townshend, J.R.G., Sohlberg, R., 2000. Global land cover classification at 1km resolution using a decision tree classifier. *Int. J. Remote Sens.* 21, 1331–1365.
- Harris, S., Mills, G., Brown, T., 2017. Variability and drivers of extreme fire weather in fire-prone areas of south-eastern Australia. *Int. J. Wildland Fire* 26, 177–190. <https://doi.org/10.1071/WF16118>
- Hilton, J.E., Miller, C., Sharples, J.J., Sullivan, A.L., 2017. Curvature effects in the dynamic propagation of wildfires. *Int. J. Wildland Fire* 25, 1238–1251. <https://doi.org/10.1071/WF16070>
- Hilton, J.E., Miller, C., Sullivan, A.L., 2016. A power series formulation for two-dimensional wildfire shapes. *Int. J. Wildland Fire* 25, 970–979. <https://doi.org/10.1071/WF15191>
- Hilton, J.E., Miller, C., Sullivan, A.L., Rucinski, C., 2015. Effects of spatial and temporal variation in environmental conditions on simulation of wildfire spread. *Environ. Model. Softw.* 67, 118–127. <https://doi.org/10.1016/j.envsoft.2015.01.015>
- Hornby, L.G., 1935. Fuel type mapping in region one. *J. For.* 33, 67–72.
- Hudec, J.L., Peterson, D.L., 2012. Fuel variability following wildfire in forests with mixed severity fire regimes, Cascade Range, USA. *For. Ecol. Manag.* 277, 11–24. <https://doi.org/10.1016/j.foreco.2012.04.008>
- Hutson, B.R., 1985. Rates of litterfall and organic matter turnover at three South Australian indigenous forest sites. *Aust. J. Ecol.* 10, 351–359. <https://doi.org/10.1111/j.1442-9993.1985.tb00896.x>
- Jackson, T.J., Schmutge, T.J., 1991. Vegetation effects on the microwave emission of soils. *Remote Sens. Environ.* 36, 203–212.
- Jin, S., Chen, S.-C., 2012. Application of QuickBird imagery in fuel load estimation in the Daxinganling region, China. *Int. J. Wildland Fire* 21, 583–590.
- Jones, D.A., Wang, W., Fawcett, R., 2009. High-quality spatial climate data-sets for Australia. *Aust. Meteorol. Oceanogr. J.* 58, 233–248.

- Jones, M.O., Jones, L.A., Kimball, J.S., McDonald, K.C., 2011. Satellite passive microwave remote sensing for monitoring global land surface phenology. *Remote Sens. Environ.* 115, 1102–1114. <https://doi.org/10.1016/j.rse.2010.12.015>
- Jurdao, S., Chuvieco, E., Arevalillo, J.M., 2012. Modelling fire ignition probability from satellite estimates of live fuel moisture content. *Fire Ecol.* 7, 77–97. <https://doi.org/10.4996/fireecology.0801077>
- Keane, R.E., Burgan, R., van Wageningen, J., 2001. Mapping wildland fuels for fire management across multiple scales: Integrating remote sensing, GIS, and biophysical modeling. *Int. J. Wildland Fire* 10, 301–319.
- Kerr, Y.H., Njoku, E.G., 1990. A semiempirical model for interpreting microwave emission from semiarid land surfaces as seen from space. *IEEE Trans. Geosci. Remote Sens.* 28, 384–393. <https://doi.org/10.1109/36.54364>
- Kidnie, S., Cruz, M.G., Gould, J., Nichols, D., Anderson, W., Bessell, R., 2015. Effects of curing on grassfires: I. fuel dynamics in a senescing grassland. *Int. J. Wildland Fire* 24, 828–837.
- Knight, I., Coleman, J., 1993. A fire perimeter expansion algorithm-based on Huygens wavelet propagation. *Int. J. Wildland Fire* 3, 73–84.
- Liu, N., Harper, R. J., Dell, B., Liu, S., Yu, Z., 2017. Vegetation dynamics and rainfall sensitivity for different vegetation types of the Australian continent in the dry period 2002–2010. *Ecology* 10, n/a-n/a. <https://doi.org/10.1002/eco.1811>
- Liu, Y.Y., de Jeu, R.A.M., McCabe, M.F., Evans, J.P., van Dijk, A.I.J.M., 2011. Global long-term passive microwave satellite-based retrievals of vegetation optical depth. *Geophys. Res. Lett.* 38, n/a–n/a. <https://doi.org/10.1029/2011GL048684>
- Liu, Y.Y., Evans, J.P., McCabe, M.F., de Jeu, R.A.M., van Dijk, A.I.J.M., Dolman, A.J., Saizen, I., 2013a. Changing climate and overgrazing are decimating Mongolian steppes. *PLoS ONE* 8, e57599. <https://doi.org/10.1371/journal.pone.0057599>
- Liu, Y.Y., van Dijk, A.I.J.M., de Jeu, R.A.M., Canadell, J.G., McCabe, M.F., Evans, J.P., Wang, G., 2015. Recent reversal in loss of global terrestrial biomass. *Nat. Clim. Change* 5, 470–474. <https://doi.org/10.1038/nclimate2581>
- Liu, Y.Y., van Dijk, A.I.J.M., McCabe, M.F., Evans, J.P., de Jeu, R.A.M., 2013b. Global vegetation biomass change (1988–2008) and attribution to environmental and human drivers. *Glob. Ecol. Biogeogr.* 22, 692–705. <https://doi.org/10.1111/geb.12024>
- Louis, S.A., Matthews, S., 2015. Fire spread prediction using a lagged weather forecast ensemble. Presented at the 21st International Congress on Modelling and Simulation, Gold Coast, Australia.
- Lucas, C., 2010. On developing a historical fire weather data-set for Australia. *Aust. Meteorol. Oceanogr. J.* 60, 1–14.
- Lucas, R., Armston, J., Scarth, P., Bunting, P., 2015. Contribution of ALOS PALSAR data to forest characterization and monitoring in Australia, in: 2015 IEEE International Geoscience and Remote Sensing Symposium (IGARSS). Presented at the 2015 IEEE International Geoscience and Remote Sensing Symposium (IGARSS), pp. 2630–2633. <https://doi.org/10.1109/IGARSS.2015.7326352>
- Lucas, R.M., Clewley, D., Accad, A., Butler, D., Armston, J., Bowen, M., Bunting, P., Carreiras, J., Dwyer, J., Eyre, T., Kelly, A., McAlpine, C., Pollock, S., Seabrook, L., 2014. Mapping forest growth and degradation stage in the Brigalow Belt Bioregion of Australia through integration of ALOS PALSAR and Landsat-derived foliage projective cover data. *Remote Sens. Environ.* 155, 42–57. <https://doi.org/10.1016/j.rse.2013.11.025>
- Luke, R.H., McArthur, A.G., 1978. Bushfires in Australia. Australian Government Publishing Service for CSIRO, Canberra, Australia.

- Martin, D., Chen, T., Nichols, D., Bessell, R., Kidnie, S., Alexander, J., 2015. Integrating ground and satellite-based observations to determine the degree of grassland curing. *Int. J. Wildland Fire* 24, 329–339.
- McArthur, A.G., 1967. Fire behaviour in eucalypt forests. Forestry and Timber Bureau, Canberra.
- McCaw, W.L., Gould, J.S., Phillip Cheney, N., Ellis, P.F.M., Anderson, W.R., 2012. Changes in behaviour of fire in dry eucalypt forest as fuel increases with age. *For. Ecol. Manag.* 271, 170–181. <https://doi.org/10.1016/j.foreco.2012.02.003>
- McLeod, R., 2003. Inquiry into the operational response to the January 2003 bushfires in the ACT. ACT Government, Canberra, Australia.
- Meesters, A.G.C.A., de Jeu, R.A.M., Owe, M., 2005. Analytical derivation of the vegetation optical depth from the microwave polarization difference index. *IEEE Geosci. Remote Sens. Lett.* 2, 121–123. <https://doi.org/10.1109/LGRS.2005.843983>
- Miller, C., Hilton, J., Sullivan, A., Prakash, M., 2015. SPARK – A bushfire spread prediction tool, in: *Environmental Software Systems. Infrastructures, Services and Applications*. Presented at the International Symposium on Environmental Software Systems, Springer, Cham, pp. 262–271. https://doi.org/10.1007/978-3-319-15994-2_26
- Miller, J.D., Danzer, S.R., Watts, J.M., Stone, S., Yool, S.R., 2003. Cluster analysis of structural stage classes to map wildland fuels in a Madrean ecosystem. *J. Environ. Manage.* 68, 239–252. [https://doi.org/10.1016/S0301-4797\(03\)00062-8](https://doi.org/10.1016/S0301-4797(03)00062-8)
- Mistry, J., Bilbao, B.A., Berardi, A., 2016. Community owned solutions for fire management in tropical ecosystems: case studies from Indigenous communities of South America. *Phil Trans R Soc B* 371, 20150174. <https://doi.org/10.1098/rstb.2015.0174>
- Mitchell, A.L., Rosenqvist, A., Mora, B., 2017. Current remote sensing approaches to monitoring forest degradation in support of countries measurement, reporting and verification (MRV) systems for REDD+. *Carbon Balance Manag.* 12, 9. <https://doi.org/10.1186/s13021-017-0078-9>
- Neale, T., Weir, J.K., McGee, T.K., 2016. Knowing wildfire risk: scientific interactions with risk mitigation policy and practice in Victoria, Australia. *Geoforum* 72, 16–25. <https://doi.org/10.1016/j.geoforum.2016.03.008>
- Newnham, G.J., Grant, I., Martin, D., Anderson, S.A.J., 2010. Improved methods for assessment and prediction of grassland curing (No. A.11.10), Satellite Based Curing Methods and Mapping (Project A1.4). Bushfire Cooperative Research Centre, Melbourne, VIC.
- Newnham, G.J., Verbesselt, J., Grant, I.F., Anderson, S.A.J., 2011. Relative Greenness Index for assessing curing of grassland fuel. *Remote Sens. Environ.* 115, 1456–1463. <https://doi.org/10.1016/j.rse.2011.02.005>
- Nijs, A.H.A. de, Parinussa, R.M., Jeu, R.A.M. de, Schellekens, J., Holmes, T.R.H., 2015. A methodology to determine radio-frequency interference in AMSR2 observations. *IEEE Trans. Geosci. Remote Sens.* 53, 5148–5159. <https://doi.org/10.1109/TGRS.2015.2417653>
- Noble, I.R., Gill, A.M., Bary, G. a. V., 1980. McArthur's fire-danger meters expressed as equations. *Aust. J. Ecol.* 5, 201–203. <https://doi.org/10.1111/j.1442-9993.1980.tb01243.x>
- Olson, J.S., 1963. Energy storage and the balance of producers and decomposers in ecological systems. *Ecology* 44, 322–331. <https://doi.org/10.2307/1932179>
- Osher, S., Sethian, J.A., 1988. Fronts propagating with curvature-dependent speed: algorithms based on Hamilton-Jacobi formulations. *J. Comput. Phys.* 79, 12–49. [https://doi.org/10.1016/0021-9991\(88\)90002-2](https://doi.org/10.1016/0021-9991(88)90002-2)
- Owe, M., De Jeu, R., Walker, J., 2001. A methodology for surface soil moisture and vegetation optical depth retrieval using the microwave polarization difference

- index. *IEEE Trans. Geosci. Remote Sens.* 39, 1643–1654. <https://doi.org/10.1109/36.942542>
- Padilla, M., Stehman, S.V., Ramo, R., Corti, D., Hantson, S., Oliva, P., Alonso-Canas, I., Bradley, A.V., Tansey, K., Mota, B., Pereira, J.M., Chuvieco, E., 2015. Comparing the accuracies of remote sensing global burned area products using stratified random sampling and estimation. *Remote Sens. Environ.* 160, 114–121. <https://doi.org/10.1016/j.rse.2015.01.005>
- Paget, M.J., King, E.A., 2008. MODIS Land data sets for the Australian region (Internal Report No. 4), CSIRO Marine and Atmospheric Research internal report. CSIRO Marine and Atmospheric Research Black Mountain, Canberra, Australia.
- Parinussa, R.M., Yilmaz, M.T., Anderson, M.C., Hain, C.R., de Jeu, R. a. M., 2014. An intercomparison of remotely sensed soil moisture products at various spatial scales over the Iberian Peninsula. *Hydrol. Process.* 28, 4865–4876. <https://doi.org/10.1002/hyp.9975>
- Paton-Walsh, C., Smith, T.E.L., Young, E.L., Griffith, D.W.T., Guérette, É.-A., 2014. New emission factors for Australian vegetation fires measured using open-path Fourier transform infrared spectroscopy – part 1: methods and Australian temperate forest fires. *Atmos Chem Phys* 14, 11313–11333. <https://doi.org/10.5194/acp-14-11313-2014>
- Penman, T.D., Collins, L., Price, O.F., Bradstock, R.A., Metcalf, S., Chong, D.M.O., 2013. Examining the relative effects of fire weather, suppression and fuel treatment on fire behaviour – a simulation study. *J. Environ. Manage.* 131, 325–333. <https://doi.org/10.1016/j.jenvman.2013.10.007>
- Peterson, S.H., Roberts, D.A., Dennison, P.E., 2008. Mapping live fuel moisture with MODIS data: a multiple regression approach. *Remote Sens. Environ.* 112, 4272–4284. <https://doi.org/10.1016/j.rse.2008.07.012>
- Pettinari, M.L., Chuvieco, E., 2017. Fire behavior simulation from global fuel and climatic information. *Forests* 8, 179. <https://doi.org/10.3390/f8060179>
- Price, O.F., Penman, T.D., Bradstock, R.A., Boer, M.M., Clarke, H., 2015. Biogeographical variation in the potential effectiveness of prescribed fire in south-eastern Australia. *J. Biogeogr.* 42, 2234–2245. <https://doi.org/10.1111/jbi.12579>
- Pugnet, L., Chong, D.M., Duff, T. J., Tolhurst, K.G., 2013. Wildland–urban interface (WUI) fire modelling using PHOENIX Rapidfire: a case study in Cavailon, France. Presented at the 20th International Congress on Modelling and Simulation, Adelaide.
- Purton, C.M., 1982. Equations for the McArthur mark 4 grassland fire danger meters. *Meteorol. Note* 147, 1–12.
- Ratnam, J.V., Doi, T., Behera, S.K., 2017. Dynamical downscaling of SINTEX-F2v CGCM seasonal retrospective Austral summer forecasts over Australia. *J. Clim.* 30, 3219–3235. <https://doi.org/10.1175/JCLI-D-16-0585.1>
- Reich, R., Lundquist, J., Bravo, V., 2004. Spatial models for estimating fuel loads in the Black Hills, South Dakota, USA. *Int. J. Wildland Fire* 13, 119–129.
- Reichle, R.H., Koster, R.D., Liu, P., Mahanama, S.P.P., Njoku, E.G., Owe, M., 2007. Comparison and assimilation of global soil moisture retrievals from the Advanced Microwave Scanning Radiometer for the Earth Observing System (AMSR-E) and the Scanning Multichannel Microwave Radiometer (SMMR). *J. Geophys. Res. Atmospheres* 112, D09108. <https://doi.org/10.1029/2006JD008033>
- Rodríguez-Fernández, N.J., Mialon, A., Mermoz, S., Bouvet, A., Richaume, P., Bitar, A.A., Al-Yaari, A., Brandt, M., Kaminski, T., Toan, T.L., Kerr, Y.H., Wigneron, J.-P., 2018. An evaluation of SMOS L-band vegetation optical depth (L-VOD) data sets: high sensitivity of L-VOD to above-ground biomass in Africa. *Biogeosciences* 15, 4627–4645. <https://doi.org/10.5194/bg-15-4627-2018>
- Rosenqvist, A., Shimada, M., Suzuki, S., Ohgushi, F., Tadono, T., Watanabe, M., Tsuzuku, K., Watanabe, T., Kamijo, S., Aoki, E., 2014. Operational performance

- of the ALOS global systematic acquisition strategy and observation plans for ALOS-2 PALSAR-2. *Remote Sens. Environ.* 155, 3–12. <https://doi.org/10.1016/j.rse.2014.04.011>
- Rothermel, R.C., 1972. A mathematical model for predicting fire spread in wildland fuels. USDA For. Serv. Res. Pap. INT-115.
- Rouse, J.W., Haas, R.H., Schell, J.A., Deering, D.W., 1973. Monitoring vegetation systems in the Great Plains with ERTS. Presented at the NASA. Goddard Space Flight Center 3d ERTS-1 Symp., Washington DC, United States, pp. 309–317.
- Ruiz, J.A.M., Lázaro, J.R.G., Cano, I. del Á., Leal, P.H., 2014. Burned area mapping in the North American boreal forest using Terra-MODIS LTDR (2001–2011): A comparison with the MCD45A1, MCD64A1 and BA GEOLAND-2 products. *Remote Sens.* 6, 815–840. <https://doi.org/10.3390/rs6010815>
- Saatchi, S., Halligan, K., Despain, D.G., Crabtree, R.L., 2007. Estimation of forest fuel load from radar remote sensing. *IEEE Trans. Geosci. Remote Sens.* 45, 1726–1740. <https://doi.org/10.1109/TGRS.2006.887002>
- Scott, K., Oswald, B., Farrish, K., Unger, D., 2002. Fuel loading prediction models developed from aerial photographs of the Sangre de Cristo and Jemez mountains of New Mexico, USA. *Int. J. Wildland Fire* 11, 85–90.
- Sharples, J.J., McRae, R.H.D., Weber, R.O., Gill, A.M., 2009a. A simple index for assessing fuel moisture content. *Environ. Model. Softw.* 24, 637–646. <https://doi.org/10.1016/j.envsoft.2008.10.012>
- Sharples, J.J., McRae, R.H.D., Weber, R.O., Gill, A.M., 2009b. A simple index for assessing fire danger rating. *Environ. Model. Softw.* 24, 764–774. <https://doi.org/10.1016/j.envsoft.2008.11.004>
- Stambaugh, M.C., Dey, D.C., Guyette, R.P., He, H.S., Marschall, J.M., 2011. Spatial patterning of fuels and fire hazard across a central U.S. deciduous forest region. *Landsc. Ecol.* 26, 923–935. <https://doi.org/10.1007/s10980-011-9618-y>
- Sullivan, A.L., Sharples, J.J., Matthews, S., Plucinski, M.P., 2014. A downslope fire spread correction factor based on landscape-scale fire behaviour. *Environ. Model. Softw.* 62, 153–163. <https://doi.org/10.1016/j.envsoft.2014.08.024>
- Surawski, N.C., Sullivan, A.L., Roxburgh, S.H., Polglase, P.J., 2016. Estimates of greenhouse gas and black carbon emissions from a major Australian wildfire with high spatiotemporal resolution. *J. Geophys. Res. Atmospheres* 121, 2016JD025087. <https://doi.org/10.1002/2016JD025087>
- Teubner, I.E., Forkel, M., Jung, M., Liu, Y.Y., Miralles, D.G., Parinussa, R., van der Schalie, R., Vreugdenhil, M., Schwalm, C.R., Tramontana, G., Camps-Valls, G., Dorigo, W.A., 2018. Assessing the relationship between microwave vegetation optical depth and gross primary production. *Int. J. Appl. Earth Obs. Geoinformation* 65, 79–91. <https://doi.org/10.1016/j.jag.2017.10.006>
- Tolhurst, K.G., Chong, D.M., Pitts, A., 2007. PHOENIX – a dynamic fire characterization simulation tool. Presented at the Bushfire CRC Fire Behaviour Workshop, Hobart, Tasmania.
- Tolhurst, K.G., Shields, B., Chong, D.M., 2008. Phoenix: development and application of a bushfire risk management tool. *Aust. J. Emerg. Manag.* 23.
- Turner, D., Lewis, M., Ostendorf, B., 2011. Spatial indicators of fire risk in the arid and semi-arid zone of Australia. *Ecol. Indic., Spatial information and indicators for sustainable management of natural resources* 11, 149–167. <https://doi.org/10.1016/j.ecolind.2009.09.001>
- Van Linn, P.F., Nussear, K.E., Esque, T.C., DeFalco, L.A., Inman, R.D., Abella, S.R., 2013. Estimating wildfire risk on a Mojave Desert landscape using remote sensing and field sampling. *Int. J. Wildland Fire* 22, 770–779.
- Vermote, E.F., Vermeulen, A., 1999. Atmospheric correction algorithm: spectral reflectance (MOD09) (No. 4.0), NASA contract NAS5-96062. University of Maryland, USA.

- Vettor, R., Guedes Soares, C., 2017. Characterisation of the expected weather conditions in the main European coastal traffic routes. *Ocean Eng.* 140, 244–257. <https://doi.org/10.1016/j.oceaneng.2017.05.027>
- Yebra, M., Dennison, P.E., Chuvieco, E., Riano, D., Zylstra, P., Hunt Jr., E.R., Danson, F.M., Qi, Y., Jurdao, S., 2013. A global review of remote sensing of live fuel moisture content for fire danger assessment: Moving towards operational products. *Remote Sens. Environ.* 136, 455–468.
- Zhang, X., Drake, N.A., Wainwright, J., Mulligan, M., 1999. Comparison of slope estimates from low resolution DEMs: scaling issues and a fractal method for their solution. *Earth Surf. Process. Landf.* 24, 763–779.
- Zhu, Q., Yang, X., Yu, Q., 2015. Climate change impact on bushfire risk in New South Wales, Australia, in: 2015 IEEE International Geoscience and Remote Sensing Symposium (IGARSS). Presented at the 2015 IEEE International Geoscience and Remote Sensing Symposium (IGARSS), pp. 1413–1416. <https://doi.org/10.1109/IGARSS.2015.7326042>
- Zweig, M.H., Campbell, G., 1993. Receiver-operating characteristic (ROC) plots: a fundamental evaluation tool in clinical medicine. *Clin. Chem.* 39, 561–577.